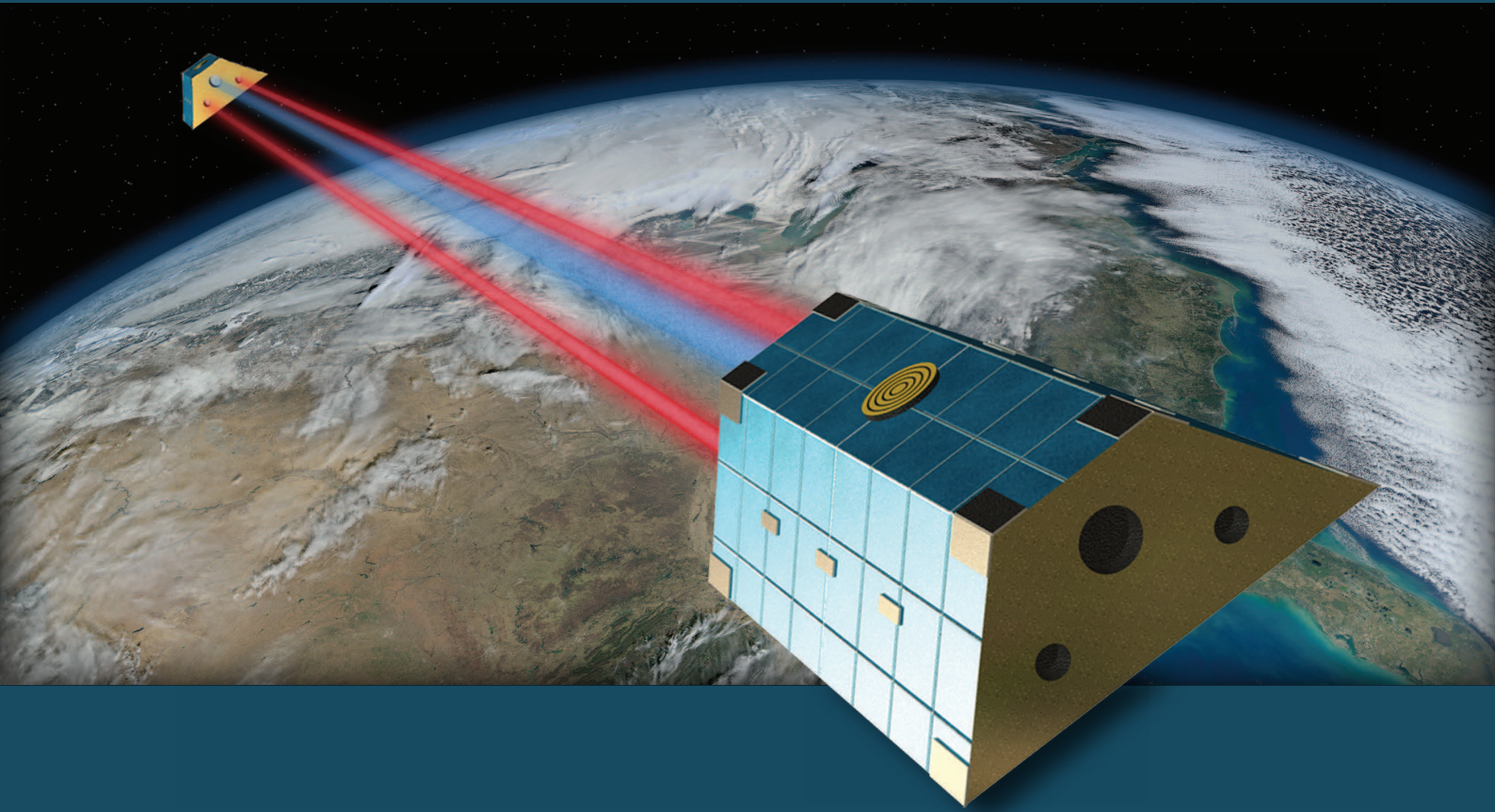


Intersatellite Laser Interferometry



Test Environments for GRACE Follow-On

*Cover picture: Artistic view of the GRACE Follow-On satellites.
Image credit: Satellites: AEI/Daniel Schütze, Earth: [1].*

Download this thesis from
www.gracefo.spacegravity.org/thesis.



Watch a brief video introduction at
www.gracefo.spacegravity.org/video1.



Intersatellite laser interferometry

Test environments for GRACE Follow-On

PhD thesis

of

Daniel Schütze

2015



Leibniz
Universität
Hannover



INSTITUTE FOR
GRAVITATIONAL PHYSICS
LEIBNIZ UNIVERSITY HANOVER



MAX PLANCK INSTITUTE FOR
GRAVITATIONAL PHYSICS
ALBERT EINSTEIN INSTITUTE



Intersatellite laser interferometry

Test environments for GRACE Follow-On

Von der QUEST-Leibniz-Forschungsschule
der Gottfried Wilhelm Leibniz Universität Hannover
zur Erlangung des Grades

DOKTOR DER NATURWISSENSCHAFTEN
– Dr. rer. nat. –

genehmigte Dissertation
von

Dipl.-Phys. Daniel Schütze,
geboren am 13.11.1981 in Neuss.

Referent	Prof. Dr. rer. nat. Karsten Danzmann, AEI Hannover
Korreferent	Prof. Dr. rer. nat. Claus Braxmeier, ZARM/DLR, Universität Bremen
Korreferent	Prof. Dr.-Ing. Jakob Flury, IfE, Universität Hannover
Tag der Promotion	16.12.2014

Abstract

Laser interferometry is the future of high-precision intersatellite range measurements. GRACE Follow-On, a two-satellite Earth geodesy mission which will be launched in 2017, sets a new milestone by hosting, for the first time, a Laser Ranging Interferometer (LRI) to measure distance changes between the satellites with unprecedented precision. While the main science instrument is still a conventional microwave ranging system, the LRI serves as a technology demonstrator to pave the way for future satellite missions using laser interferometry.

New space technologies require extensive test campaigns to verify and consolidate the design functionality. The test campaigns are performed in specialized test environments. This thesis presents the development of such test environments which have served to test and verify the design functionality of two key LRI components: the Triple Mirror Assembly (TMA) and the LRI Optical Bench.

The TMA is a passive retroreflector which sends the local oscillator laser beam to the distant spacecraft. The first key property of the TMA is the beam coalignment of the retroreflected laser beam with respect to the incident beam. This thesis verifies that the TMA design is capable of a beam coalignment of better than $10\ \mu\text{rad}$, while incoming and outgoing beams are laterally separated by 60 cm.

The second key property of the TMA is a small rotation-to-pathlength coupling, which couples local satellite attitude jitter into the pathlength measurement and is one of the LRI's limiting noise sources. The investigations in this thesis have shown that the TMA rotation-to-pathlength coupling is reduced to below $20\ \mu\text{m}/\text{rad}$ when rotating around the TMA's point of minimal coupling (PMC). Furthermore, the PMC has been located within $\pm 51\ \mu\text{m}$.

The LRI Optical Bench is the core piece of the LRI. Here, the local oscillator beam is actively coaligned to the wavefronts received from the distant spacecraft using the LRI beam steering method. This beam steering is crucial in order to maintain the intersatellite laser link, since drag of the residual atmosphere leads to a large local spacecraft attitude jitter.

In this thesis, the LRI beam steering method has been implemented on breadboard level. Investigations with the optical bench breadboard model have verified that the LRI beam steering method is capable of maintaining an intersatellite laser link with a coalignment of local oscillator wavefronts and received wavefronts of better than $\pm 10\ \mu\text{rad}$ under local spacecraft attitude jitter of many mrad. Furthermore, a beam coalignment stability of better than $10\ \mu\text{rad}/\sqrt{\text{Hz}}$ in the GRACE Follow-On measurement frequency band of 0.002...0.1 Hz has been achieved.

The test environments and test campaigns presented in this thesis have substantially supported the verification and consolidation of the LRI design, so that in June 2014, the LRI successfully passed the Critical Design Review at NASA/JPL and has

now entered the flight unit production phase. Furthermore, the test concepts developed in this thesis have opened a whole new avenue of investigation for future satellite missions using intersatellite laser interferometry.

Keywords: GRACE Follow-On, intersatellite interferometry,
space instrumentation

Kurzzusammenfassung

Die Zukunft der hochpräzisen Entfernungsmessung zwischen Satelliten heißt Laserinterferometrie. Ein Meilenstein in dieser Entwicklung ist die GRACE Follow-On Mission, die ab 2017 mit zwei Satelliten das Erdschwerefeld vermessen wird. GRACE Follow-On wird zum allerersten Mal in der Geschichte der Raumfahrt ein Laserinterferometer (LRI) zur Messung von Abstandsänderungen zwischen Satelliten mit bisher unerreichter Präzision einsetzen. Das Hauptinstrument von GRACE Follow-On verwendet weiterhin Mikrowellen zur Entfernungsmessung. Die Rolle des LRI ist die eines Technologiedemonstrators, um den Weg für zukünftige Satellitenmissionen mit Laserinterferometern zu ebnen.

Neue Technologien in der Raumfahrt erfordern umfassende Testkampagnen, um die Funktionalität des Designs zu verifizieren und zu konsolidieren. Die Testkampagnen werden in speziellen Testumgebungen durchgeführt. Diese Arbeit beschreibt die Entwicklung geeigneter Testumgebungen, in denen zwei LRI-Schlüsselkomponenten untersucht wurden: ein spezieller virtueller Retroreflektor, genannt “Triple Mirror Assembly” (TMA), und die LRI Optische Bank.

Der TMA ist ein passiver Retroreflektor, der den Laserstrahl des Lokaloszillators zum entfernten Satelliten schickt. Die erste Schlüsseleigenschaft des TMA ist Strahlparallelität. Sie bestimmt, wie parallel der retroreflektierte Strahl zur Achse des einlaufenden Strahls ist. In dieser Arbeit wird gezeigt, dass das TMA-Design eine Strahlparallelität von besser als $10 \mu\text{rad}$ erreicht, während der einlaufende und der retroreflektierte Strahl um 60 cm lateral versetzt sind.

Die zweite Schlüsseleigenschaft des TMA ist eine kleine Rotations-zu-Längenkopplung, die Fluktuationen in der Fluglage des lokalen Satelliten in die gemessene Weglänge koppelt. Dies ist eine der limitierenden Rauschquellen des LRI. Die Untersuchungen dieser Arbeit belegen, dass die Rotations-zu-Längenkopplung des TMA sich auf unter $20 \mu\text{m}/\text{rad}$ reduziert, wenn die Rotationen um den Punkt kleinster Kopplung (PMC) durchgeführt werden. Desweiteren wurde der PMC auf $\pm 51 \mu\text{m}$ genau lokalisiert.

Die LRI Optische Bank ist das Kernstück des LRI. Hier wird der Laserstrahl des Lokaloszillators aktiv auf die empfangenen Wellenfronten vom entfernten Satelliten ausgerichtet. Diese Strahlnachführung ist essentiell, um die Laser-Verbindung zwischen den Satelliten aufrechtzuerhalten, da die Fluglage der Satelliten durch den Einfluss der Restatmosphäre stark schwankt.

In dieser Arbeit wurde die LRI-spezifische aktive Strahlnachführung in einem Prototypen der LRI Optischen Bank umgesetzt. Untersuchungen mit diesem Prototypen haben gezeigt, dass eine Laser-Verbindung zwischen den Satelliten aufrechterhalten werden kann, auch wenn die Fluglage der Satelliten um viele mrad schwankt. Dabei wurde der Strahl des Lokaloszillators auf unter $\pm 10 \mu\text{rad}$ parallel zum empfangenen

Strahl gehalten, und zwar mit einer Stabilität von besser als $10 \mu\text{rad}/\sqrt{\text{Hz}}$ im GRACE Follow-On Frequenzband von 0.002...0.1 Hz.

Die Testumgebungen und Testkampagnen, die in dieser Arbeit vorgestellt werden, haben wesentlich zur Bestätigung des LRI-Designs beigetragen, so dass das LRI im Juni 2014 erfolgreich das Critical Design Review bei NASA/JPL bestanden hat und mit der Herstellung von LRI-Flughardware begonnen wurde. Des Weiteren eröffnen die Test-Konzepte, die in dieser Arbeit entwickelt wurden, neue Wege zu Untersuchungen für zukünftige Missionen, die Laserinterferometrie zur Abstandsmessung zwischen Satelliten verwenden.

Schlagworte: GRACE Follow-On, Intersatelliten-Interferometrie, Raumfahrttechnologie

Contents

Abstract	5
Kurzzusammenfassung	7
Contents	9
Acronyms	13
List of figures	17
1 Introduction	21
1.1 GRACE and GRACE Follow-On	23
1.2 The GRACE Follow-On Laser Ranging Interferometer	25
1.3 The Triple Mirror Assembly	29
1.3.1 Basic TMA properties	29
1.3.2 TMA rotation-to-pathlength coupling	29
1.3.3 TMA with non-zero mirror misalignments	30
1.4 The LRI Optical Bench	34
1.4.1 RX beam, LO beam, and telescope	34
1.4.2 Rotation-to-pathlength coupling	34
1.4.3 Heterodyne interferometry	35
1.4.4 Quadrant photo receiver signals	36
1.4.5 The LRI beam steering method	38
2 Items under test	41
2.1 Triple Mirror Assemblies	42
2.1.1 Fabrication of TMA units	42
2.1.2 TMA coordinate systems	43
2.2 Optical bench breadboard model	47
2.2.1 Optical bench assembly	48
2.2.2 LO beam generator	50
2.2.3 Quadrant photo receiver	55
2.2.4 Integration of OBBM subunits	57
3 Test environments for LRI components	61
3.1 TMA beam coalignment test bed	62
3.1.1 Setup of the TMA beam coalignment test bed	63
3.1.2 Recovery of TMA beam coalignment information	66

3.1.3	Data evaluation tool	70
3.2	TMA rotation-to-pathlength coupling test bed	73
3.2.1	PMC test bed: locating the TMA PMC	74
3.2.2	CMM test bed	81
3.2.3	Uncertainty of TMA vertex and PMC colocation measurement	91
3.3	LRI Optical Bench test bed	93
3.3.1	RX beam generation	93
3.3.2	Phasemeter, DWS signal computation, and beam steering control loop	97
3.3.3	Simulation of DWS signals and heterodyne efficiency	102
3.3.4	Coalignment of LO beam and RX beam	103
3.3.5	Measuring rotation-to-pathlength coupling	105
3.3.6	QPD phase offsets	106
4	Test results	107
4.1	TMA beam coalignment test bed	108
4.1.1	TMA beam coalignment test results	108
4.1.2	Discussion	108
4.1.3	Conclusion	110
4.2	TMA rotation-to-pathlength coupling test results	111
4.2.1	Pre-alignment in CMM	111
4.2.2	Locating the TMA PMC	112
4.2.3	Measuring TMA vertex and BMR position with CMM	117
4.2.4	Measuring TMA dihedral angles and beam coalignment with CMM	118
4.2.5	Discussion	119
4.2.6	Conclusion	123
4.3	OBBM test results	125
4.3.1	Calibration of QPD phase offsets	125
4.3.2	Beamwalk on QPDs	125
4.3.3	Transfer function of beam steering loop	127
4.3.4	DWS signals, DWS transfer matrix, and heterodyne efficiency	129
4.3.5	Coalignment of LO beam and RX beam	131
4.3.6	Rotation-to-pathlength coupling	133
4.3.7	Conclusion	134
5	Conclusion and outlook	135
5.1	Conclusion	135
5.2	Outlook	138
5.2.1	Testing of LRI flight hardware	138
5.2.2	The LRI ground reference setup	138
5.2.3	Future satellite geodesy missions with laser interferometers	139
	Appendix	143
	Bibliography	149
	Acknowledgments	161

CONTENTS

Curriculum vitae	163
Publications	165

Acronyms

AC	Alternating current
ADC	Analogue-to-digital converter
AEI	Albert Einstein Institute; often synonymously for Max Planck Institute for Gravitational Physics (Albert Einstein Institute) and Institute for Gravitational Physics – Leibniz Universität Hannover
ANU	Australian National University
AR	Anti-reflective
BS	Beam splitter
CABAM	CMM-assisted beam alignment and measurement
CAD	Computer-aided design
CAS	Cassidian Optronics GmbH (formerly Carl Zeiss AG)
CCD	Charge-coupled device
CFB	Carbon fiber breadboard
CFRP	Carbon fiber-reinforced plastic
CFRP TMA	TMA with CFRP tube spacer
CM	Center of mass
CNC	Computerized numerical control
CP	Compensation plate
CSIRO	Commonwealth Scientific and Industrial Research Organisation
DAC	Digital-to-analog converter
DC	Direct current
DLR	Deutsches Zentrum für Luft- und Raumfahrt
DM	Design model
DPS	Differential power sensing

DWS	Differential wavefront sensing
EBB	Elegant breadboard model
EM	Engineering model
EOS	Electro Optic Systems Pty. Ltd.
FM	Flight model
GFZ	Helmholtz-Zentrum Potsdam – Deutsches GeoForschungsZentrum (German Research Centre for Geosciences)
Glass TMA	TMA with glass ceramic bar spacer
GNSS	Global navigation satellite system
GPS	Global positioning system
GRACE	Gravity Recovery and Climate Experiment
ICS	Interferometer-bound coordinate system
IfE	Institut für Erdmessung – Leibniz Universität Hannover
JPL	Jet Propulsion Laboratory
JQI	Joint Quantum Institute
LO	Local oscillator
LRI	Laser Ranging Interferometer
LSD	Linear spectral density
NASA	National Aeronautics and Space Administration
NIST	National Institute of Standards and Technology
OBA	Optical bench assembly
OBBM	Optical bench breadboard model
OBE	Optical bench electronics
OGSE	Optical ground support equipment
PLL	Phase-locked loop
PMC	Point of minimal coupling
PP	Pivot point
QM	Qualification model
QPD	Quadrant photodiode

ACRONYMS

QR code	Quick response code
RB	Reference bar
RX	Received
S/C	Spacecraft
SHS	Shack-Hartmann sensor
SM	Steering mirror
STI	SpaceTech GmbH Immenstaad
TCS	TMA-bound coordinate system
TDI	Time-delay interferometry
TMA	Triple Mirror Assembly
TX	Transmitted
ZARM	Zentrum für angewandte Raumfahrttechnologie und Mikrogravitation – Universität Bremen

List of figures

1.1	Schematic of the LRI architecture	25
1.2	Artistic view of GRACE Follow-On	26
1.3	Inside view of GRACE satellite with schematic LRI boxes	27
1.4	Sensitivity of GRACE and GRACE Follow-On	27
1.5	Schematic of virtual cornercube and TMA	30
1.6	Schematic of TMA invariants under rotation	31
1.7	QPD naming convention and DWS for one tilt dimension	37
1.8	Block diagram of beam steering control loop	39
2.1	Picture of CFRP TMA	43
2.2	Picture of Glass TMA	44
2.3	Picture of TMA DM	45
2.4	Schematic of OBBM	47
2.5	Assembly steps of OBA	51
2.6	CAD model of fully assembled OBA	52
2.7	Photograph of OBA	53
2.8	Schematic of LO beam generator	53
2.9	Picture of LO beam generator	54
2.10	LO beam wavefront recorded with SHS	56
2.11	Image of LO beam intensity profile taken with CCD camera	57
2.12	CAD model of fully assembled OBBM	59
2.13	Photograph of fully assembled OBBM	60
3.1	TMA beam coalignment test bed	64
3.2	Setup to measure flatness of RB	65
3.3	Topography of RB	65
3.4	Setup to measure TMA beam coalignment (photograph)	67
3.5	Illustration of CFRP TMA mounting types	67
3.6	Sample interferogram for CFRP TMA	69
3.7	Topography of simulated RB	72
3.8	Simulated interferogram of TMA beam coalignment measurement	72
3.9	Setup to locate TMA PMC	75
3.10	Glass TMA in PMC test bed (CAD model)	76
3.11	Glass TMA in PMC test bed (photograph)	77
3.12	TMA DM in PMC test bed (CAD model)	77
3.13	TMA DM in PMC test bed (photograph)	78
3.14	Setup to determine noise floor in PMC test bed	82

3.15	Vertex measurement of Glass TMA with CMM	83
3.16	Vertex measurement of TMA DM with CMM	84
3.17	Referencing TMA nominal incident beam axis with CMM	85
3.18	CABAM measurement principle	88
3.19	Setup to test CABAM	89
3.20	Schematic of LRI Optical Bench test bed with OBBM installed	94
3.21	LRI Optical Bench test bed with OBBM installed (CAD model)	95
3.22	LRI Optical Bench test bed with OBBM installed (photograph)	96
3.23	Wavefront and intensity profile of RX beam	97
3.24	Wavefront and intensity profile of RX beam in OBBM aperture	98
3.25	Schematic of phasemeter architecture	98
3.26	Response function of OBBM steering mirror piezo	100
3.27	Simulated transfer function of beam steering control loop	101
3.28	Numerically simulated DWS signals	103
3.29	Numerically simulated heterodyne efficiency	104
4.1	Interferograms of CFRP TMA	109
4.2	Locating TMA PMC ^x and BMR ^x in hexapod coordinates	113
4.3	Locating TMA PMC ^y and BMR ^y in hexapod coordinates	114
4.4	Locating TMA PMC ^z and BMR ^z in hexapod coordinates	114
4.5	Rotation-to-length coupling of Glass TMA during hexapod rotations	116
4.6	Rotation-to-length coupling of TMA DM and TMA QM during hexapod rotations	116
4.7	Stability of phase differences between QPD segments (time series)	125
4.8	Stability of phase differences between QPD segments (LSD)	126
4.9	Beamwalk suppression on OBBM QPD	127
4.10	Transfer function of beam steering control loop	128
4.11	DWS signals for OBBM QPD as measured during hexapod pitch and yaw rotations	129
4.12	DWS signals for QPD2 as measured during hexapod pitch and yaw rotations	130
4.13	Heterodyne efficiency measured on OBBM QPD during hexapod pitch and yaw rotations	131
4.14	Time series of GRACE-like attitude jitter performed by the hexapod and of beam coalignment of the beam steering loop	132
4.15	Closed-loop beam coalignment stability under hexapod attitude jitter	133
5.1	LRI ground reference setup	139
A.1	Optical layout of LINT	144
A.2	LINT interferometer CAD model	145
A.3	LINT and hexapod hosting carbon fiber breadboard and TMA	145
A.4	LINT templates	146
A.5	Hexapod gallows to place optical component	147

Chapter 1

Introduction

Laser interferometry is a powerful tool for high-precision measurements of small length fluctuations over large distances. This makes it especially well suited as intersatellite ranging device. There are two science fields that would immensely profit from the advent of intersatellite laser interferometry: gravitational wave astronomy and satellite geodesy.

Gravitational wave astronomers, who are hunting tiny ripples in space-time, have been pushing technology development to realize the Laser Interferometer Space Antenna (LISA, [2–18]). By monitoring length fluctuations between test masses that are separated by millions of kilometers, LISA will open the window for gravitational wave detection at low frequencies in the mHz regime, complementing ground-based instruments which operate at higher frequencies of 10...1000 Hz [19, 20].

Geosciences have been revolutionized by modern satellite geodesy. A prominent example is the two-satellite mission GRACE [21], which monitors intersatellite distance changes with a microwave ranging device. GRACE has been very successful [22–37] so that a successor mission was strongly called for by the data users. GRACE Follow-On, which will be launched in 2017, promises to be even more trail-blazing than its predecessor: It will, for the first time in the history of cosmonautics, use a Laser Ranging Interferometer (LRI) to measure distance changes between satellites. While the main science instrument is still a microwave ranging system, the LRI serves as a technology demonstrator for future intersatellite interferometry applications. Additionally, it is expected to deliver improved ranging data compared to the microwave instrument.

New technologies come with new challenges. Especially for a technology demonstrator such as the LRI, which has never been built or tested before, an extensive design study and verification is indispensable. At various design stages, breadboard models, prototypes, and engineering models have to be investigated to verify design functionality, identify design caveats, and consolidate the final design for the ultimate

flight unit production. These investigations take place in specialized test environments that focus on specific component properties.

This thesis presents test environments and test procedures for two LRI key components: the Triple Mirror Assembly (TMA) and the LRI Optical Bench. Dedicated test campaigns investigate the key properties of these two components. For the TMA, the key properties are beam coalignment and a small rotation-to-pathlength coupling, and for the LRI Optical Bench, the LRI beam steering method. The goal of this thesis is to verify that the design of the TMA and the LRI Optical Bench ensures that these two components fulfill their requirements.

In the remainder of this chapter, we take a closer look at GRACE and the GRACE Follow-On mission (Sec. 1.1). Then we focus on the LRI (Sec. 1.2) and pick out the two key components which are further investigated in this thesis: the Triple Mirror Assembly (Sec. 1.3) and the LRI Optical Bench (Sec. 1.4). The following chapter, *Items under test*, introduces the specific LRI units that have entered the test environments. Chapter 3, *Test environments for LRI components*, is dedicated to the test setups and procedures that have been developed in this thesis. Chapter 4, *Test results*, presents the test results that have been obtained during test campaigns with the specific LRI units in the test environments. Finally, the last chapter, *Conclusion and outlook*, provides a summary of the presented test environments and test campaigns and discusses the future prospects of the test environments.

1.1 GRACE and GRACE Follow-On

Earth – the place we all live on, our home, our habitat, our supplier of all resources essential for life. Earth observation and exploration is not only a matter of quenching our thirst for knowledge. In an age where human impact dramatically shapes the condition of the planet as a whole, it is increasingly a matter of survival to understand the underlying mechanisms and processes as a prerequisite to take appropriate actions.

An important tool to observe global processes on our planet is satellite geodesy [21, 38, 39]. By covering the entire surface of Earth in a reasonable amount of time, satellite geodesy allows to observe processes that affect the planet as a whole and that could hardly be grasped with small-scale measurements.

A very prominent satellite geodesy mission is the Gravity Recovery and Climate Experiment (GRACE, [21]), which was launched in 2002 as a joint project of NASA and GFZ. GRACE has been extremely successful in monitoring the spatial and temporal variations of Earth’s geoid [24, 32]. It was the first mission to prove impressively the feasibility of low-orbit satellite-to-satellite tracking. GRACE’s particular strength is resolving changes in Earth’s gravitational potential caused by hydrological mass transport [26]. This allows to study processes that are vital to humankind. To name a few examples, GRACE has verified groundwater depletion in California [40] and northern India [28] and an accelerated decline of Greenland’s ice sheet mass [27, 30, 35, 36].

GRACE comprises two identical satellites in a common, freely decaying, low polar orbit. The satellite separation is maintained between 170–270 km by occasional orbit maintenance maneuvers. Relative spacecraft velocities are a few m/s. A microwave ranging system tracks intersatellite distance changes with micrometer precision, while the satellite orbit is monitored with GNSS (global navigation satellite system) with centimeter accuracy [41]. From the measured distance changes, the gravity potential of Earth can be recovered.

Due to its relatively low orbit altitude of 450 km, GRACE is exposed to a non-negligible drag from residual atmosphere. Other non-gravitational forces acting on the satellites are solar radiation pressure and Earth’s albedo. These disturbances are measured with an accelerometer [42] and henceforth removed from the science measurement.

Every month, the surface of Earth is sufficiently covered by the ground track of the satellites to yield an update of the gravity field. This is a remarkable advantage of the GRACE mission, since it makes it possible to study temporal changes in Earth’s gravity field and, due to GRACE’s long mission lifetime of already more than 12 years, longterm trends.

The GRACE mission has a natural lifetime limit due to hardware fatigue and limited thruster fuel. The initially planned mission lifetime of five years has already greatly been exceeded. Especially the worn-out batteries will soon result in a mission termination.

Owing to its great success and the urgent need to continue the Earth gravity observations, NASA and GFZ are preparing a GRACE Follow-On mission which will be launched in 2017. The main science instrument on board of GRACE Follow-On is still a microwave ranging system. However, in addition, GRACE Follow-On will fly, for the first time ever, a Laser Ranging Interferometer (LRI, [43]) as technology demonstrator.

The goal of the LRI is to improve the intersatellite distance measurements by more than one order of magnitude in the measurement frequency band of 0.002...0.1 Hz, which is determined by the satellite orbit frequency. Furthermore, the LRI will demonstrate the feasibility of laser interferometry for future geodesy missions based on high-precision intersatellite ranging.

The GRACE geoid accuracy is not only limited by the intersatellite ranging precision, but by various noise sources such as accelerometer noise [42], temporal aliasing effects due to ocean tides [44], orbit determination [41], and spurious forces [45]. For this reason, we do not necessarily expect an immediate proportional improvement of the GRACE Follow-On geoid recovery by using the LRI. However, for future geodesy missions with an LRI as main science instrument [46, 47], the full benefit of the increased LRI ranging precision and pointing accuracy can be exploited.

The LRI is a joint project with US and German contributions. The developments under US responsibility are carried out by NASA and JPL, with major components delivered by Ball Aerospace and Tesat-Spacecom GmbH & Co. KG. The US part includes the phasemeter and payload processing electronics, laser frequency stabilization, and the laser source [48, 49].

The German side (GFZ/AEI/DLR/STI/Airbus) is responsible for the optics, the Triple Mirror Assembly, the beam steering method including electronics, and the quadrant photo receivers with electronics. Within the GRACE Follow-On project, the AEI has been nominated the principal investigator of the German LRI contributions. Additional support to the LRI project has come from Australia (ANU/EOS/CSIRO), where first Triple Mirror Assembly prototypes were built [50] and laser link acquisition between the two spacecraft was studied [51, 52].

During the past three years, the LRI project has progressed from early design studies to breadboard model proof-of-principle experiments and to engineering model fabrication and testing. In June 2014, the LRI has successfully passed the Critical Design Review at NASA/JPL and has now entered the flight unit production phase.

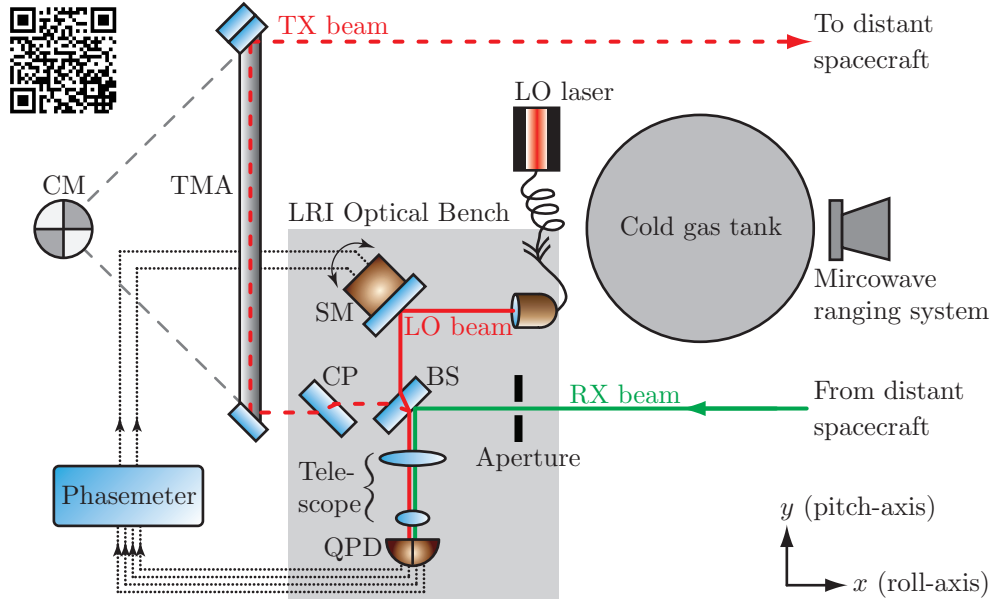


Figure 1.1: Schematic of the LRI on one of the two GRACE Follow-On satellites. The LRI is identical on both satellites. For an animation of the LRI inside the satellite, scan the QR code in the upper left corner of the picture or go to www.gracefo.spacegravity.org/video2.

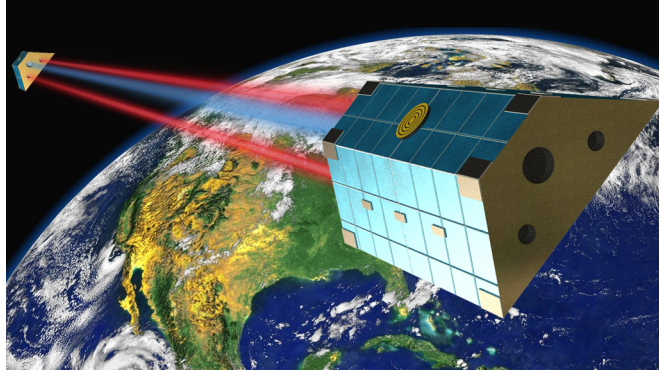
1.2 The GRACE Follow-On Laser Ranging Interferometer

Figure 1.1 shows a schematic of the LRI [43] on one satellite. The LRI is identical on both spacecraft. The LRI uses a symmetric active transponder principle: The weak incoming received (RX) beam is “amplified” by a strong local oscillator (LO) beam. This beam is then sent back to the distant spacecraft as transmitted (TX) beam via retroreflection by the Triple Mirror Assembly (TMA, [50, 53, 54]). An artistic view of the two GRACE Follow-On spacecraft is displayed in Fig. 1.2.

The local spacecraft attitude jitter is not sufficiently counteracted by the satellite’s attitude control system to support the intersatellite laser link. This makes it necessary to introduce the LRI beam steering method, which simultaneously coaligns the LO and the TX beams with the RX beam. This maximizes the interferometric contrast and makes sure that the TX beam, after being retroreflected by the TMA, points directly towards the distant spacecraft.

Since the LRI is a technology demonstrator and not the main science instrument, it had to be implemented within the limited space of the existing satellite design. The

Figure 1.2: Artistic view of the GRACE Follow-On satellites. The microwave ray is depicted in blue, the laser beams in red. Image credit: Satellites: AEI/Daniel Schütze, Earth: [1].



tight constraints on the available space become clear from the photograph of the inside of one of the GRACE satellites shown in Fig. 1.3. The foreseen locations for the different LRI units are marked with pink boxes.

As one can see in Figs. 1.1 and 1.3, the line-of-sight between the two spacecraft’s (S/C) centers-of-masses (CM) is occupied by the main science instrument, the microwave ranging system, and tanks of the cold gas propulsion system. This was the original motivation to choose an off-axis interferometer configuration in which the interferometer beams are routed using the TMA. By placing the TMA vertex at the S/C CM, the LRI virtually measures distance changes between the two S/C centers-of-masses due to the special TMA properties [43]. Additionally, in the ideal case, the TMA properties assure that no rotation-to-pathlength couplings occur [43, 54].

While this “racetrack” configuration had originally been chosen to solve the problem of spatial constraints, it turned out that it allows for a simple implementation of closed-loop beam steering. In on-axis interferometer concepts, closed-loop beam steering cannot be implemented in such a simple manner. Thus the “racetrack” configuration is a promising candidate architecture even for a new mission design in which the line-of-sight would be available.

The LRI design sensitivity aims at $80 \text{ nm}/\sqrt{\text{Hz}}$ for the one-way range displacement measurement, as shown in Fig. 1.4. This is almost two orders of magnitude below the ranging residuals of the GRACE satellites. For low frequencies $\lesssim 5 \text{ mHz}$, the overall sensitivity is limited by noise of the accelerometer, allowing for an increased LRI noise level without impact on the final data product. Above 5 mHz , the main noise sources are laser frequency noise and TMA rotation-to-pathlength coupling driven by local spacecraft attitude jitter.

The laser frequency noise couples linearly with the spacecraft separation into the LRI measurement [43]. Since this is a single-link measurement, frequency noise cannot be canceled as in other interferometry schemes using time-delay interferometry

1.2 THE GRACE FOLLOW-ON LASER RANGING INTERFEROMETER

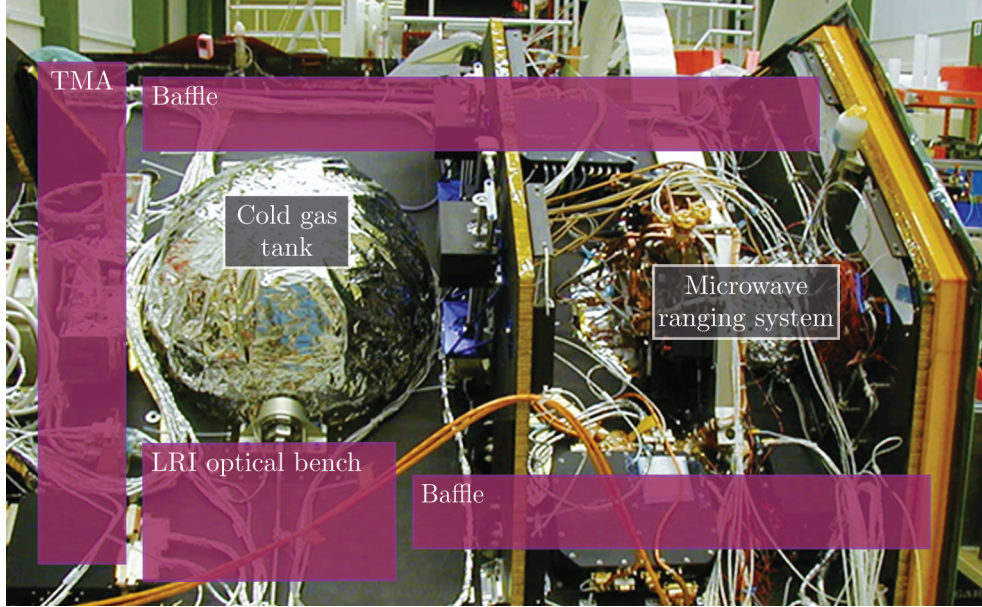
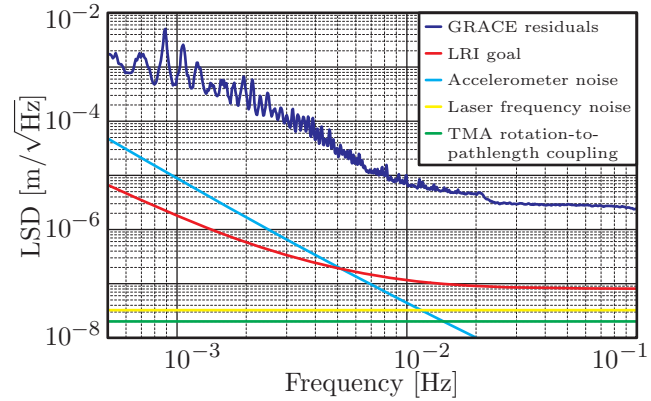


Figure 1.3: Inside view of GRACE satellite (image credit: [55]) with the foreseen positions for the LRI components schematically marked with pink boxes. The RX beam and the TX beam are contained within baffles.

Figure 1.4: Linear spectral density (LSD, [56]) of GRACE residuals and the LRI ranging sensitivity goal. For low frequencies, the overall sensitivity will be limited by accelerometer noise. Above 5 mHz, laser frequency noise and TMA rotation-to-pathlength coupling are the dominant noise sources. Source for GRACE residuals: Personal communication with Gerhard Heinzel (AEI); GRACE data available at [55, 57]. Source for LRI requirements: [43].



(TDI, [58]). However, laser frequency stabilization for the LRI laser has already been demonstrated [48, 49] and is expected to achieve $30 \text{ Hz}/\sqrt{\text{Hz}}$. For the largest spacecraft separation of 270 km and a laser frequency of 281 THz, which corresponds to a wavelength of 1064 nm, this leads to a noise contribution of $30 \text{ nm}/\sqrt{\text{Hz}}$.

The TMA rotation-to-pathlength coupling is caused by displacements of the TMA vertex with respect to the spacecraft's center of rotation which couple local spacecraft attitude jitter into the pathlength measurement. This is discussed in Sec. 1.3.2.

In the LRI concept in Fig. 1.1, we can identify four functional units: the phasemeter, the laser system including the frequency stabilization which is not shown in the figure, the TMA, and the LRI Optical Bench. This thesis focuses on the TMA and the LRI Optical Bench, which are introduced in more detail in the following sections.

1.3 The Triple Mirror Assembly

1.3.1 Basic TMA properties

The TMA functions as a passive retroreflector [59–63]: Its mirror planes intersect at right angles and constitute a virtual cornercube [64], as illustrated in Fig. 1.5. We call it virtual, because not the full corner is physically present, as in Fig. 1.5, (1). Instead, only those fractions of the cornercube physically exist where the beam is actually being reflected, see Fig. 1.5, (2).

The TMA mirrors M1, M2, M3 are installed into a 600 mm long rigid structure at the specific locations of the virtual cornercube where the laser beam is incident, as shown in Fig. 1.5, (2). Thus the virtual intersection point of the three mirror planes, the “TMA vertex”, is located outside the TMA structure. This makes it possible to position the TMA vertex at the spacecraft’s center of mass (CM) which is the center of spacecraft rotations, see Fig. 1.6 with $\Delta x = \Delta y = \Delta z \equiv 0$. In this way, rotation-to-pathlength coupling does not occur, due to the special properties of the TMA under rotations [43]:

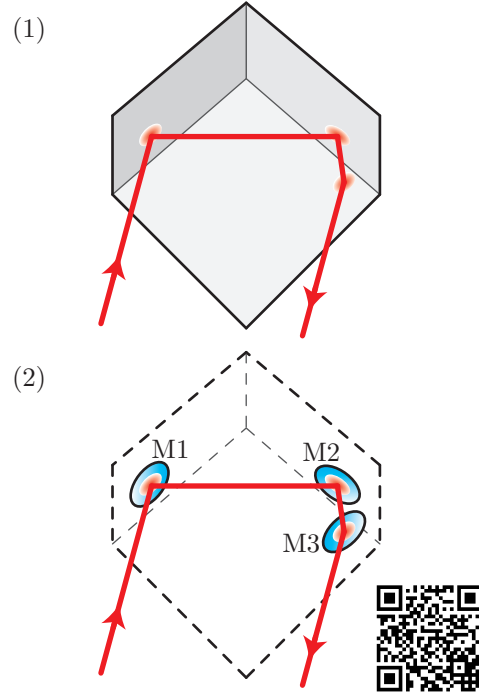
- The round-trip pathlength $L_{rt} = 2d$ is preserved. This is twice the distance from the starting point of the beam on plane (A) to plane (B) which is normal to the beam direction and intersects the retroreflector vertex.
- The propagation direction \vec{b}_{out} of the retroreflected beam does not change. It is anti-parallel to the incident beam \vec{b}_{in} , which assures that the TX beam is sent back to the distant spacecraft.
- The lateral beam offset h , which is equal for both incident and reflected beam, remains constant.

1.3.2 TMA rotation-to-pathlength coupling

An alignment offset of the TMA vertex Δy , Δz with respect to the spacecraft center-of-mass (CM, cf. Fig. 1.6) leads to coupling of local S/C pitch and yaw rotations, $\delta\theta_{pitch}$ and $\delta\theta_{yaw}$, into the interferometric one-way pathlength measurement $L = 0.5 \cdot L_{rt}$. For small S/C rotations, the linearized variation of L under rotations is given by [43]:

$$\delta L \approx (\Delta x \cdot \theta_{pitch} - \Delta z) \cdot \delta\theta_{pitch} + (\Delta x \cdot \theta_{yaw} + \Delta y) \cdot \delta\theta_{yaw}. \quad (1.1)$$

Figure 1.5: This schematic visualizes the equivalence between a cornercube retroreflector and the TMA. (1) Imagine a hollow cornercube which functions as a retroreflector. (2) The TMA mirrors $M1$, $M2$, $M3$ are placed at the locations where the laser beam is incident. They form a virtual cornercube retroreflector without the whole cornercube physically existing. This is also illustrated in a short animation, which you can watch by scanning the QR code in the lower right corner of the picture or by going to www.gracefo.spacegravity.org/video3.



Note that in this equation, roll rotations do not couple at all. The static on-axis angular offsets θ_{pitch} , θ_{yaw} are of the order of mrad, so that the contribution from the TMA vertex offset Δx is suppressed by three orders of magnitude and can be neglected.

The shape and magnitude of the pathlength noise contribution from TMA rotation-to-pathlength coupling depends on the residual spacecraft pointing noise due to the attitude control system. Assuming spacecraft pointing noise for $\delta\theta_{\text{roll}}$, $\delta\theta_{\text{pitch}}$, and $\delta\theta_{\text{yaw}}$ of $100 \mu\text{rad}/\sqrt{\text{Hz}}$ and TMA vertex placement offsets of $100 \mu\text{m}$, the noise contribution from TMA rotation-to-pathlength coupling is roughly $20 \text{ nm}/\sqrt{\text{Hz}}$. This makes the TMA rotation-to-pathlength coupling the second largest noise source in the LRI after laser frequency noise, cf. Fig. 1.4.

1.3.3 TMA with non-zero mirror misalignments

For a real TMA, we expect non-zero misalignments between the mirror planes. This manifests as two effects. Firstly, the incoming and outgoing beams are not exactly anti-parallel anymore, but there is a coalignment error introduced by the TMA. Secondly, the rotation-to-pathlength coupling behavior changes from the simple formula given in Eq. (1.1).

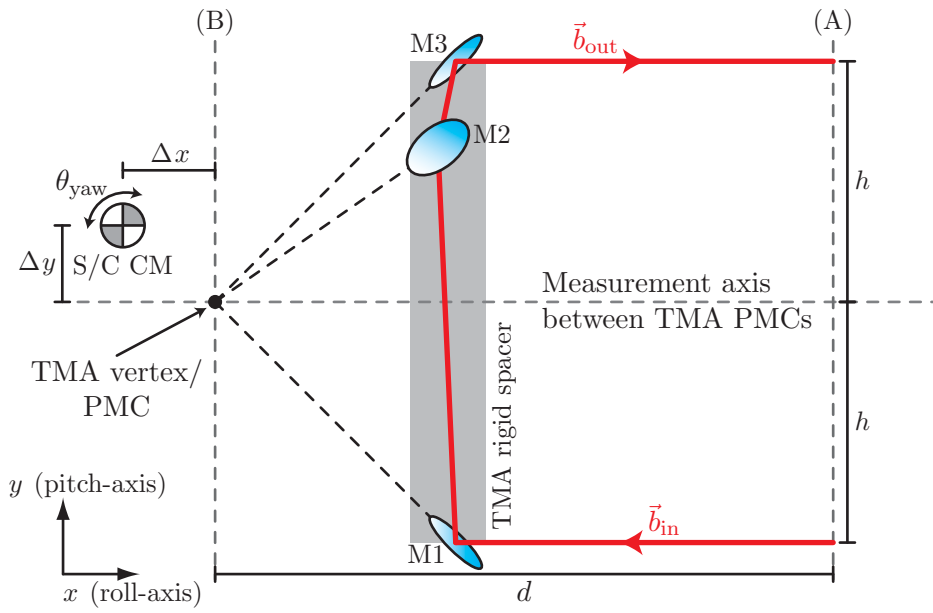


Figure 1.6: This sketch illustrates TMA properties under S/C rotations. The outgoing beam \vec{b}_{out} is always antiparallel to the incoming beam \vec{b}_{in} and the lateral beam offset h remains constant. Furthermore, for $\Delta x = \Delta y = \Delta z \equiv 0$, the roundtrip pathlength L_{rt} measured from a fixed reference plane (A) is constant as well. It is equal to twice the separation of the TMA vertex to that plane, $L_{rt} = 2d$.

We follow the analytical TMA model developed in [65, 66]. We introduce the deviations of the dihedral angles between the TMA mirrors M1, M2, M3 from 90° :

$$\vec{\gamma} := \begin{pmatrix} \gamma_1 \\ \gamma_2 \\ \gamma_3 \end{pmatrix} = \begin{pmatrix} \angle(\text{M1}, \text{M3}) - \pi/2 \\ \angle(\text{M1}, \text{M2}) - \pi/2 \\ \angle(\text{M2}, \text{M3}) - \pi/2 \end{pmatrix}. \quad (1.2)$$

Now we take a look at how TMA beam coalignment and TMA rotation-to-pathlength coupling change for $\vec{\gamma} \neq 0$.

1.3.3.1 TMA beam coalignment error

In a linear approximation, the outgoing beam direction \vec{b}_{out} for an incoming beam $\vec{b}_{\text{in}} = (-1, 0, 0)^\text{T}$, cf. Fig. 1.6, can be written as [65, 66]:

$$\begin{aligned} \vec{b}_{\text{out}} = & \begin{pmatrix} 1 \\ 0 \\ 0 \end{pmatrix} + \begin{pmatrix} 0 & 0 & 0 \\ -\sqrt{2} & -\sqrt{2} & 0 \\ 1 & -1 & \sqrt{2} \end{pmatrix} \vec{\gamma} \\ & + \begin{pmatrix} 0 & 0 & 0 \\ -\theta_{\text{roll}} + \theta_{\text{pitch}} & \theta_{\text{roll}} - \theta_{\text{pitch}} & -\sqrt{2} \cdot \theta_{\text{roll}} - \sqrt{2} \cdot \theta_{\text{pitch}} \\ -\sqrt{2}\theta_{\text{roll}} + \theta_{\text{yaw}} & -\sqrt{2} \cdot \theta_{\text{roll}} - \theta_{\text{yaw}} & -\sqrt{2} \cdot \theta_{\text{yaw}} \end{pmatrix} \vec{\gamma}. \end{aligned} \quad (1.3)$$

For an ideal TMA with $\vec{\gamma} = \vec{0}$, the outgoing beam direction is $(1, 0, 0)^\text{T}$. From the second term in Eq. (1.3), we see that non-zero mirror misalignments change the outgoing beam direction by the same order of magnitude. The third term shows that for a non-perfect TMA, the direction of the outgoing beam also depends on the TMA orientation. But since this term is suppressed by the on-axis angular offsets of $\theta_{\text{roll}}, \theta_{\text{pitch}}, \theta_{\text{yaw}} \lesssim 2 \text{ mrad}$, this effect is of second order and negligible.

For small angles, we can use Eq. (1.3) to define ‘‘horizontal’’ and ‘‘vertical’’ TMA beam coalignment error δ_{hor} and δ_{ver} , respectively:

$$\begin{aligned} \delta_{\text{hor}} &:= b_{\text{out}}^y = -\sqrt{2} \cdot \gamma_2 - \sqrt{2} \cdot \gamma_3, \\ \delta_{\text{ver}} &:= -b_{\text{out}}^z = -\gamma_1 + \gamma_2 - \sqrt{2} \cdot \gamma_3. \end{aligned} \quad (1.4)$$

While $\delta_{\text{hor}}, \delta_{\text{ver}}$ depend on the specific choice of coordinates, the root-mean-square coalignment error of the TMA is coordinate independent:

$$\delta_{\text{RMS}} = \sqrt{\delta_{\text{hor}}^2 + \delta_{\text{ver}}^2}. \quad (1.5)$$

From manufacturing and alignment tolerances, we expect mirror misalignments of the order of $10\ \mu\text{rad}$, which should result in a TMA beam coalignment error of the same order of magnitude. The initial beam coalignment of the TMA is required to be better than $10\ \mu\text{rad}$. After environmental tests such as thermal cycling and vibration the beam coalignment must still be smaller than $40\ \mu\text{rad}$.

1.3.3.2 Modified TMA rotation-to-pathlength coupling

The second effect of non-zero TMA mirror misalignments is a change of the rotation-to-pathlength coupling, which, in general, will not be zero anymore as in Eq. (1.1) for rotations around the TMA vertex. There exists a special point now, which we call *point of minimal coupling* (PMC), for which TMA rotation-to-pathlength coupling is minimized. For an ideal TMA, vertex and PMC coincide. For a realistic TMA with non-zero mirror misalignments, the TMA PMC is displaced from the vertex. For the specific dimensions of the TMA that is being used for the LRI, the offset between PMC and vertex is given by [65,66]

$$\begin{pmatrix} \delta x_{\text{PMC}} \\ \delta y_{\text{PMC}} \\ \delta z_{\text{PMC}} \end{pmatrix} \approx \begin{pmatrix} 0 \\ 12 \cdot (-\gamma_1 + \gamma_2) + 17 \cdot \gamma_3 \\ 150 \cdot (-\gamma_1 + \gamma_2) + 212 \cdot \gamma_3 \end{pmatrix} \cdot 1\ \text{mm/rad}. \quad (1.6)$$

With the expected TMA mirror misalignments of roughly $10\ \mu\text{rad}$ each, we derive an offset between TMA PMC and vertex of less than $10\ \mu\text{m}$. When rotating around the PMC, the remaining ranging error δL for non-zero TMA mirror misalignments, in linear approximation, is given by [65,66]:

$$\delta L = (266 \cdot \gamma_1 - 334 \cdot \gamma_2 + 424 \cdot \gamma_3) \cdot 1\ \text{mm/rad}^2 \cdot \delta\theta_{\text{roll}}. \quad (1.7)$$

While in principle, pitch and yaw coupling can still be zeroed by rotating around the PMC, now roll rotations inevitably couple. However, considering TMA mirror misalignments of $10\ \mu\text{rad}$, we expect the residual rotation-to-length coupling to be below $20\ \mu\text{m/rad}$.

1.4 The LRI Optical Bench

1.4.1 RX beam, LO beam, and telescope

The LRI Optical Bench is the core piece of the LRI optics, cf. Fig. 1.1. Here, RX beam and LO beam are interfered on a beam splitter (BS) and the LO beam/TX beam is coaligned with the RX beam by the LRI beam steering method. This ensures, via retroreflection by the TMA, that the TX beam reaches the distant spacecraft.

The RX beam has traveled a distance of roughly 200 km from the distant spacecraft and has expanded to a diameter of 60 m. Over the 8 mm diameter aperture of the LRI Optical Bench, the RX beam is flat in intensity and phase. After being clipped by the aperture, the RX beam therefore comes very close to what is referred to as “flattop” or “top hat” beam [67]. The received light power of the RX beam is of the order of 100 pW.

The RX beam and the LO beam are interfered on the BS (nominally 90% reflective, 10% transmissive). On the master spacecraft, the LO laser, which produces both the LO beam and the TX beam, is frequency-stabilized to a reference cavity [48]. On the slave spacecraft, the LO beam is phase-locked to the RX beam with a frequency offset so as to generate an amplified phase copy. The LO light power is of the order of some mW.

The LO beam is delivered to the optical bench with an optical fiber connected to a fiber collimator. On the optical bench, the LO beam is guided over a steering mirror, which can be actuated in two axes. A two-lens telescope images both steering mirror surface and aperture plane on a quadrant photodiode (QPD). The telescope serves three purposes: suppression of diffraction effects caused by beam clipping at the aperture, cancellation of beamwalk of the RX beam due to local spacecraft rotations and of the LO beam due to steering mirror tilts, and reduction of the beam sizes to match the QPD diameter.

1.4.2 Rotation-to-pathlength coupling

Since the beam splitter on the LRI Optical Bench (Fig. 1.1) is in the sensitive path of the roundtrip measurement, the question of optical bench rotation-to-length coupling arises. The optical pathlength through the beam splitter depends on the angle of the incident beam, so that the beam splitter exhibits a large linear rotation-to-length coupling of 2.2 mm/rad for local spacecraft yaw rotations [43]. This linear term can be suppressed by the use of a compensation plate (CP, [43]). The remaining coupling for pitch and yaw is quadratic and, for expected spacecraft rotations of less than 2 mrad,

of the order of $\mu\text{m}/\text{rad}$.

Recent investigations have shown that for a plane parallel beam splitter, ghost beams due to residual reflections at the beam splitter’s AR (anti-reflective) coating contribute to an additional, sinusoidal term in the rotation-to-pathlength coupling. While the amplitude of this coupling term is expected to be of the order of $\mu\text{m}/\text{rad}$, it could still be harmful to the intersatellite range measurement due to the sinusoidal modulation with several cycles per mrad.

For this reason, wedged optics have been chosen for beam splitter and compensation plate, so that ghost beams are reflected off the optical axis so they do not interfere with the measurement beams anymore. The wedges of beam splitter and compensation plate are matched and aligned to each other such that the influence on the beam coalignment of the TX beam with respect to the RX beam is negligible.

1.4.3 Heterodyne interferometry

The relative intersatellite velocities v_{rel} for GRACE Follow-On will be some m/s. With a laser wavelength of $\lambda = 1064\text{ nm}$, this leads to non-relativistic one-way Doppler frequency shifts of some MHz, according to [43]

$$\omega_{\text{D}} \approx \frac{-2\pi v_{\text{rel}}}{\lambda}. \quad (1.8)$$

Thus an interferometry scheme which is capable of phase-tracking over many fringes is required. For this reason, the LRI uses heterodyne interferometry to track the intersatellite distance changes, as is also foreseen for other intersatellite ranging applications [4].

In heterodyne interferometry, two laser beams with frequencies ω_0 and $\omega_0 + \Delta\omega$ are interfered. The frequency offset $\Delta\omega$ is achieved by offset phase-locking the laser light generated on the “slave” spacecraft to the RX wavefronts received from the “master” spacecraft. To obtain an unambiguous ranging signal for a full orbit, the offset frequency $\Delta\omega$ of the phase-lock must be larger than the maximum Doppler frequency shifts ω_{D} caused by the relative spacecraft motion, cf. Eq. (1.8).

On the LRI Optical Bench (Fig. 1.1), LO beam and RX beam are overlapped on the beam splitter and demagnified with a telescope to fit onto the QPD. The resulting optical power of the interfering light fields can be written as [67, 68]

$$P(t) = P_{\text{LO}} + P_{\text{RX}} + A \cdot \cos(\Delta\omega t - \varphi). \quad (1.9)$$

Here, P_{LO} and P_{RX} are the light powers of LO beam and RX beam, respectively. The amplitude of the AC light field is given by $A = 2\sqrt{\beta P_{\text{LO}} P_{\text{RX}}}$. The heterodyne

efficiency β is obtained from the overlap integral of LO wavefronts and RX wavefronts normalized to the incident light power and describes how well both light fields interfere. It depends on the beam properties of the LO beam and the RX beam and on relative beam tilts.

The heterodyne efficiency β is related to the interferometric contrast κ [67–71]:

$$\begin{aligned}\beta &= \frac{\kappa^2 (P_{\text{LO}} + P_{\text{RX}})^2}{4 P_{\text{LO}} P_{\text{RX}}}, \\ \kappa &= \frac{P_{\text{max}} - P_{\text{min}}}{P_{\text{max}} + P_{\text{min}}},\end{aligned}\tag{1.10}$$

with the minimum and maximum light power levels P_{min} and P_{max} , respectively.

Since β has a strong dependence on relative beam tilt [67], signal amplitudes are expected to drop below the noise level for relative beam tilts of more than about $\pm 200 \mu\text{rad}$. However, after launch, there will be a large unknown bias of some mrad between the LRI's optical axes and the estimated line-of-sight between the two spacecraft. The line-of-sight estimate is obtained with a star-tracker and an onboard orbit predictor. The bias is mainly due to a bias between the LRI's optical axes and the star-trackers' reference systems.

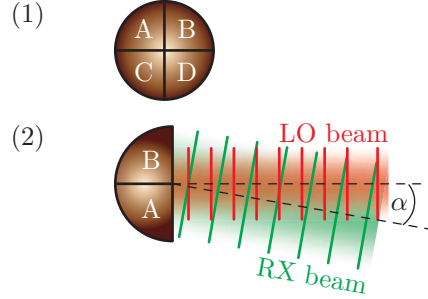
Additionally, the laser frequencies on the two spacecraft are expected to have an offset which might be larger than the bandwidth of the QPDs. This makes it necessary to perform an initial calibration scan in 5 degrees of freedom [51, 52, 67, 72]: While the steering mirrors on both spacecraft perform angular scan patterns, the laser frequency onboard the slave spacecraft is slowly ramped to find the correct combination of steering mirror angles and laser frequency which maximizes the heterodyne signal amplitude.

1.4.4 Quadrant photo receiver signals

A QPD consists of four segments A, B, C, D, separated by a small slit. The QPD naming convention used in the LRI project is shown in Fig. 1.7, (1). Light power P_i incident on a segment $i = \text{A, B, C, D}$ produces a photo current $J_i = \eta P_i$. The proportionality factor η is the responsivity of the photodiode. It depends on the semiconductor material and the wavelength of the laser light. For InGaAs it has a value of 0.7 A/W for a wavelength of 1064 nm.

The photo currents J_i are converted into voltages V_i by the quadrant photo receiver (QPR) electronics using transimpedance amplifiers. For interfering LO beam and RX beam, we find from Eq. (1.9) that the signal has a DC part and an AC part, which are separated by low-pass and high-pass filtering in the QPR electronics into V_i^{dc} and

Figure 1.7: (1) The QPD front view shows the segment naming convention used in the LRI project. (2) Split photodiode with two segments A and B to illustrate DWS for one tilt dimension. In this simplified case, the phase difference between segments A and B is proportional to the geometric tilt angle α between the wavefronts of the LO beam and the RX beam.



V_i^{ac} respectively.

The DC part is proportional to the DC light power on each QPD segment and can be used to determine the beam position on the QPD with differential power sensing (DPS, [73]). Neglecting offsets, horizontal and vertical beam displacements from the QPD center Δ_{hor} and Δ_{ver} can be inferred from

$$\begin{aligned}\Delta_{\text{hor}} &= C_{\text{hor}} \cdot \frac{V_A^{\text{dc}} + V_C^{\text{dc}} - V_B^{\text{dc}} - V_D^{\text{dc}}}{\sum_i V_i^{\text{dc}}}, \\ \Delta_{\text{ver}} &= C_{\text{ver}} \cdot \frac{V_A^{\text{dc}} + V_B^{\text{dc}} - V_C^{\text{dc}} - V_D^{\text{dc}}}{\sum_i V_i^{\text{dc}}},\end{aligned}\tag{1.11}$$

where $C_{\text{hor,ver}}$ are proportionality factors which depend on QPD, QPR, and beam properties. We can calibrate $C_{\text{hor,ver}}$ by translating the QPD transversally to the incident beam by a known distance.

The telescope of the LRI Optical Bench, cf. Sec.1.4.1, is designed to cancel beamwalk such that ideally $\Delta_{\text{hor}} = \Delta_{\text{hor}} \equiv 0$. Reversely, measuring Δ_{hor} and Δ_{hor} can be used to align the optics of the telescope.

The AC voltages V_i^{ac} of the QPD segments contain both amplitude and phase information of the interferometric beatnote between LO beam and RX beam for each segment, cf. Eq.(1.9). Both amplitudes A_i and phases φ_i of the AC signals are recorded with a digital phasemeter [10–13, 74]. The phase of the coherent sum of all four QPD segments is used as error signal of the phase-locked loop onboard the slave spacecraft and as intersatellite roundtrip ranging signal on the master spacecraft [43]. Additionally, the phasemeter computes relative tilts between LO beam and RX beam wavefronts using differential wavefront sensing (DWS, [75–80]).

The DWS principle, reduced to one tilt dimension, is illustrated in Fig.1.7, (2): Consider LO beam and RX beam with plane wavefronts incident on a split photodiode with two segments A, B. Without actuation of the LO beam with the steering mirror, local spacecraft yaw rotation leads to a relative wavefront tilt α . This causes

the integrated phases φ_A, φ_B of the QPD segments A, B to change differentially. By defining the DWS phase

$$\varphi_{\text{DWS,1D}} := \varphi_A - \varphi_B \quad (1.12)$$

we obtain a signal which, for small tilt angles $\alpha \lesssim 200 \mu\text{rad}$, is proportional to the wavefront tilt α ,

$$\varphi_{\text{DWS,1D}} = M_{\text{1D}} \cdot \alpha. \quad (1.13)$$

The proportionality factor M_{1D} converts relative geometric wavefront tilt between LO beam and RX beam to electronic DWS phase. The value of M_{1D} is large, of the order of 10,000 rad/rad, which is related to the ratio of laser frequency to wavelength. This large optical gain, in combination with common mode suppression for many noise sources, yields the excellent noise performance of DWS.

We can generalize Eqs.(1.12) and (1.13) to two dimensions by combining the phases of the QPD segments in Fig. 1.7, (1) appropriately:

$$\begin{aligned} \text{DWS}_{\text{hor}} &:= 0.5 \cdot (\varphi_A - \varphi_B + \varphi_C - \varphi_D), \\ \text{DWS}_{\text{ver}} &:= 0.5 \cdot (\varphi_A + \varphi_B - \varphi_C - \varphi_D), \\ \begin{pmatrix} \text{DWS}_{\text{hor}} \\ \text{DWS}_{\text{ver}} \end{pmatrix} &= M \cdot \begin{pmatrix} \delta\theta_{\text{yaw}} \\ \delta\theta_{\text{pitch}} \end{pmatrix}. \end{aligned} \quad (1.14)$$

Now M is a 2×2 matrix and $\delta\theta_{\text{yaw}}, \delta\theta_{\text{pitch}}$ are local spacecraft rotations leading to “horizontal” and “vertical” relative wavefront tilt between LO beam and RX beam at the beam splitter. Nominally, the QPD/DWS axes and the spacecraft’s axes of rotation are aligned, so that the off-diagonal elements of M are zero. Due to alignment tolerances of $\pm 2^\circ$, a small cross coupling is expected leading to off-diagonal matrix elements that are by a factor of 100 smaller than the diagonal elements.

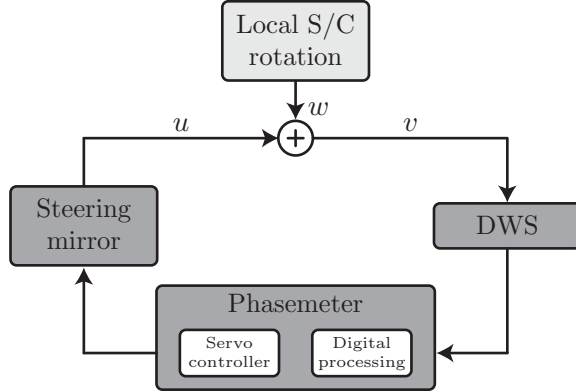
Note that the factor of 0.5 in Eq. (1.14) is conventional and depends on the specific implementation of DWS calculation, which is performed in the phasemeter. However, this only changes the calibration values of M .

1.4.5 The LRI beam steering method

The LRI beam steering method makes use of the proportionality between DWS signals and relative LO beam to RX beam tilt: By feeding the DWS signals back to the steering mirror electronics in closed-loop, the relative wavefront tilt is actively minimized to keep the LO beam and the TX beam coaligned to the RX beam under local spacecraft attitude jitter, cf. Fig. 1.1.

The beam steering control loop can be described by the block diagram in Fig. 1.8

Figure 1.8: This block diagram shows the control loop of the LRI beam steering for one of the two actuation axes.



(see e.g. [81]). Note that the diagram shows only one of the two actuation axes. Local spacecraft rotation leads to relative beam tilt which changes the relative phases on the QPD segments. According to Eq. (1.14), the resulting DWS signals are magnified compared to the beam tilt by the DWS transfer matrix M .

The QPR signals are processed by the phasemeter (PM), which is simplified in this picture by two boxes accounting for digital signal processing and the servo-controller of the loop. The gain of the servo can be adjusted to control the loop properties. The actuation signal from the phasemeter is passed on to the steering mirror (SM), which tilts the LO beam.

Each box in the diagram in Fig. 1.8 represents a complex, frequency-dependent gain function. The open-loop transfer function G of the beam steering loop is given by the product of those gain functions,

$$G = G_{\text{DWS}} \cdot G_{\text{PM}} \cdot G_{\text{SM}}, \quad (1.15)$$

where G_{DWS} is the DWS gain given by M (cf. Eq. (1.14)), G_{PM} is the phasemeter gain, and G_{SM} is the steering mirror gain. The steering mirror gain includes geometrical factors of 2 for horizontal and $\sqrt{2}$ for vertical tilts.

The open-loop transfer function G fully characterizes the beam steering control loop. It can be obtained by feeding in a disturbance w (cf. Fig. 1.8) and measuring the responses u and v . Since $u = vG$, we get

$$G = \frac{u}{v}. \quad (1.16)$$

Chapter 2

Items under test

We have looked at the LRI scheme in the previous chapter and we have identified two important subsystems that are further investigated in this thesis: the Triple Mirror Assembly (TMA) and the LRI Optical Bench. The development of TMA and LRI Optical Bench evolved in parallel with the development of the test environments which are presented in this thesis, so that TMA and optical bench units at various design stages have been investigated.

In this thesis, a total of four different TMA units ranging from prototype design studies to qualification models have been tested. Furthermore, the concept of the LRI Optical Bench has been implemented on breadboard level. This optical bench breadboard model (OBBM) was designed, fabricated, and tested within this thesis. In this chapter, the different test items are introduced with a special focus on the AEI in-house built OBBM.

2.1 Triple Mirror Assemblies

2.1.1 Fabrication of TMA units

In an early design study, two TMA versions were fabricated by a consortium led by the Australian National University (ANU, [50]). Both TMAs were kindly provided by ANU for test campaigns. In version one, a 600 mm long tube with 40 mm diameter made of carbon fiber-reinforced plastic (CFRP) was used as rigid structure between the TMA mirrors, thus the name CFRP TMA. In version two, a glass ceramic bar was used instead, leading to the name Glass TMA.

The CFRP TMA is shown in Fig. 2.1. It was the first TMA built within the GRACE Follow-On project and thus of particular value, since at an early stage, the design could be studied and performance tested [50, 52, 53, 82].

This is the basic assembly procedure [50] which, with some modifications and improvements, has been established for the following TMAs as well:

1. Assembly of mirror M1 and mirrors M2/M3 subassemblies. Perpendicularity between mirrors M2 and M3 is ensured by polishing procedures of the substrates.
2. Glass spacers are glued to CFRP tube as interface between the tube and the mirror subassemblies. Iterative polishing of spacers can later be used to adjust TMA beam coalignment.
3. M2/M3 subassembly is fixed via spacer interface to CFRP tube.
4. M1 subassembly is installed under observance with measurement tool (Fizeau interferometer or autocollimator) to assure proper alignment with respect to M2/M3 subassembly.

Glass-glass interfaces are fixed by optical contacting and hydroxide-catalysis bonding [83–86], while glass-CFRP interfaces are glued with space-qualified epoxides. The CFRP TMA has been investigated in the TMA beam coalignment test bed [53], which is described in subsequent Chaps. 3.1 and 4.1.

The Glass TMA in Fig. 2.2 was an alternative approach making use of the glass ceramic Zerodur[®], which has an ultra-low thermal expansion coefficient, as rigid structure between the M1 and M2/M3 subassemblies. The benefit of this approach is temperature stability and rigidity of the TMA, since via hydroxide-catalysis bonding between the mirror subassemblies and the Zerodur[®] bar, the whole TMA is virtually one monolithic glass piece.

However, concerns of this approach are that a large, rather filigree glass structure might be prone to damage during launch. Especially invisible micro-cracks that might

2.1 TRIPLE MIRROR ASSEMBLIES

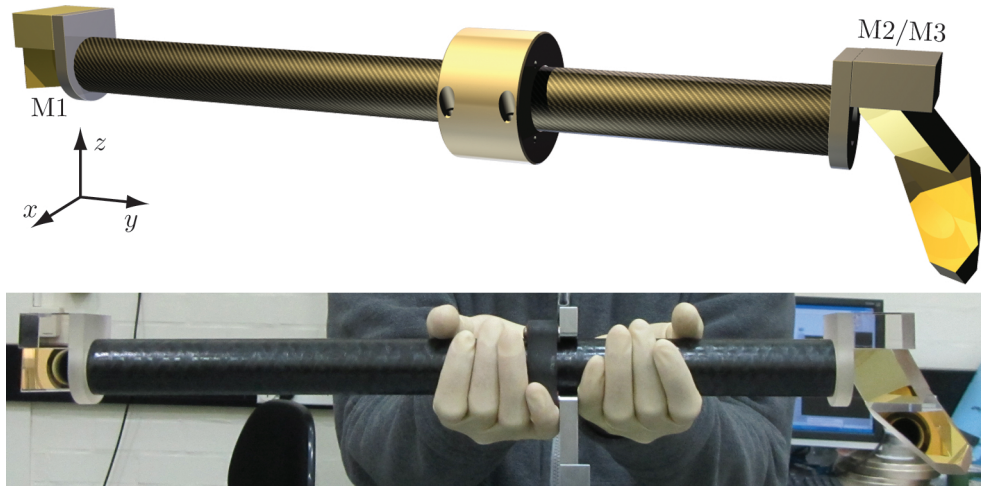


Figure 2.1: CAD model (top) and photograph (bottom, see also [53]) of the CFRP TMA. Mirror subassemblies M1 (left) and M2/M3 (right) are separated by a 600 mm long CFRP tube. The image of the CAD model was created with Autodesk[®] Inventor[®] using a CAD file which was kindly provided by ANU.

preexist in the Zerodur[®] material could lead to failure of the bar structure. This is why the glass bar approach was abandoned in favor of the CFRP tube approach in later TMA versions. For the Glass TMA, rotation-to-pathlength coupling has been investigated [54] in the TMA rotation-to-pathlength coupling test bed, see Chaps. 3.2 and 4.2.

Later on, as the design grew more mature, a TMA Development Model (DM, Fig. 2.3) and Qualification Model (QM) were designed and constructed by industry partners (STI/CAS). While TMA DM and TMA QM are identical in design, less effort was spent on optimizing the beam coalignment for the DM due to cost and schedule reasons. Both TMA DM and TMA QM were kindly provided by STI for test campaigns in the TMA rotation-to-pathlength coupling test bed, see Chaps. 3.2 and 4.2.

2.1.2 TMA coordinate systems

To measure the TMA properties and to reference them to the TMA units, suitable TMA-bound coordinate systems (TCS) have to be defined. We apply the coordinate definitions introduced in Chap. 1, Figs. 1.1 and 1.6. The orientation of the axes of the TMA-bound coordinate system is nominally identical with the orientation of the axes of the S/C coordinate system.

For the CFRP TMA, beam coalignment is investigated in this thesis. Since this

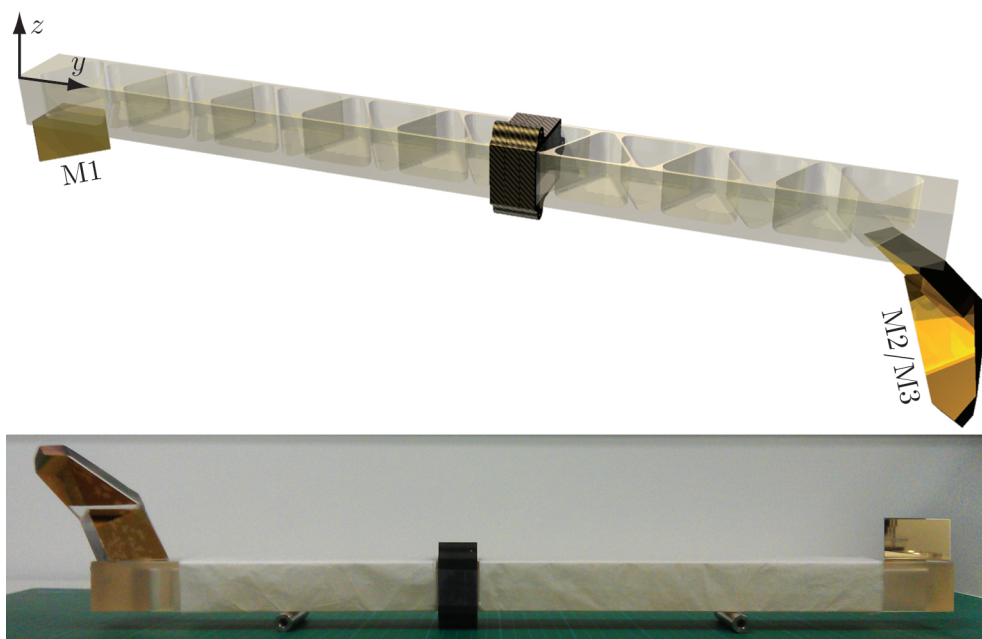


Figure 2.2: CAD model (top) and photograph (bottom, taken by ANU personnel, see also [54]) of the Glass TMA. The photograph is upside down for installation reasons. Top: Mirror subassemblies M1 (left) and M2/M3 (right) are separated by a 600 mm long glass ceramic bar. The image of the CAD model was created with Autodesk[®] Inventor[®] using a CAD file which was kindly provided by ANU.

2.1 TRIPLE MIRROR ASSEMBLIES

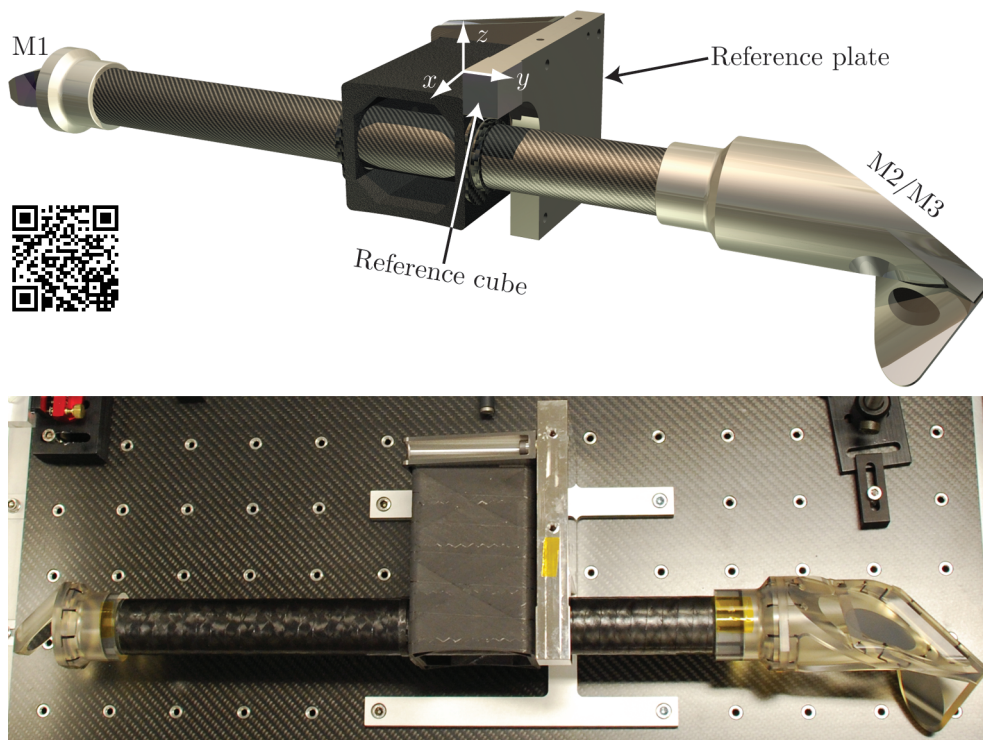


Figure 2.3: CAD model (top) and photograph (bottom) of TMA DM. Mirror sub-assemblies M1 (left) and M2/M3 (right) are separated by a 600 mm long CFRP tube. Top: The reference plate features a polished cube which can be used to define a coordinate system for CMM measurements. Before launch, the reference plate will be removed. The image of the CAD model was created with Autodesk[®] Inventor[®] using a CAD file which was kindly provided by STI. To see an animation of the three TMA models CFRP TMA, Glass TMA, and TMA DM, scan the QR code on the left side of the picture or go to www.gracefo.spacegravity.org/video4.

is a relative angular measurement, the origin of the coordinate system does not need to be defined. We fix the y -axis to be parallel to the CFRP tube, pointing from M1 to M2/M3, cf. Fig. 2.1 (top). The z -axis is perpendicular to the base of the mirror M1 subassembly so that the x -axis is antiparallel to the nominal incoming beam axis \vec{b}_{in} , cf. Chap. 1.3.1, Fig. 1.6.

For the other TMA units, this thesis investigates rotation-to-pathlength coupling. As we will learn in Chap. 3.2, this involves measurements with a coordinate measuring machine (CMM). This is why we define TMA-bound coordinate systems such that they can easily be measured with the CMM.

For the Glass TMA, we use the Zerodur[®] bar's front, top, and left faces to define the coordinate system, see Fig. 2.2 (top). The origin is defined as the intersection point of the three bar faces. The x -axis is perpendicular to the front face, the z -axis is perpendicular to the top face.

Both TMA DM and TMA QM feature a polished reference cube on a reference plate, see Fig. 2.3 (top). The reference plate is part of the TMA assembly and testing strategy and will be removed before launch. We use the cube's front, top, and left faces to define the coordinate system. The origin is defined as the intersection point of the three cube faces. The x -axis is perpendicular to the front face, the z -axis is perpendicular to the top face. TMA DM and TMA QM have been assembled in a way that nominal vertex position and nominal incident beam position and direction, which is antiparallel to x -axis and centered on TMA mirror M1, are referenced to the cube coordinate system.

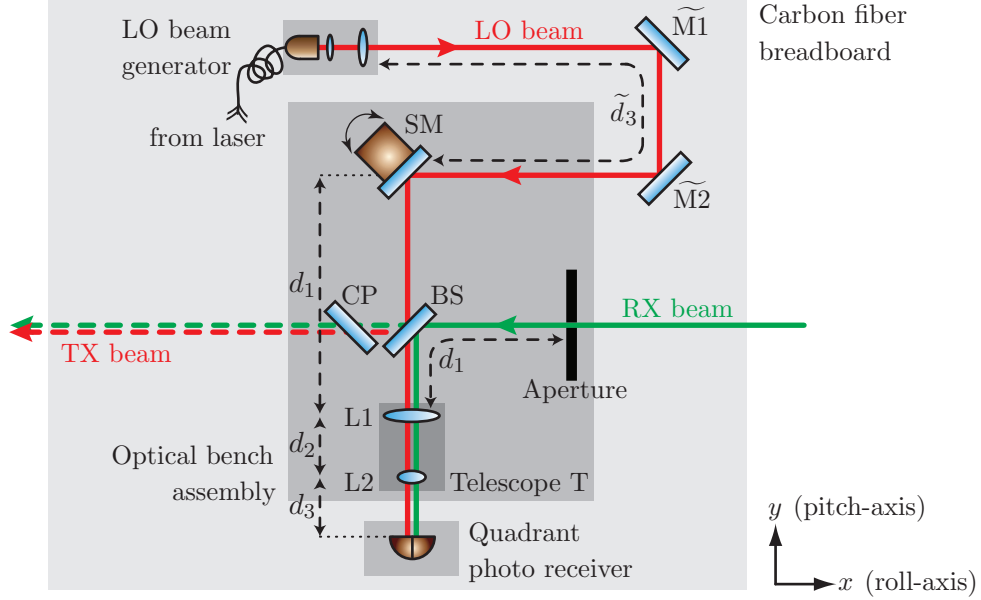


Figure 2.4: Schematic of OBBM mounted on a carbon fiber breadboard. The OBBM is divided into three functional parts: 1) The LO beam generator delivers a laser beam with the desired beam profile. 2) On the optical bench assembly, RX beam and LO beam are interfered on a beam splitter (BS) and demagnified with a telescope. The LO beam can be tilted with a steering mirror (SM) in two axes. The compensation plate (CP) suppresses rotation-to-pathlength coupling caused by the BS. 3) The quadrant photo receiver (including a QPD) converts the optical beatnote between the two beams into a voltage.

2.2 Optical bench breadboard model

For the investigations in this thesis, an optical bench breadboard model (OBBM) was designed and fabricated at the AEI as prototype of the LRI Optical Bench following the LRI design described in Chap. 1.2. The motivation was to have a prototype to work with at an early stage in the project. Furthermore, the OBBM served well in preparing the LRI Optical Bench test bed, cf. Chaps. 3.3 and 4.3, which is presently employed to investigate industry-built LRI Optical Bench engineering models from STI [87].

When designing the OBBM, we can identify three functional subunits (Fig. 2.4):

1. The optical bench assembly (OBA), on which LO beam and RX beam are interfered on a beam splitter (BS). Telescope T images both steering mirror (SM) surface and aperture plane onto a QPD. Furthermore, the LO beam can be tilted in two axes with the SM.

2. The LO beam generator, which delivers the LO beam.
3. The quadrant photo receiver (QPR) including a QPD, which converts the optical beatnote between LO beam and RX beam into a voltage.

The fabrication strategy is to design and build each subunit individually and then assemble the OBBM on a carbon fiber breadboard of sufficient size. In the following, design and construction of each OBBM subunit is described.

2.2.1 Optical bench assembly

The tasks of the OBA are (see Fig. 2.4):

- Provide an 8 mm diameter aperture to clip the RX beam.
- Provide two-axes beam steering for the LO beam.
- Interfere LO beam and RX beam on a beam splitter (BS).
- Suppress linear rotation-to-pathlength coupling caused by the BS with a compensation plate (CP).
- Suppress beamwalk on the QPD caused by local S/C rotations by simultaneously imaging aperture plane and steering mirror (SM) plane on the QPD with telescope T.

Let us begin the OBA design by choosing an aperture with 8 mm diameter and assuming a QPD with 1 mm diameter, which is the baseline for the LRI. A telescope with 1/8 demagnification is required to adjust the diameter of the RX beam to the QPD diameter. To keep the design reasonably compact, we choose lens L1 for the OBBM telescope (cf. Fig. 2.4) with a focal length of $f_1 = 81.46$ mm for a laser wavelength of 1064 nm (Linos/Qioptiq GmbH & Co. KG). With a lens L2 that has a focal length of $f_2 = 10.20$ mm (Linos/Qioptiq GmbH & Co. KG), we achieve the required demagnification factor.

The OBBM telescope has been designed with a Matlab[®]-based ABCD matrix raytracing simulation. The telescope is described by the thick lens approach. The distances d_1 , d_2 , and d_3 , which are sketched in Fig. 2.4, are the distances between the telescope's object plane and the first principle plane of lens L1, between the second principle plane of L1 and the first principle plane of L2, and between the second principle plane of L2 and the telescope's image plane, respectively.

For proper imaging, one has to choose $d_2 = f_1 + f_2$. By making the further choice $d_3 = 10$ mm, $d_1 = 94.22$ mm is automatically fixed, which is a convenient distance to

place beam splitter, aperture, and steering mirror. The distances d_1 , d_2 , d_3 are shown in Fig. 2.4. The ABCD system matrix M_T of the telescope T is calculated to be

$$M_T = \begin{pmatrix} -0.1252 & 0 \\ 0 & -7.9863 \end{pmatrix}. \quad (2.1)$$

We have thus designed a telescope which images an object located at the object plane at a distance d_1 in front of lens L1 to the image plane at a distance d_3 behind lens L2. The image is reversed and demagnified by a factor of 1/8, while the angle of a ray in the object plane is reversed and magnified by a factor of 8. Most importantly, the off-diagonal elements of M_T are zero. This means that there is no coupling between beam tilt at the aperture plane or the steering mirror surface and lateral beam offset on the QPD, which is located at the image plane at a distance d_3 behind lens L2. Thus beamwalk incurred by local S/C tilts is canceled by the telescope.

After the telescope design, the remaining OBA components are selected (cf. Fig. 2.4): aperture stop (manufactured by AEI workshop, 8 mm diameter), steering mirror (PI GmbH & Co. KG, S-325.3SD, controller: E-616.S0), beam splitter (Melles Griot GmbH, customized, $45 \times 35 \times 5$ mm³, 95% reflective/AR coating), and compensation plate (Melles Griot GmbH, customized, $45 \times 35 \times 5$ mm³, AR/AR coating). Both beam splitter and compensation plate have wedge angles of some arcmin, so that residual ghost beam reflections from the AR coatings leave the optical axis.

In the next step, the OBA design is completed with the chosen components on a 160×260 mm² aluminum baseplate using the CAD program Autodesk[®] Inventor[®]. The distances d_1 , d_2 , d_3 as determined above are applied. Furthermore, the compensation plate is placed perpendicular to the beam splitter. The construction strategy is to place the aperture stop and mounts for all OBA components to mechanical stops on the baseplate defined by bolts in drill holes (3 per OBA component) with below ± 100 μ m positional accuracy. The mounts themselves serve as mechanical stops for the optics and the steering mirror. Baseplate, mounts, and aperture stop were fabricated from aluminum by the AEI mechanical workshop.

The step-by-step assembly is illustrated in Fig. 2.5: (1) Positioning holes are drilled into the baseplate. (2) Steel bolts are inserted into the holes as mechanical stops for the OBA parts (3 bolts per item). (3) The mount for the steering mirror is glued to the baseplate by sliding it to the bolts, see close-up (4). The glue is a two-component epoxide. During glueing, the baseplate is installed at an angle so that the mount is held in place by gravity. (5) The steering mirror is inserted into its mount. The steering mirror axes are aligned to the baseplate within $\pm 1^\circ$ by performing mirror tilts under observation with an autocollimator (Möller-Wedel GmbH, ELCOMAT direct).

(6) Aperture stop, mounts for lenses L1 and L2, and mounts for beam splitter and compensation plate are glued to the baseplate as described for the steering mirror mount.

After glueing the mounts, the optics are clamped into the mounts. Their position is fixed by mechanical stops. Only lens L2 can be moved along the nominal beam axis to adjust the outgoing beam profile. The CAD model of the fully assembled OBA is shown in Fig. 2.6. The legs under the baseplate were added to adjust the OBA beam height within the OBBM. A photograph of the OBA is shown in Fig. 2.7.

2.2.2 LO beam generator

The LO beam generator shall deliver a beam with Gaussian beam waist diameter of 5 mm to the OBA, which is the current LRI baseline. The nominal beam waist position shall be on the steering mirror surface, i.e., the wavefront shall be flat on the steering mirror. While commercial fiber collimators exist which promise beams with 5 mm diameter, experience has shown that the combination of beam divergence and beam diameter is poorly controlled by commercial devices.

The approach chosen here for generating an appropriate LO beam was to start with a commercial fiber collimator with rather small beam diameter and then expand the beam with a two-lens telescope to the desired size, see Fig. 2.8. The selected fiber collimator has an adjustable lens (Schäfter&Kirchhoff GmbH, SUK60FC-4-A11-03), which can later be used to fine-tune the LO beam generator after fabrication.

The intensity profiles of the fiber collimator beam are measured with a CCD (charge-coupled device) camera (DataRay Inc., WinCamD™) over a distance of more than one meter, covering the waist position of the beam. From these, a Gaussian beam waist diameter of 1.8 mm and the waist position have been determined. Using an ABCD matrix raytracing simulation similar to Sec. 2.2.1 and q-parameter propagation, a suitable combination of lenses $\widetilde{L1}$ and $\widetilde{L2}$ was determined. This lens combination transforms the beam leaving the fiber collimator to the desired beam size. Additionally, it produces a waist position in a convenient distance to be placed on the OBA steering mirror surface.

A suitable lens combination was found to be $\widetilde{L1}$ with focal length $\widetilde{f}_1 = 35.38$ mm and $\widetilde{L2}$ with focal length $\widetilde{f}_2 = 100.83$ mm (Thorlabs Inc., LA1027-C and LA1509-C), which should increase the beam size by a factor of almost 3. The distance between fiber collimator and telescope was chosen as $\widetilde{d}_1 = 20$ mm for compactness, cf. Fig. 2.8, whereas $\widetilde{d}_3 = 200$ mm between LO beam generator and waist position of generated beam was chosen to have enough space for coupling the beam into the OBA with mirrors $\widetilde{M1}$, $\widetilde{M2}$ (cf. Fig. 2.4) and for placing the beam waist on the steering mirror

2.2 OPTICAL BENCH BREADBOARD MODEL

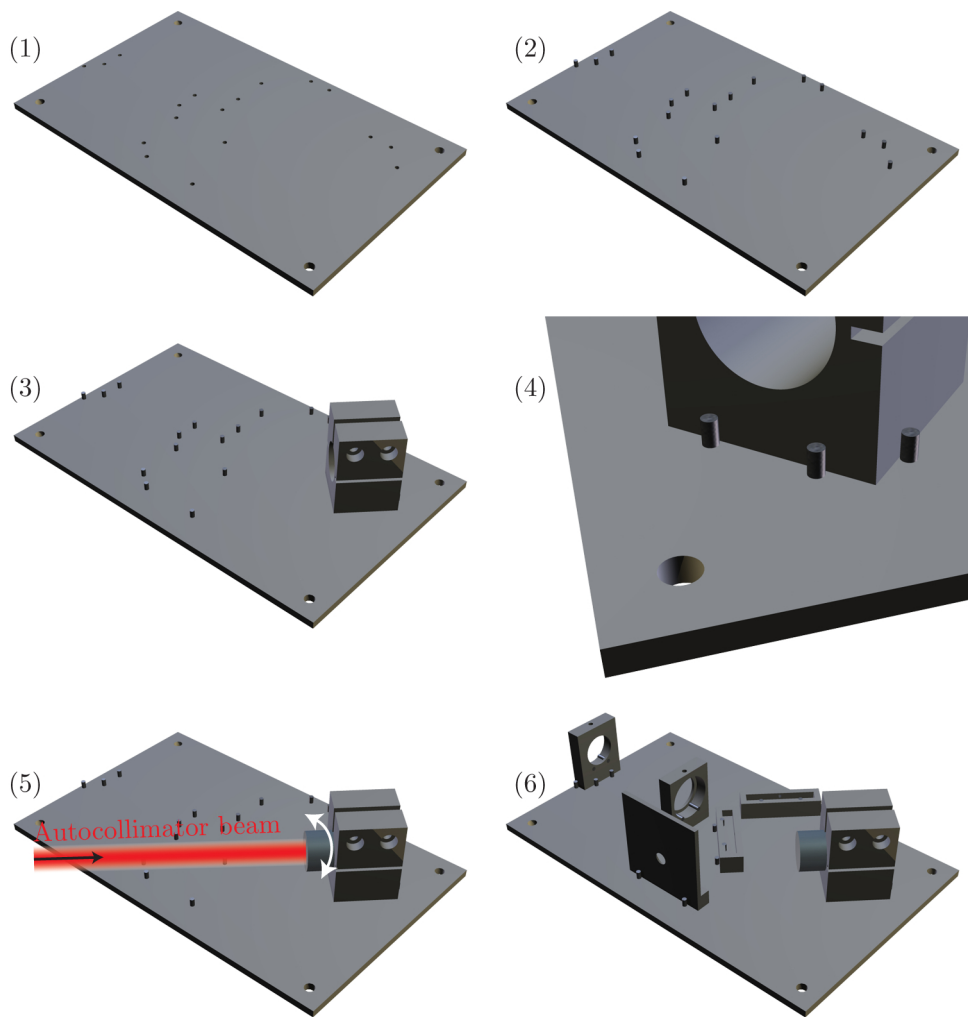


Figure 2.5: Assembly steps of OBA. (1) Holes are drilled into baseplate. (2) Steel bolts are inserted into the drill holes. (3) The steering mirror mount is placed to the three steel bolts which define its position and orientation and then glued. (4) Close-up of (3). (5) The steering mirror is mounted and aligned to the baseplate with an autocollimator. (6) All other components are placed and glued.

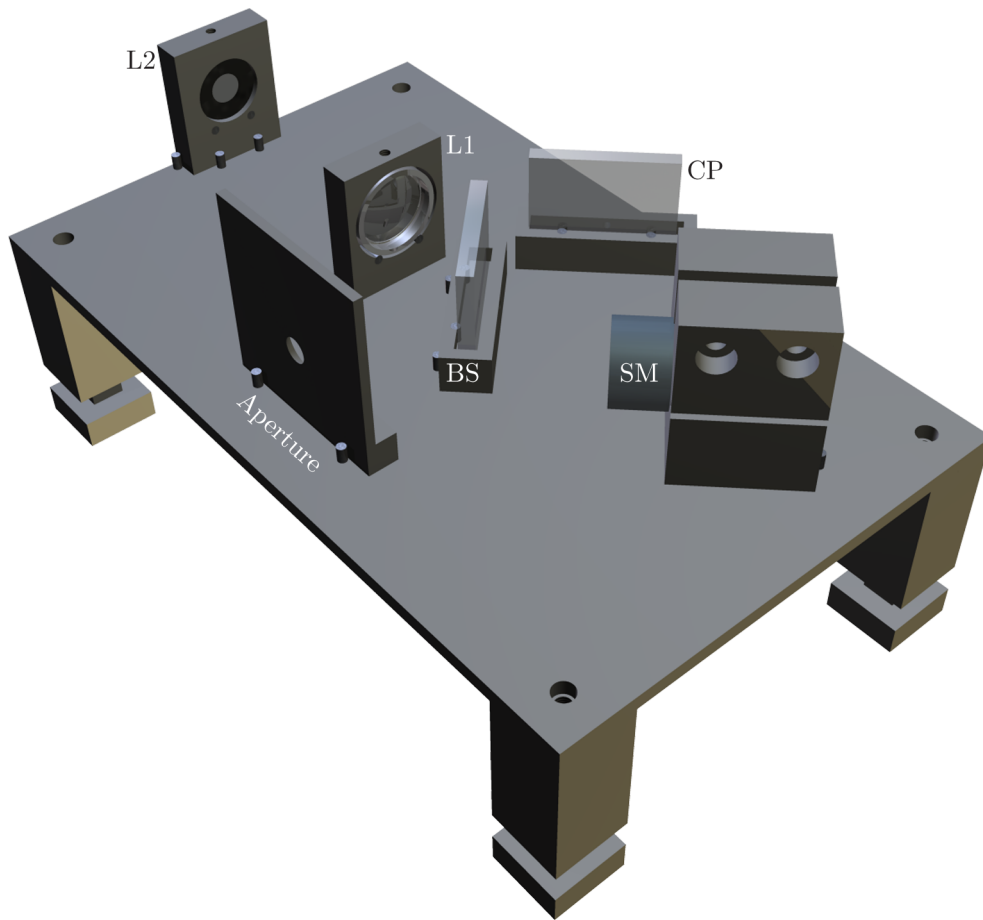


Figure 2.6: CAD model of fully assembled OBA. The optics are installed in the mounts as well. For component explanation, see Fig. 2.4.

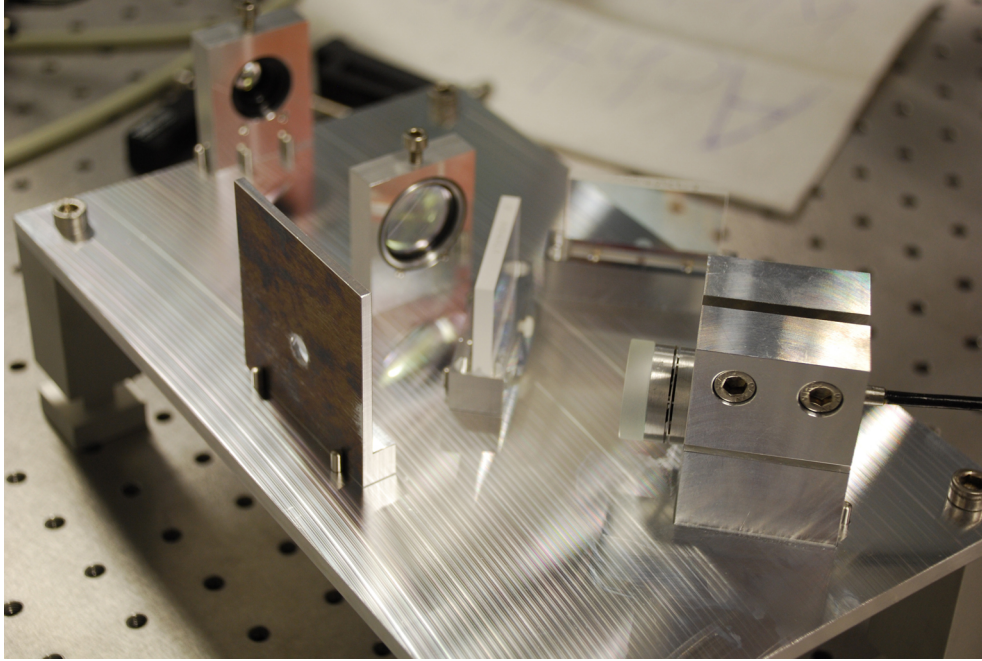
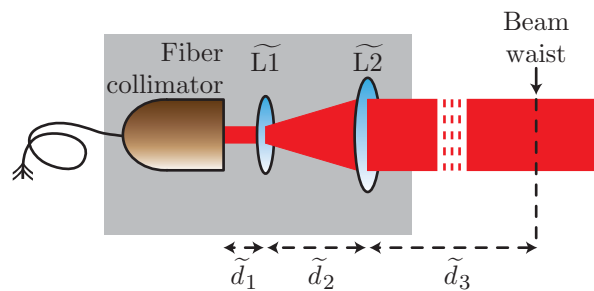


Figure 2.7: Photograph of OBA after assembly. All optics mounts are positioned via three steel bolts in precision drill holes and glued to the baseplate. The optics (beam splitter, compensation plate, steering mirror with actuator, lens L1, and lens L2) are held in place by screws. While the position of lens L1 is defined by the stop of the mount, the position of lens L2 along the beam axis can be adjusted.

Figure 2.8: Schematic of LO beam generator. The beam from a commercial fiber collimator is expanded with lenses $\tilde{L}1$, $\tilde{L}2$. The nominal waist position of the generated beam is located at $\tilde{d}_3 = 200$ mm, which is a convenient distance to place the OBBM steering mirror, cf. Fig. 2.4.



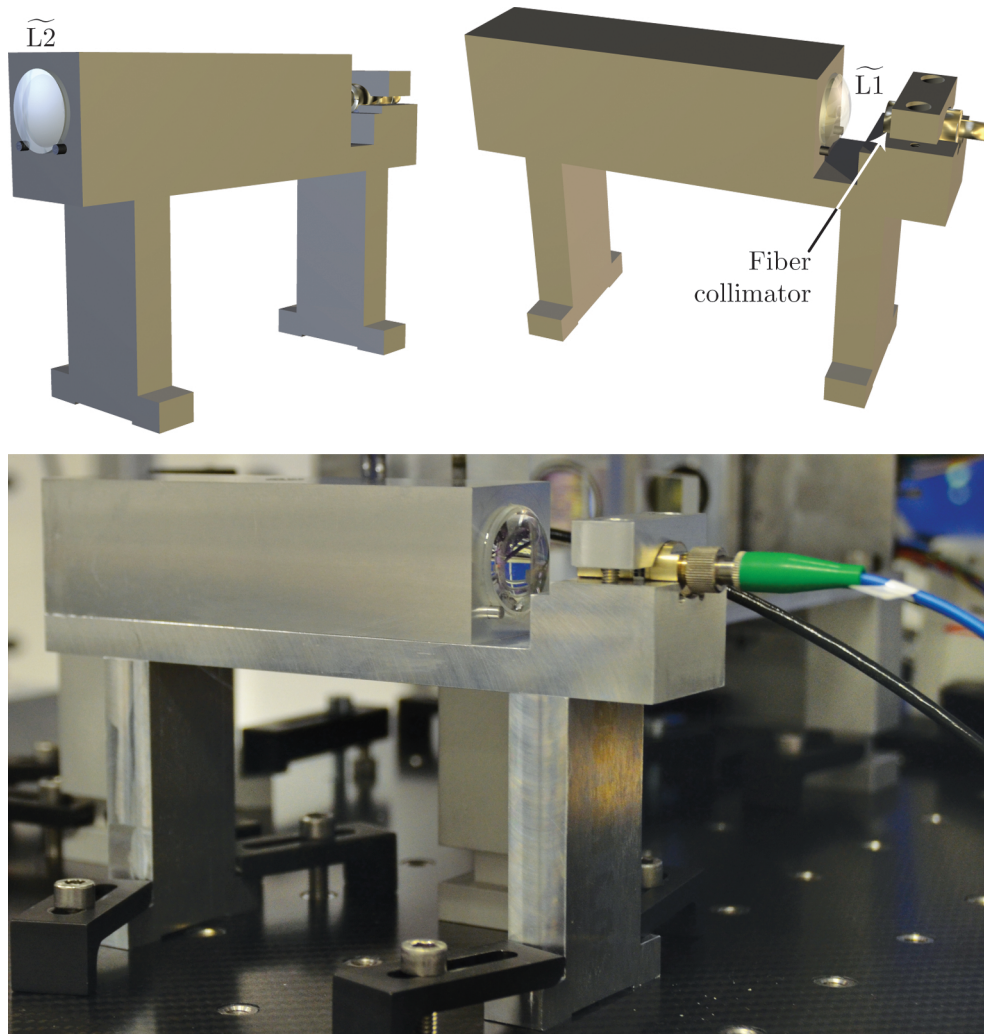


Figure 2.9: *Top: CAD model of LO beam generator from two perspectives. Bottom: Photograph of assembled LO beam generator.*

surface.

Consecutively, a CAD model of the LO beam generator was created consisting of an aluminum structure holding fiber collimator, lens $\widetilde{L1}$, and lens $\widetilde{L2}$, which is shown in Fig. 2.9 (top). All mechanical parts were manufactured from aluminum at the AEI workshop. Lenses $\widetilde{L1}$ and $\widetilde{L2}$ were glued to an aluminum spacer with a two-component epoxide glue. The fiber collimator could be clamped at a defined distance.

The simulations have shown that the parameters of the beam produced by the LO beam generator depend very critically on lens parameter tolerances and on tolerances

of the distance \tilde{d}_2 between $\tilde{L}1$ and $\tilde{L}2$. Especially the waist position varies by many meters, if the distance between $\tilde{L}1$, $\tilde{L}2$ is changed by less than 100 μm . Since this is of comparable size with the anticipated workshop manufacturing tolerances, a fiber collimator with an adjustable lens position was chosen to have a means of fine-tuning the LO beam generator after construction.

The LO beam generator was fine-tuned while observing the generated LO beam with a Shack-Hartmann sensor (SHS, Imagine Optics S.A., HASO3-128-GE2). The SHS was placed at distance $\tilde{d}_3 = 200$ mm behind lens $\tilde{L}2$, as this is the foreseen distance to the steering mirror in the fully assembled OBBM (see Fig. 2.4). Minimal adjustment of the position of the fiber collimator lens led to a flat wavefront on the SHS.

Consecutively, wavefront and intensity profile of the produced LO beam were measured, see Fig. 2.10, at distances of 70 mm (top), 200 mm (middle), and 700 mm (bottom) behind lens $\tilde{L}2$. Fitting Zernike polynomials up to 2nd order, “piston”, “tilt”, and “defocus”, to the phasefronts in Fig. 2.10 (left column) yields wavefront radii of curvature of -1.3 km (top), -198 km (middle), and 0.7 km (bottom).

Within the SHS measurement accuracy, a radius of curvature of -198 km cannot be distinguished from a wavefront curvature of zero. The sign change in radius of curvature shows that the beam waist lies between 70 mm and 700 mm. At the nominal waist position $\tilde{d}_3 = 200$ mm, a peak-to-valley wavefront error of 120 nm is observed.

Additionally, the LO beam intensity profile was investigated with a CCD camera, since it offers a higher spatial resolution than the intensity profiles taken with the SHS. Beam intensity profiles were recorded at five distances up to 1 m. The Gaussian beam diameter fitted to the intensity distributions is 4.6 mm and does not change noticeably over the investigated distance.

Averaging over the five measurements yields a beam diameter of (4.64 ± 0.05) mm. The deviation from the desired beam diameter of 5 mm can be attributed to lens parameter tolerances. A typical image taken with the CCD camera at distance $\tilde{d}_3 = 200$ mm is shown in Fig. 2.11. The beam shape is very symmetrical with a ratio of minor to major axis of 0.966 ± 0.005 .

2.2.3 Quadrant photo receiver

The QPR used on the OBBM is the elegant breadboard model (EBB) of the LRI QPR which was kindly provided by the Deutsches Zentrum für Luft- und Raumfahrt (DLR Berlin). The EBB QPR features a 1 mm diameter InGaAs QPD (OSI Optoelectronics AS, FCI-InGaAs-Q1000) with 44 μm slit width, as determined with an optical microscope.

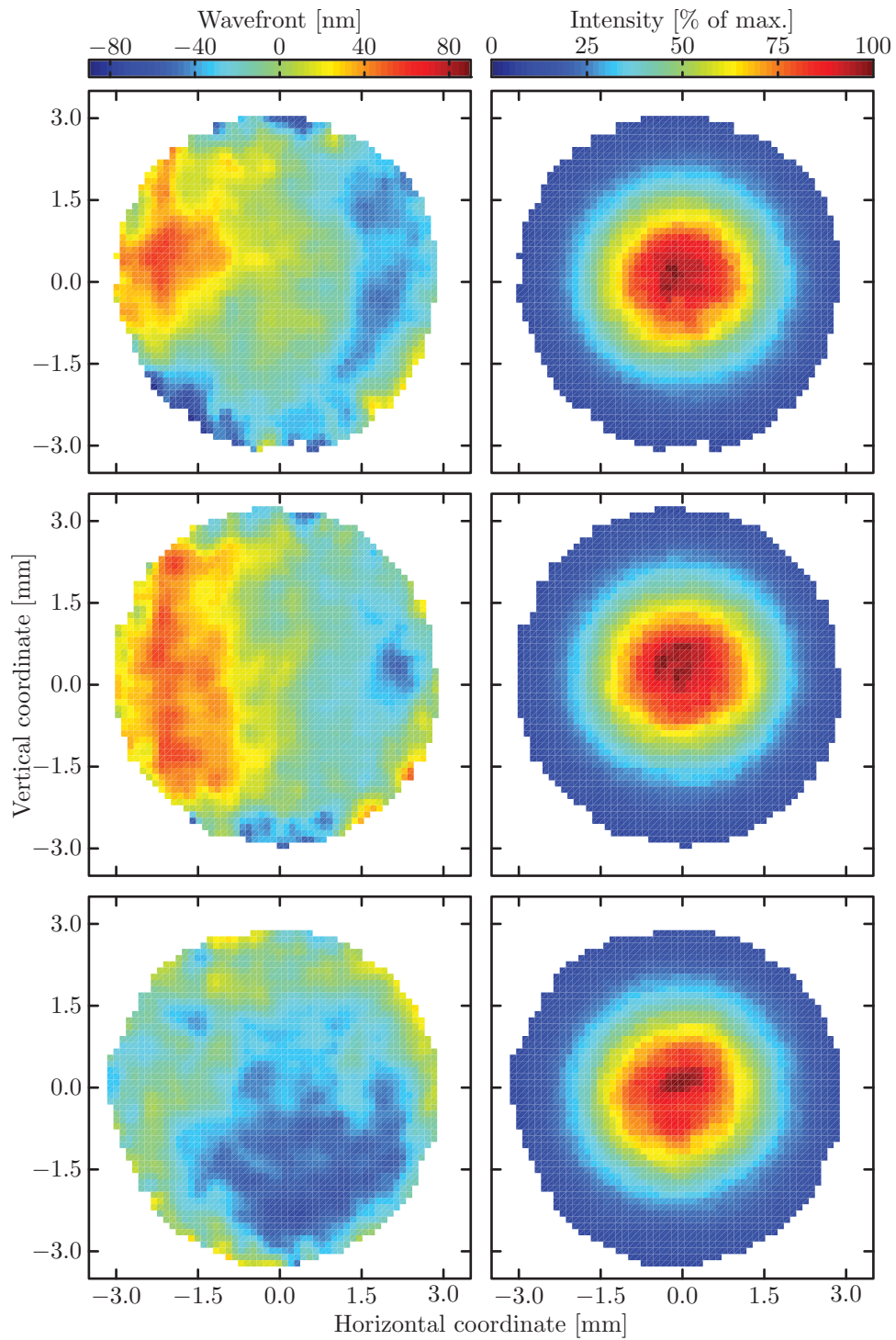
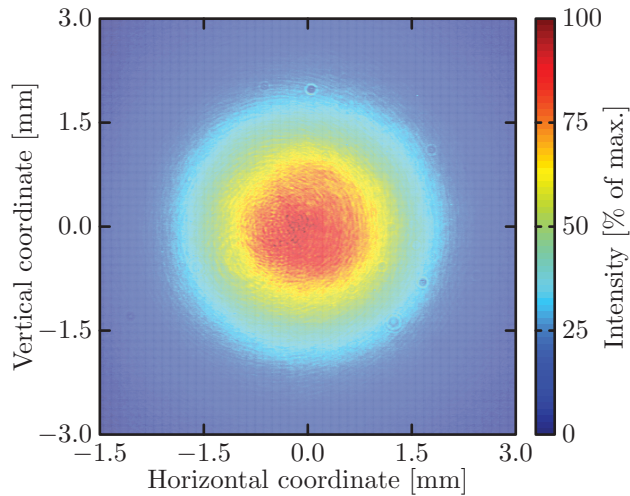


Figure 2.10: *LO* beam wavefront (left) and intensity profile (right) recorded with *SHS*. Images taken behind $\widehat{L}2$ at 70 mm (top), 200 mm (middle), and 690 mm (bottom).

Figure 2.11: *Image of LO beam intensity profile taken with CCD camera in distance $\tilde{d}_3 = 200$ mm behind lens \tilde{L}_2 . The small circular spots are caused by dust particles on the camera's neutral density filter and do not influence the measurement.*



A photograph of the EBB QPR is shown in the left inset of Fig. 2.13. The EBB QPR is mounted on a 3-axes translation stage with micrometer screws so it can be aligned both along the beam axis and transversally.

2.2.4 Integration of OBBM subunits

The OBBM subunits are integrated on a $400 \times 700 \times 50$ mm³ carbon fiber breadboard with aluminum honeycomb structure (CarbonVision GmbH, customized), which is used for weight considerations. CAD model and photograph of the integrated OBBM are shown in Figs. 2.12 and 2.13, respectively.

In a first step, the OBA is positioned on the carbon fiber breadboard. Mechanical axes are coarsely aligned to a few mrad. Then the LO beam generator is placed and connected to an optical fiber, which delivers light from a laser source with 1064 nm wavelength (Mephisto 500, Innolight GmbH, now Coherent Inc.). The LO beam is guided over the mirrors \tilde{M}_1 , \tilde{M}_2 such that it travels a distance $\tilde{d}_3 = (200 \pm 3)$ mm from the LO beam generator to the steering mirror surface on the OBA (cf. Fig. 2.4). The LO beam is aligned to the OBA telescope axis by iteratively adjusting near and far field beam positions with mirrors \tilde{M}_1 , \tilde{M}_2 and alternately removing and inserting lenses L1, L2 of the OBA telescope. During the alignment process, the LO beam position behind lens L2 is monitored with a CCD camera. When properly aligned, the LO beam position on the CCD camera does not change noticeably when inserting lenses L1, L2.

Next, the distance d_2 between OBA telescope lenses L1 and L2, cf. Fig. 2.4, is fine-tuned by adjusting the L2 position along the beam with a micrometer screw.

The straightforward approach, which is placing the SHS at the distance d_3 behind lens L2 and adjusting the position of L2 until a flat wavefront is measured, could not be realized for two reasons. Firstly, the distance of $d_3 = 10$ mm, cf. Sec. 2.2.1, is too short such that the SHS housing and the L2 mount were obstructing each other. Secondly, the expected beam diameter at d_3 behind L2 of below 0.6 mm is too small to be investigated with the SHS.

Therefore, the intensity profile of the LO beam is measured with a CCD camera at various distances behind lens L2 to determine Gaussian waist diameter and waist position. In a Matlab[®]-based raytracing simulation using ABCD matrix formalism and q-parameter propagation, the LO beam is propagated with beam parameters as determined in Sec. 2.2.2 through the OBA telescope. By comparing the measured beam parameters with the simulated beam parameters, the longitudinal position of lens L2 can be corrected. This process is iteratively applied down to an L2 placement precision below ± 50 μm .

Finally, the QPR mounted on a 3-axes translation stage is installed. The beam is centered on the QPD by translating the QPR transversally to the beam and minimizing the DPS signals, cf. Chap. 1.4.4. The alignment of the QPD position along the beam direction to place the QPD at the image plane of the OBA telescope is part of the test results presented in Chap. 4.3.2.

2.2 OPTICAL BENCH BREADBOARD MODEL

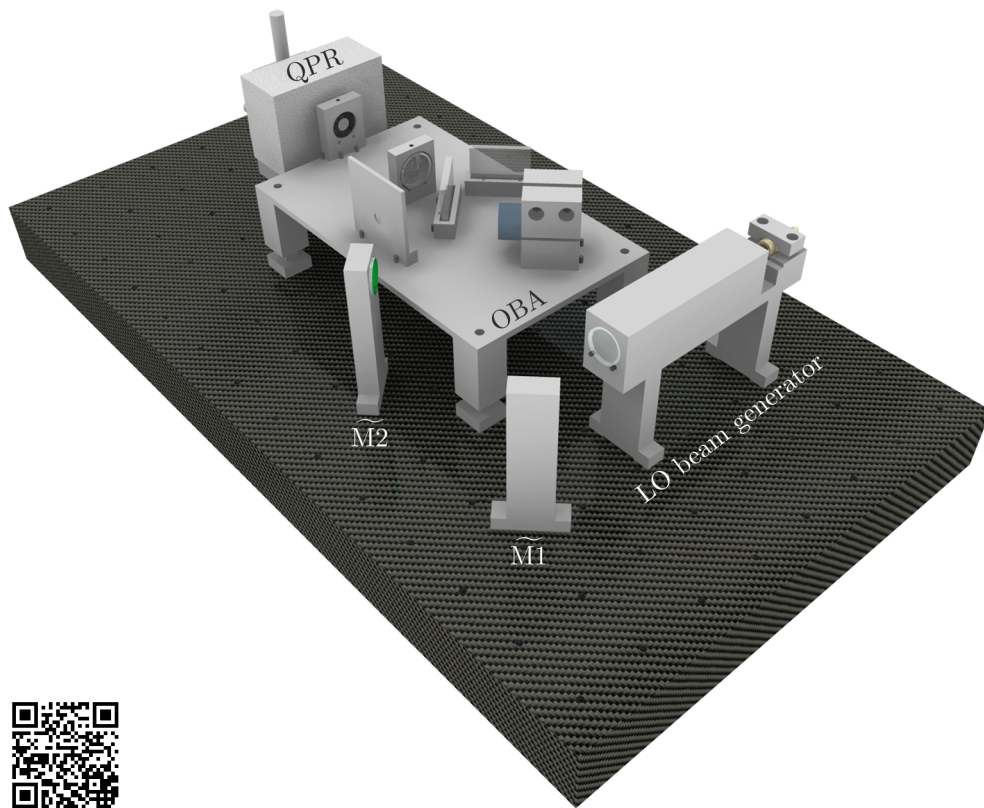


Figure 2.12: *CAD model of fully assembled OBBM. The OBBM subunits OBA, LO beam generator, and QPR are integrated on a $400 \times 700 \times 50 \text{ mm}^3$ carbon fiber breadboard. The LO beam is fed into the OBA with mirrors $\widetilde{M1}$, $\widetilde{M2}$. You can watch an animation of the OBBM CAD model by scanning the QR code in the lower left corner of the picture or by going to www.gracefo.spacegravity.org/video5.*

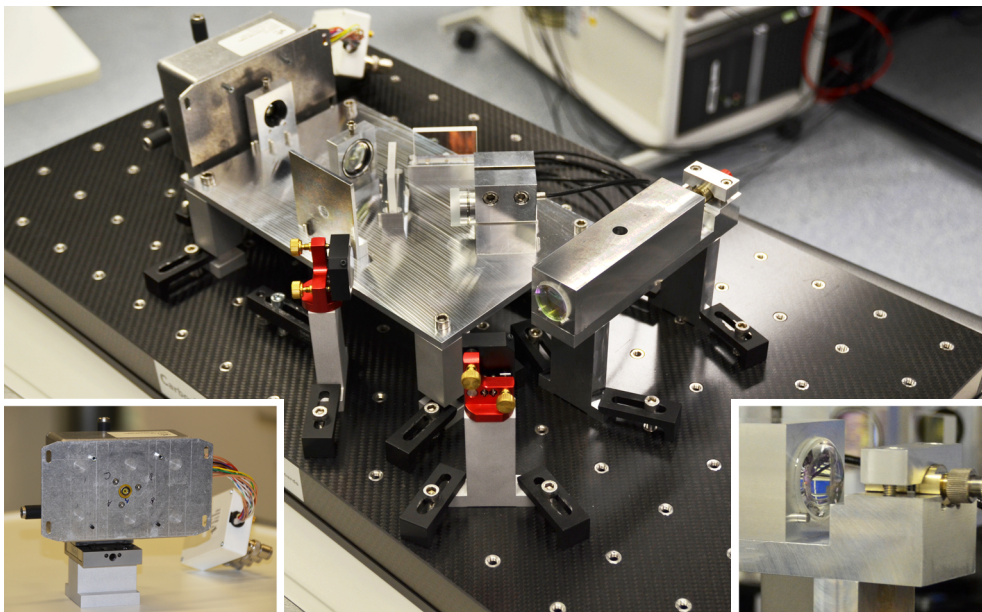


Figure 2.13: The picture shows the fully assembled OBBM with the subunits OBA, LO beam generator, and QPR integrated on a carbon fiber breadboard. In the left inset, the QPR mounted on a 3-axes translation stage can be seen, while the right inset shows a close-up of lens $L1$ of the LO beam generator.

Chapter 3

Test environments for LRI components

This chapter introduces the test environments that have been developed in this thesis to test two important LRI components: the TMA and the LRI Optical Bench. This chapter is divided into three sections. In Sec. 3.1, the TMA beam coalignment test bed is introduced, while Sec. 3.2 explains the TMA rotation-to-pathlength coupling test bed. Finally, Sec. 3.3 is dedicated to the LRI Optical Bench test bed.

3.1 TMA beam coalignment test bed

The essential property of the TMA is to retroreflect an incoming beam \vec{b}_{in} (cf. Fig. 1.6). As we have seen in Chap. 1.2, this property ensures, in combination with the LRI beam steering method, that the outgoing beam \vec{b}_{out} is sent back into the direction of the distant S/C. If incoming and outgoing beams are not sufficiently well coaligned, the light power received by the distant S/C will be reduced so that the establishment of the laser link might be impeded. The initial beam coalignment requirement for the TMA before environmental tests is 10 μrad , cf. Chap. 1.3.3.1. This is to be verified with the TMA beam coalignment test bed.

The methods and procedures that have been developed for this test bed within this thesis have been published [53].

The TMA beam coalignment test bed as described in Sec. 3.1.1 has been installed at CSIRO (Sydney, Australia) in collaboration with CSIRO personnel, following a concept which had previously been developed at CSIRO. The data processing and evaluation procedure to recover the TMA beam coalignment information which is described in Secs. 3.1.2 and 3.1.3 has been solely developed within this thesis.

Retroreflectors and their properties have been studied for many years due to their usefulness in various applications [59–63]. For characterization, either dot patterns recorded with an autocollimator [64, 88] or interferograms measured with a phase-shifting Twyman-Green or Fizeau interferometer [89–96] can be used. The dot patterns or the interferograms are recorded by fully illuminating the retroreflector under test.

However, for the TMA, the task becomes more intriguing. The large separation of TMA mirror M1 and the M2/M3 subassembly of 600 mm (cf. Chap. 2.1) would require an autocollimator beam or an interferometer beam of comparable size, which is not available. Standard autocollimators have a measurement beam diameter of roughly 40 mm, while large aperture interferometers come with 150 mm diameter optics. Manufacturing a customized device would require unreasonable effort and expense.

There are two common approaches for measuring large aperture optics: sub-aperture stitching interferometry [97] and “Ritchey-Common” or “Skip-Flat” tests [98–100]. However, for the TMA, subaperture stitching interferometry cannot be applied, since incoming and outgoing beam are laterally displaced by 600 mm. “Ritchey-Common” and “Skip-Flat” tests reduce the effective aperture of the investigated optics by installing the optics at a large angle of incidence of many degrees, but this is far beyond the clear opening angle of the TMA, which is a few mrad.

For this reason, a new approach for characterizing TMA beam coalignment had

to be developed in the GRACE Follow-On project. For the different TMA units, the approaches have slightly varied. However, all of them require some sort of reference bar, which extends the aperture of the used inspection tool to the required size, i.e., the distance between TMA mirror M1 and M2/M3 subassembly of 600 mm. The inspection tool is either an autocollimator or a large-aperture homodyne interferometer.

In this thesis, the TMA beam coalignment test bed comprises a combination of a flat 650 mm long reference bar and a phase-shifting Fizeau interferometer. Furthermore, the investigations focus on the measurement concept and demonstrate the achievable accuracies instead of exercising the full scope of necessary test runs, which would involve beam coalignment investigation under thermal cycling and in vacuum [82]. However, in principle the test bed presented in this thesis could be extended to support such test conditions as well.

3.1.1 Setup of the TMA beam coalignment test bed

A schematic of the TMA beam coalignment test bed is shown in Fig. 3.1. The key component of this setup is a polished, flat reference bar (RB) made of Zerodur[®] for its low thermal expansion coefficient. The RB has been fabricated by CSIRO.

With the RB, the auxiliary mirrors $\widetilde{M}1$, $\widetilde{M}2$ are aligned parallel to each other by simultaneously observing back-reflections from the left and right side of the RB, RB_L and RB_R respectively. The auxiliary mirrors are adjusted such that the interferogram of RB_R matches the one of RB_L .

Effectively, the parallel mirrors $\widetilde{M}1$, $\widetilde{M}2$ expand the 150 mm diameter aperture of the homodyne phase-shifting Fizeau interferometer (Wyko[®] Corp., Wyko[®] 6000) to the desired size of 600 mm, which is the distance of TMA mirror M1 and M2/M3 subassembly.

The RB topography has been recorded by CSIRO personnel using a “Skip-Flat” test [98–100], cf. Fig. 3.2. The RB flat surface has a rectangular shape of $650 \times 79 \text{ mm}^2$. To fully illuminate it with the interferometer laser beam, the RB was installed under an angle of incidence of $\alpha = 40^\circ$ leading to an effective aperture of $116 \times 79 \text{ mm}^2$. The return flat (RF) topography with a peak-to-valley excursion of less than 70 nm had previously been measured and is subtracted.

The measured topography of the RB is displayed in Fig. 3.3. Additionally, a photograph of the RB is shown as inset. The RB exhibits a concave topography with a peak-to-valley excursion of 600 nm. Differences $\varphi_{q,RB\text{polish}} = \varphi_{q,RB\text{polish}_R} - \varphi_{q,RB\text{polish}_L}$ between angles on the right and left side of the RB, $\varphi_{q,RB\text{polish}_R}$ and $\varphi_{q,RB\text{polish}_L}$ respectively, are smaller than $4 \mu\text{rad}$. This leads to a corresponding alignment error of the mirrors $\widetilde{M}1$, $\widetilde{M}2$, which is considered in the measurement data evalua-

tion (cf. Sec. 3.1.2).

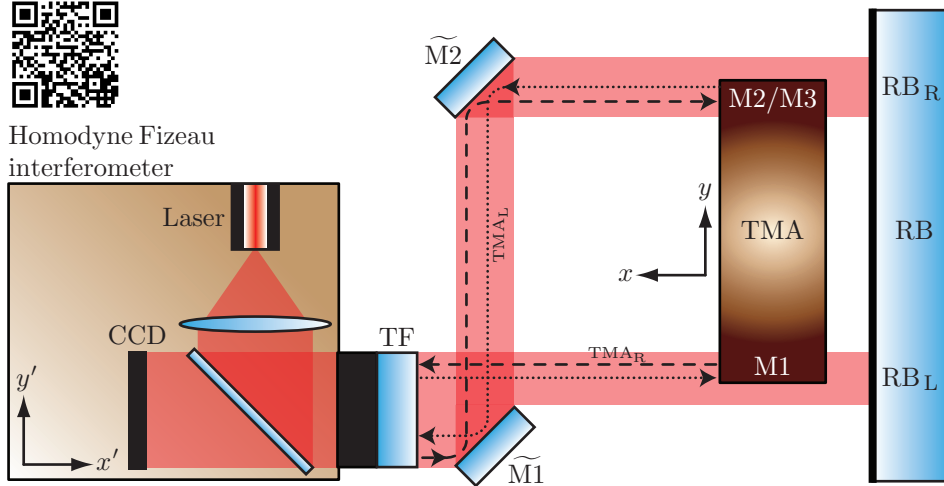


Figure 3.1: Setup to measure TMA beam coalignment. The flat reference bar (RB) is used to align mirrors $\tilde{M}1$, $\tilde{M}2$ parallel to each other. This expands the 150 mm diameter aperture of the interferometer to the separation distance of 600 mm between TMA mirrors $M1$ and $M2/M3$. Interference of returning beams with the interferometer's reference beam, which is the beam reflected at the transmission flat (TF), are recorded with a CCD camera. The returning beams come from reflections at the left and right side of the reference bar, RB_L and RB_R , and from clockwise and counterclockwise propagation through the TMA, TMA_R and TMA_L . The paths of the beams traveling through the TMA are shown as dashed line for clockwise propagation and as dotted line for counterclockwise propagation. See also [53]. To watch an animation of the setup, scan the QR code in the upper left corner of the picture or go to www.gracefo.spacegravity.org/video6.

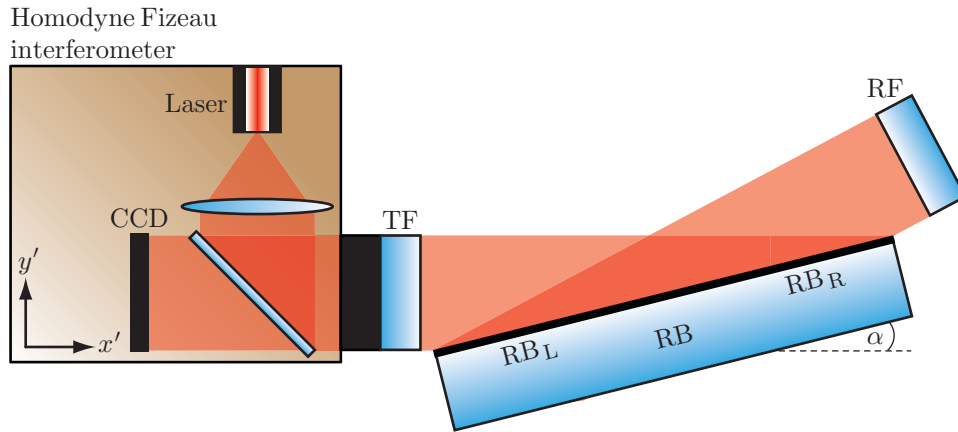


Figure 3.2: Setup to measure flatness of reference bar (RB) using the “Skip-Flat” test. The return flat (RF) topography has previously been measured and is subtracted.

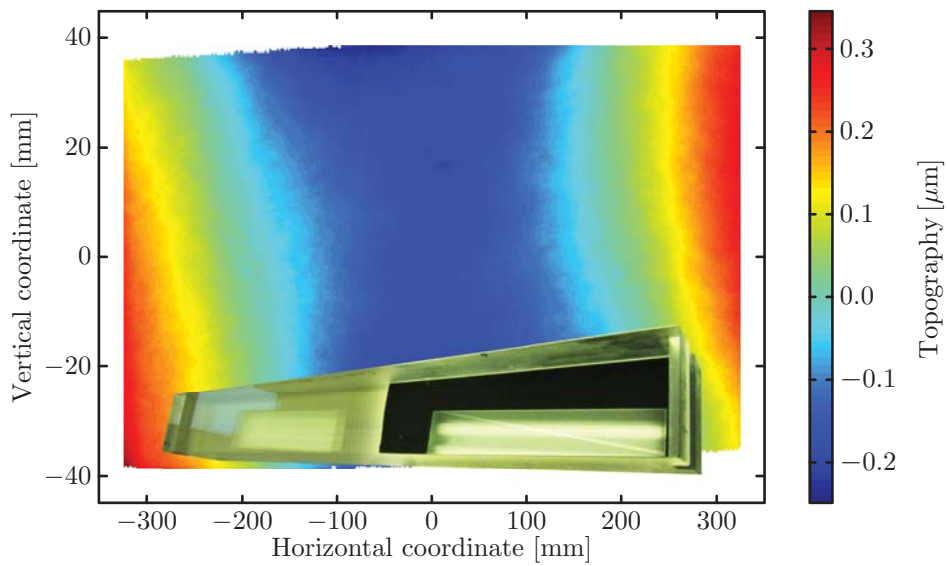


Figure 3.3: Topography of the reference bar (RB). A photograph of the RB is shown in the inset. The RB topography is concave with a peak-to-valley excursion of 600 nm. Angular distortions between left and right side of the RB of below $4 \mu\text{rad}$ can be inferred. See also [53].

Now we take a closer look at the different beam paths in Fig. 3.1. Mirror $\widetilde{M}1$ splits the laser beam of the homodyne phase-shifting interferometer into two parts. One part travels through the TMA counterclockwise, TMA_L , which is shown as dotted line. The other part is reflected by a second mirror $\widetilde{M}2$, which is parallel to $\widetilde{M}1$, and passes the TMA clockwise, TMA_R , see dashed line. The TMA is installed in a way such that interferograms of clockwise and counterclockwise propagating beams can be observed simultaneously on the CCD camera of the interferometer with interferograms of the reflections from both sides of the RB, RB_L and RB_R . The arrangement of TMA and RB in the setup can also be seen from the photograph in Fig. 3.4.

We introduce two coordinate systems in Fig. 3.1: the unprimed TMA-bound coordinate system (TCS), which is defined in Chap. 2.1.2, and the primed interferometer-bound coordinate system (ICS). The y' - and z' -axis of the ICS span the plane of the interferometer's CCD camera which records the interferograms. The y' -axis corresponds to the horizontal, the z' -axis to the vertical direction. The ICS x' -axis points along the laser beam axis of the outgoing interferometer beam.

Within alignment tolerances of a few mrad, the x -axis of the TMA-bound TCS is antiparallel to the ICS x' -axis. The TCS is rotated around the ICS x' -axis by the TMA tube angle ϕ_{tube} .

During the measurements, the TMA can be installed in two different ways to study the effect of gravity, which is expected to bend the tube and thus change the alignment of the TMA mirrors. The two different mounting types are illustrated in Fig. 3.5: “center-mounting” by the TMA bracket and “2-point support” of the tube on small steel rods close to the TMA mirror assemblies.

Additionally, the TMA can be installed with orientations $\phi_{\text{tube}} = 180^\circ, 0^\circ$. For the 2-point support, center loads can be installed at the TMA bracket. Simulations have shown that a 2-point support with a center load of 30 g and a tube angle of $\phi_{\text{tube}} = 180^\circ$ ($\phi_{\text{tube}} = 184^\circ$ was used for practical installation reasons) compensates for the tube-bending effect of gravity such that the test conditions come close to the zero-gravity environment during the actual satellite mission [50]. This mounting-type is therefore referred to as “zero-gravity” mounting.

3.1.2 Recovery of TMA beam coalignment information

We now discuss how we can extract the TMA beam coalignment information from the interferograms recorded with the phase-shifting homodyne interferometer in the setup shown in Fig. 3.1. Furthermore, we learn how to remove the main error sources: imperfect parallelism between mirrors $\widetilde{M}1$, $\widetilde{M}2$ and non-flatness of the RB.

Knowing the laser wavelength of the interferometer, $\lambda = 632.8 \text{ nm}$, the interfero-

3.1 TMA BEAM COALIGNMENT TEST BED

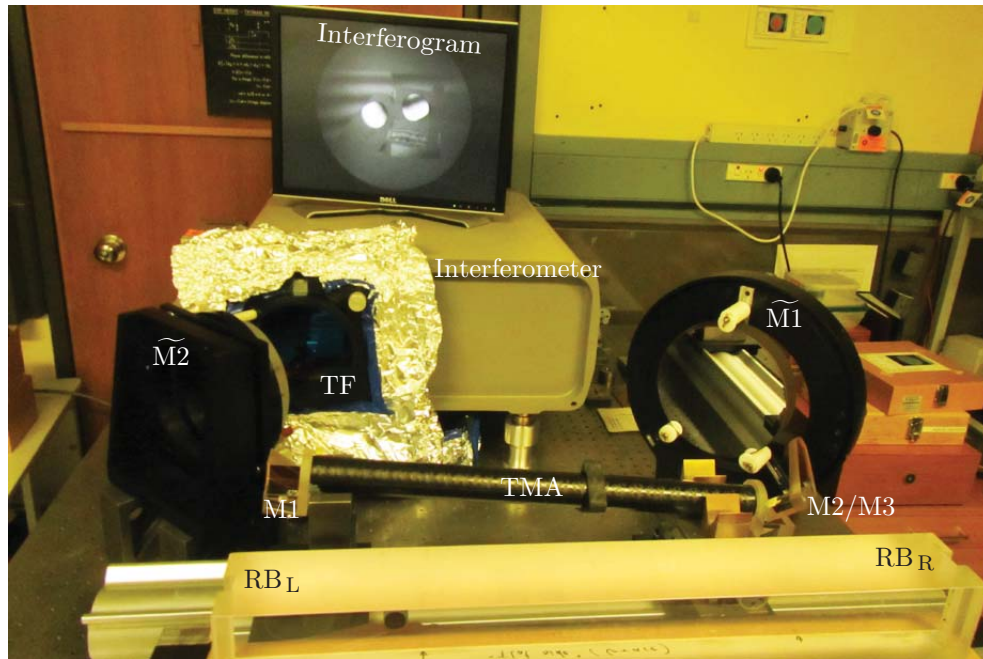
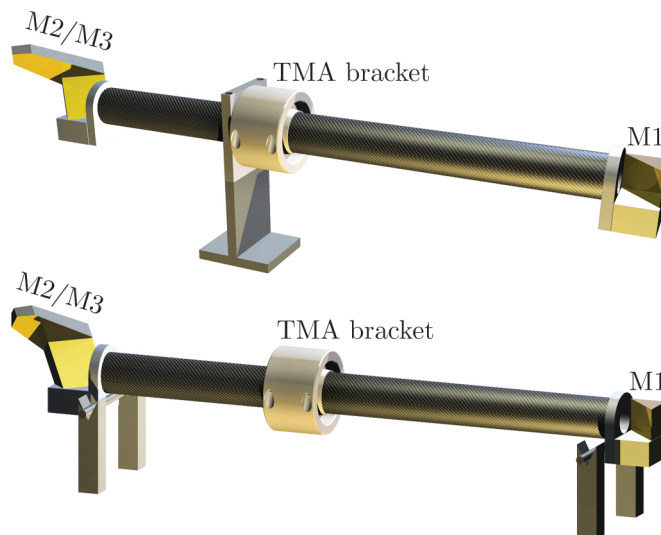


Figure 3.4: Photograph of setup to measure TMA beam coalignment. The CFRP TMA is installed in the setup. In the front, one can see the RB. The interferometer is located at the back. The interferometer beam exits through the transmission flat (TF).

Figure 3.5: The two pictures schematically illustrate the different mounting types of the CFRP TMA. Shown is the “center-mounting” by the TMA bracket (top) and the “2-point support” of the TMA tube on small steel rods close to the TMA mirror assemblies (bottom). For the 2-point support, center loads can be installed at the TMA bracket. In both pictures, the TMA tube angle is $\phi_{\text{tube}} = 180^\circ$.



grams are phase-calibrated in an automated manner by moving the interferometer's transmission flat (TF) by a well-defined distance. One measurement run of the interferometer is an average of 20 phase-shifting measurements. Each run gives a two-dimensional map in the y' - z' -plane with a phase value for each pixel of the CCD camera. We convert this map with the spatial scale of the CCD pixels given by the manufacturer, $y'_{\text{scale}} = 0.291$ [mm/pixel], $z'_{\text{scale}} = 0.339$ [mm/pixel], into pathlength variations over an area.

To facilitate explanations, Fig. 3.6 shows a typical interferogram as obtained with the TMA beam coalignment test bed. The pathlength variations map consists of four distinct sectors $K_i(y', z')$, $i = \text{RB}_L, \text{RB}_R, \text{TMA}_R, \text{TMA}_L$, which are sketched with dashed lines in Fig. 3.6. The four sectors result from laser beam reflections from the left and right side of the RB, RB_L and RB_R , and from laser beams propagating clockwise and counterclockwise through the TMA, TMA_R and TMA_L , cf. Fig. 3.1. Furthermore, we can identify the areas (a) and (b). They are caused by reflections from TMA mirrors M2/M3 and M1, respectively, which are beyond the TMA clear aperture and thus do not return to the interferometer. Area (c) shows a reflection from the mirror M1 mounting base.

For each sector $i = \text{RB}_L, \text{RB}_R, \text{TMA}_R, \text{TMA}_L$, we calculate partial derivatives along the y' - and the z' -axis:

$$\begin{aligned}\phi_{\text{hor},i}(y', z') &= -\arctan\left(\frac{\partial}{\partial y'} K_i(y', z')\right), \\ \phi_{\text{ver},i}(y', z') &= \arctan\left(\frac{\partial}{\partial z'} K_i(y', z')\right).\end{aligned}\tag{3.1}$$

By averaging over each sector i , we obtain

$$\begin{aligned}\varphi_{\text{hor},i} &= \overline{\phi_{\text{hor},i}}, \\ \varphi_{\text{ver},i} &= \overline{\phi_{\text{ver},i}}.\end{aligned}\tag{3.2}$$

The angles $\varphi_{\text{hor},i}$ and $\varphi_{\text{ver},i}$ correspond to ‘‘horizontal’’ and ‘‘vertical’’ tilts of the return beam of sector i with respect to the reference beam of the interferometer which is the beam reflected by the TF, cf. Fig. 3.1.

We refer to the horizontal and vertical TMA beam coalignment error in ICS coordinates for a counterclockwise propagating beam as δ_q^{ICS} , $q = \text{hor}, \text{ver}$. We calculate δ_q^{ICS} , $q = \text{hor}, \text{ver}$, from

$$\delta_q^{\text{ICS}} = 0.5 \cdot (\varphi_{q, \text{TMA}_L} - \varphi_{q, \text{TMA}_R}) - \varphi_{q, \text{M}}.\tag{3.3}$$

Here, $\varphi_{q, \text{M}}$ is the coalignment error of a counterclockwise propagating beam caused

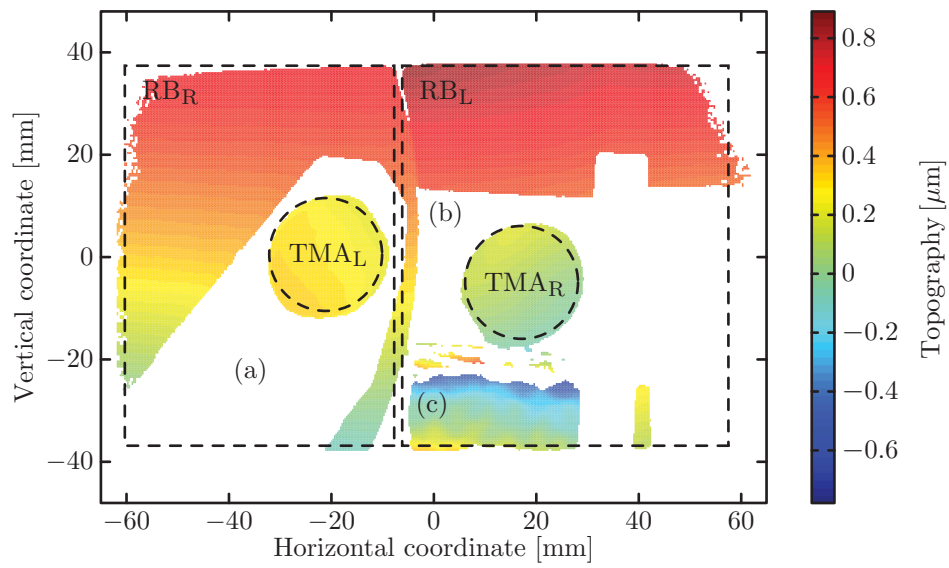


Figure 3.6: Typical interferogram as taken with the setup in Fig. 3.1, converted into pathlength variations over an area. The interferogram shows four sectors schematically drawn with dashed lines: RB_L , RB_R are caused by beam reflections from the left and right side of the RB, TMA_R , TMA_L by beams propagating clockwise and counterclockwise through the TMA. Areas (a), (b) are caused by beam reflections from mirror M2/M3 and M1 respectively, which are beyond the TMA clear aperture and thus do not return to the interferometer. Area (c) shows a reflection from the mirror M1 mounting base. See also [53].

by the two mirrors $\widetilde{M1}$, $\widetilde{M2}$, if they are not perfectly parallel. This effect can be calculated as

$$\varphi_{q,M} = 0.5 \cdot (\varphi_{q,RB_R} - \varphi_{q,RB_L}) + \varphi_{q,RB_{polish}}, \quad (3.4)$$

with $q = \text{hor, ver}$ and the polish angle difference $\varphi_{q,RB_{polish}}$ between the right and left side of the RB, which we obtain from the previously performed ‘‘Skip-Flat’’ test, cf. Sec. 3.1.1.

Equations (3.3) and (3.4) are deduced from simple geometrical considerations and have been verified in raytracing simulations performed with Matlab[®]. In the simulations, small angle approximations for rotations are applied ($\sin \phi \approx \phi$, $\cos \phi \approx 0$). Furthermore, the TMA is treated as a perfect retroreflector with a small beam coalignment error $\lesssim 50 \mu\text{rad}$ which is independent of the incident beam angle. As we have seen in Chap. 1.3.3.1, this is a valid simplification.

While the horizontal and vertical beam coalignment errors δ_q^{ICS} , $q = \text{hor, ver}$, are coordinate-dependent, the root-mean-square TMA beam coalignment error

$$\delta_{\text{RMS}} = \sqrt{\delta_{\text{hor}}^{\text{ICS}2} + \delta_{\text{ver}}^{\text{ICS}2}} \quad (3.5)$$

is independent of the coordinate system. However, the angle ϕ_{tube} by which the TCS is rotated around the ICS x' -axis is required if we want to transform δ_q^{ICS} from ICS to TCS coordinates.

From the CFRP TMA CAD model, we know the horizontal (600 mm) and vertical (48 mm) offset for a beam propagating through the CFRP TMA. From this, ϕ_{tube} can be determined by measuring the vertical offset between the centers of the TMA_R and TMA_L sectors in the interferograms, cf. Fig. 3.6. The alignment error of the ICS x' - and TCS x -axis is negligible. The TMA beam coalignment error δ_q^{TCS} , $q = \text{hor, ver}$, in TCS coordinates can then be calculated with a coordinate transformation of δ_q^{ICS} from ICS to TCS coordinates.

3.1.3 Data evaluation tool

A data evaluation tool written in Matlab[®] has been developed in this thesis with which the interferograms from the TMA beam coalignment measurements can be processed. The evaluation tool reads in the RB topography and the TMA interferograms. It then extracts the TMA beam coalignment as described in Sec. 3.1.2.

The evaluation tool has been extensively tested with a raytracing-based data simulator, which had been developed in Matlab[®]. The data simulator creates simulated RB topographies and TMA interferograms which can be processed with the evaluation tool. By comparing simulation input parameters with values recovered with the

3.1 TMA BEAM COALIGNMENT TEST BED

Table 3.1: *Simulation input parameters and parameter values recovered with the evaluation tool. All values given in μrad , except for ϕ_{tube} , which is given in degrees.*

Parameter name	Input value	Output value	Unit
$\delta_{\text{hor}}^{\text{TMA}}$	-2.14	-2.14	μrad
$\delta_{\text{ver}}^{\text{TMA}}$	25.74	25.69	μrad
$\varphi_{\text{hor, RBpolishR}}$	-6.98	-6.98	μrad
$\varphi_{\text{ver, RBpolishR}}$	-6.62	-6.59	μrad
$\varphi_{\text{hor, RBpolishL}}$	-8.74	-8.74	μrad
$\varphi_{\text{ver, RBpolishL}}$	2.57	2.55	μrad
$\varphi_{\text{hor, M}}$	5.86	5.86	μrad
$\varphi_{\text{ver, M}}$	-3.42	-3.37	μrad
ϕ_{tube}	2.97	2.96	$^{\circ}$

evaluation tool, the evaluation tool and the achievable accuracies have been investigated.

As an example, Tab. 3.1 shows a list of simulation input parameters and output parameters recovered with the evaluation tool. The corresponding simulated RB topography is shown in Fig. 3.7, whereas the simulated TMA beam coalignment measurement interferogram is displayed in Fig. 3.8. In total, more than 40 such simulation runs with randomly selected input parameters have been performed. The tube angle ϕ_{tube} was varied by $\pm 7^{\circ}$, the TMA beam coalignment errors δ_q^{TCS} , $q = \text{hor, ver}$ by $\pm 50 \mu\text{rad}$ each, and all other parameters by as much as $\pm 100 \mu\text{rad}$. Also extreme scenarios with small TMA beam coalignment error $\delta_q^{\text{TCS}} \leq 1 \mu\text{rad}$ and large values for all other parameters of $\pm 100 \mu\text{rad}$ were studied. For all cases, the tube angle ϕ_{tube} could be recovered within $\pm 0.1^{\circ}$, all other parameters including the TMA beam coalignment error δ_q^{TCS} , $q = \text{hor, ver}$, within less than $\pm 1 \mu\text{rad}$.

During the evaluation process, suitable areas within the measurement sectors (cf. Fig. 3.6) are chosen manually to determine the angles $\varphi_{\text{hor, } i}$, $\varphi_{\text{ver, } i}$, $i = \text{RB}_L, \text{RB}_R, \text{TMA}_R, \text{TMA}_L$. For the simulations, this has no influence, since the simulated areas are homogeneous and show no features other than horizontal and vertical tilt. However, for the evaluation of measured interferograms, this might have some arbitrary influence on the final result, so that in Chap. 4.1, each measurement is evaluated 10 times selecting slightly different areas each time.

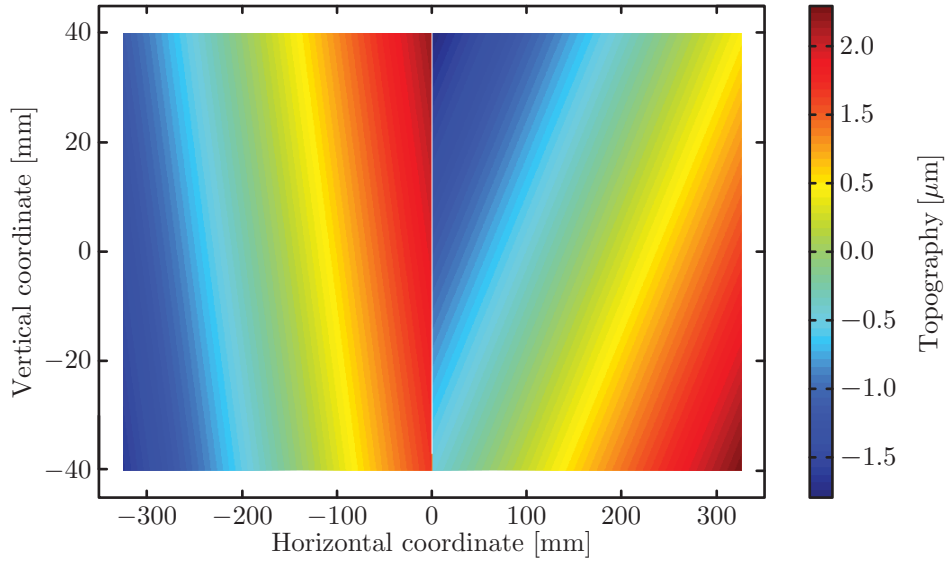


Figure 3.7: *Topography of simulated RB. The RB topography is approximated by two areas with horizontal and vertical tilt.*

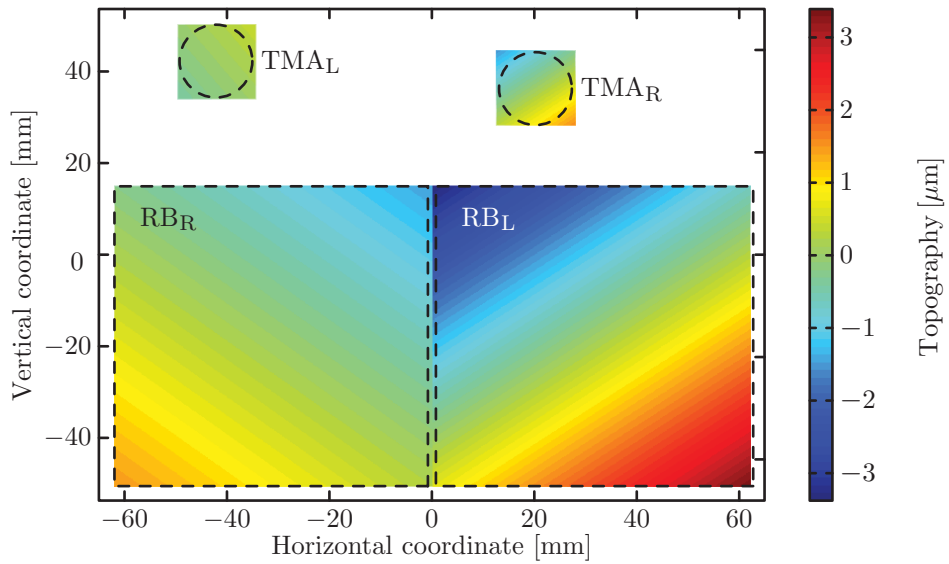


Figure 3.8: *Simulated interferogram of TMA coalignment measurement, cf. Fig. 3.6. Note that RB_L , RB_R look different from the RB topography in Fig. 3.7 due to the simulation of installation angle tolerances in the setup and the effect of mirrors M1, M2.*

3.2 TMA rotation-to-pathlength coupling test bed

Besides beam collimation, the other important property of the TMA that is essential for the performance of the LRI is its behavior under rotation, since it is the cause of one of the limiting noise sources of the LRI (cf. Sec. 1.2).

We have seen in Chap. 1.3 that a perfect TMA which is rotated around its vertex does not cause pathlength changes in the LRI roundtrip measurement. Furthermore, we have learned that for a real TMA with non-zero mirror misalignments, a point of minimal rotation-to-pathlength coupling (PMC) can be defined. The residual rotation-to-pathlength coupling can be minimized by rotating around the PMC.

During spacecraft integration, however, the TMA vertex instead of the PMC will be placed at the S/C center of rotation for practical reasons, since the TMA vertex can be directly measured by probing the TMA mirror planes with a coordinate measuring machine (CMM, [101]).

The purpose of the TMA rotation-to-pathlength coupling test bed is threefold:

1. We want to show that for a “realistic” TMA with non-zero mirror misalignments rotation-to-pathlength coupling can be sufficiently well reduced by rotating around the TMA PMC. We aim at residual couplings of $20\ \mu\text{m}/\text{rad}$.
2. We want to verify that TMA PMC and TMA vertex are colocated within $\pm 100\ \mu\text{m}$ so that the baseline integration procedure of the TMA into the spacecraft does not significantly increase the rotation-to-pathlength coupling.
3. We want to verify the analytical model of TMA properties as presented in Chap. 1.3 against measurements.

The TMA vertex is determined by probing the TMA mirror planes with a CMM. In contrast, for a direct measurement, the TMA PMC has to be determined dynamically: The TMA is placed on a hexapod, a six-degree-of-freedom rotation and translation platform, and range displacements incurred under calibrated hexapod rotations are monitored with heterodyne interferometry. By varying the rotation pivot of the hexapod and searching for the point for which the coupling is minimal, the PMC can be determined within the hexapod coordinate frame.

However, there are two major challenges that had to be resolved: Firstly, the hexapod coordinate frame is not directly measurable with the CMM, which makes it impossible to directly compare the TMA PMC position obtained within the hexapod coordinate frame with the TMA vertex position, which is measured in CMM coordinates. Secondly, the hexapod’s translational precision is limited to $\pm 500\ \text{nm}$. This introduces noise to the range displacement measurement which limits the PMC

location to $\pm 200\ \mu\text{m}$.

There are different approaches to overcome those two challenges. One of the attempts was to build a six-degree-of-freedom reference interferometer to monitor erroneous hexapod motions. While this endeavor has evolved into an interesting project on its own right (cf. App. A), it did not provide an immediate solution due to its complexity.

As so often, a much simpler, yet very elegant solution was at hand: A second, much smaller retroreflector is iteratively positioned at the TMA PMC. The second retroreflector serves as a physical reference of the TMA PMC and is mounted on the same platform as the TMA. This is accomplished by choosing for the second retroreflector a ball-mounted retroreflector (BMR), the vertex of which is located at the center of a spherical housing, which is accessible to CMM measurements.

In the alignment process, differential range displacements between TMA and BMR under hexapod rotations are monitored, in which erroneous hexapod translations cancel out. These differential measurements are minimal when the BMR is properly positioned at the TMA PMC. Consecutively, the BMR housing is measured with the CMM, so that the position of the TMA PMC can be determined in CMM coordinates and compared to the CMM-derived TMA vertex position.

The TMA rotation-to-pathlength coupling test bed consists of two disjunct setups which are introduced in the following sections: The *PMC test bed* comprises the hexapod and is dedicated to aligning the BMR to the TMA PMC (Sec. 3.2). In the *CMM test bed*, TMA mirror planes and BMR position are measured with the CMM to compare TMA vertex and PMC positions (Sec. 3.2.2). As we will see, this setup is a very powerful TMA investigation tool, since it even provides the possibility to measure TMA beam coalignment.

Furthermore, Sec. 3.2.3 provides an assessment of the measurement uncertainty of TMA vertex and PMC comparison that is to be expected with the presented method. The setups and procedures of the TMA rotation-to-pathlength coupling test bed that have been developed within this thesis have also been published [54, 102].

3.2.1 PMC test bed: locating the TMA PMC

The PMC test bed to locate the TMA PMC is shown in Fig. 3.9. The TMA and the BMR (PLX Inc., BMR-1.5-1) are mounted on a carbon fiber breadboard (CarbonVision GmbH, customized, $700 \times 400 \times 50\ \text{mm}^3$), which is installed on a hexapod (PI GmbH & Co. KG, M824). The BMR vertex is located within $2.5\ \mu\text{m}$ in the center of the $38.1\ \text{mm}$ diameter spherical housing according to the manufacturer's specification.

3.2 TMA ROTATION-TO-PATHLENGTH COUPLING TEST BED

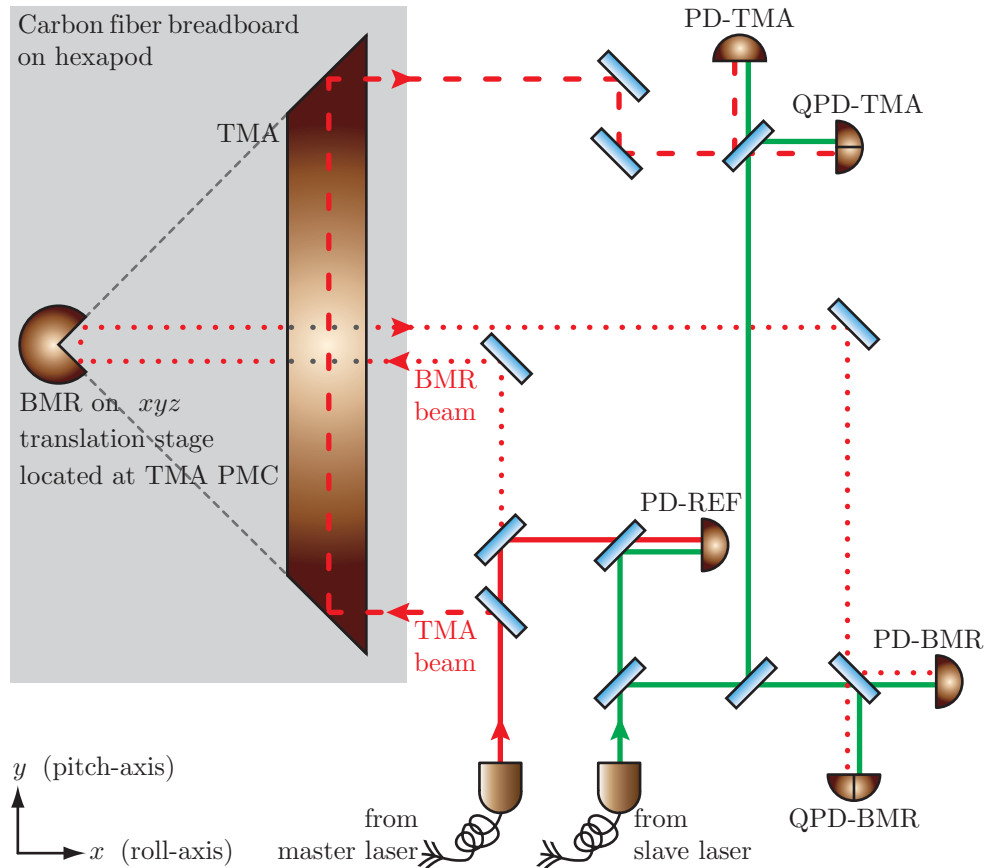


Figure 3.9: Setup to locate the TMA PMC. Range displacements to TMA and BMR incurred under hexapod rotations are monitored with heterodyne interferometry on PD-TMA and PD-BMR, with the measurement on PD-REF being subtracted as reference. Beamwalk of TMA beam (dashed line) and BMR beam (dotted line) can be observed on QPD-TMA and QPD-BMR, respectively. The slave laser is offset phase-locked to the master laser before entering the setup. See also [54].

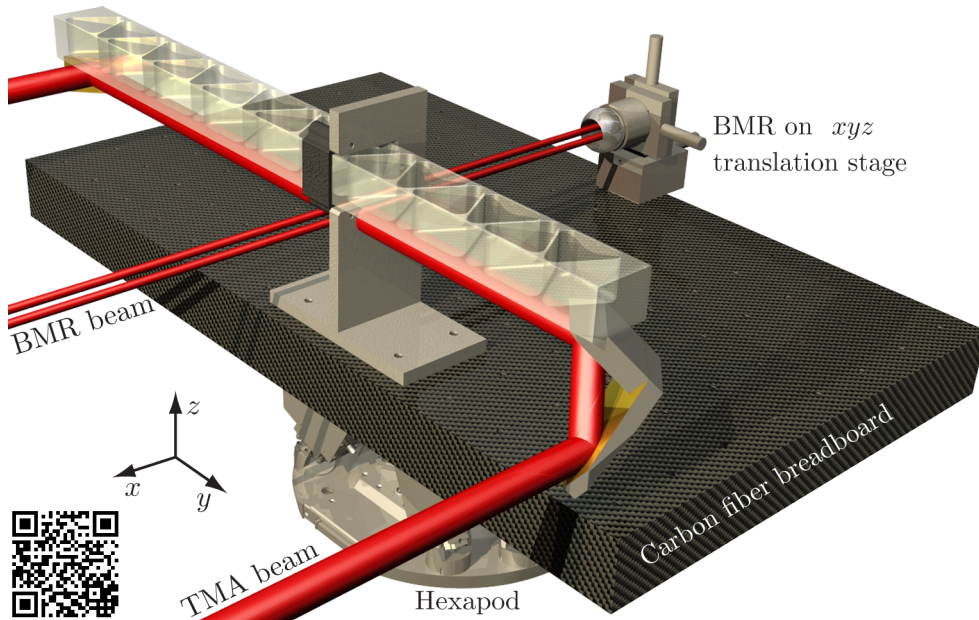


Figure 3.10: CAD model of Glass TMA in PMC test bed. The laser beams probing the TMA and the BMR are shown in red. Both beams are fed in along the $-x$ -axis (cf. Fig. 3.9). Glass TMA CAD file provided by ANU, hexapod CAD file by PI GmbH & Co. KG. An animation of this setup can be found by scanning the QR code in the lower left corner of the picture or by going to www.gracefo.spacegravity.org/video7.

The hexapod exhibits a positional uncertainty of ± 500 nm, which has been verified interferometrically along the x -axis. For pitch and yaw, the rotational uncertainty of the hexapod has been shown to be below ± 6 μ rad with an autocollimator (ELCOMAT direct SN-162, Möller Wedel), which has a calibrated angular accuracy of ± 0.34 μ rad).

The setup in Fig. 3.9 has been implemented for test runs with the Glass TMA, the TMA DM, and the TMA QM (cf. Chap. 2.1). The CAD drawings and photographs for the Glass TMA implementation are displayed in Figs. 3.10 and 3.11. Likewise, the implementation for the TMA DM, which looks identical for the QM, can be seen in Figs. 3.12 and 3.13. The coordinate axes given are hexapod coordinates. Nominally, these axes are coaligned with the TMA coordinate axes as defined in Chap. 2.1.2. Alignment tolerances in the setup are a few mrad.

The laser beams in the setup in Fig. 3.9 are generated by two lasers (Mephisto 500, Innolight GmbH, now Coherent Inc.) with 1064 nm wavelength, which are off-set phase-locked at 6 MHz with an analog phase lock (not shown in the picture) and

3.2 TMA ROTATION-TO-PATHLENGTH COUPLING TEST BED

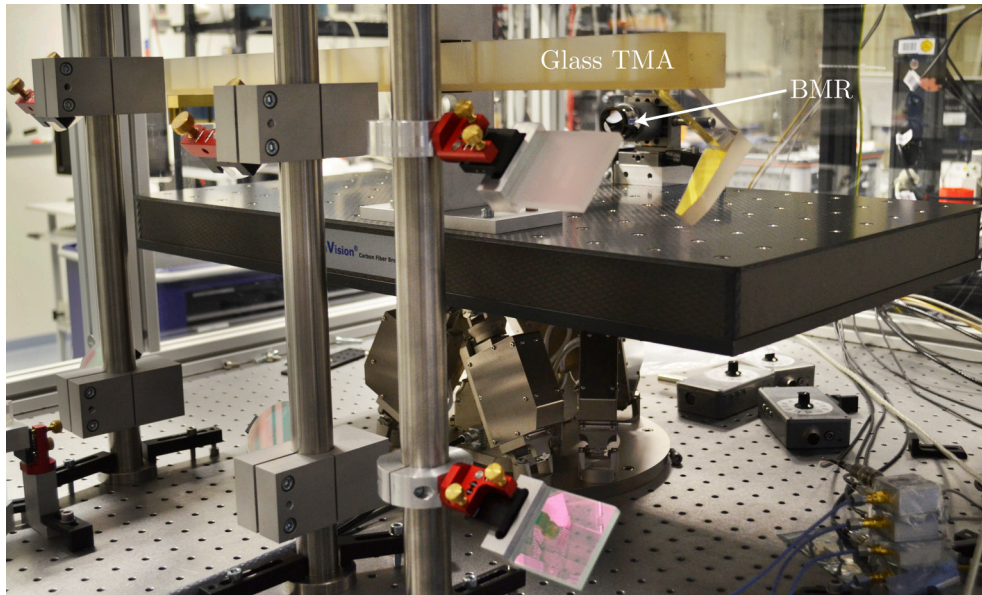


Figure 3.11: Photograph of Glass TMA in PMC test bed. The laser beams are routed with periscopes.

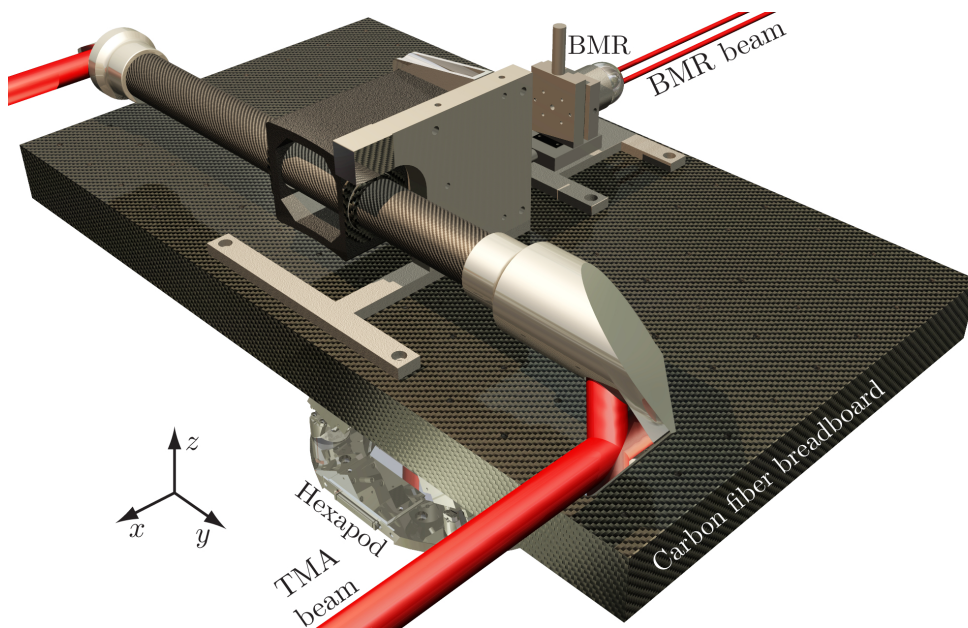


Figure 3.12: CAD model of TMA DM in PMC test bed. The laser beams probing the TMA and the BMR are shown in red. The TMA beam is fed in along the $-x$ -axis (cf. Fig. 3.9), while the BMR beam, due to space constraints, enters along $+x$. TMA DM CAD file provided by STI, hexapod CAD file by PI GmbH & Co. KG.

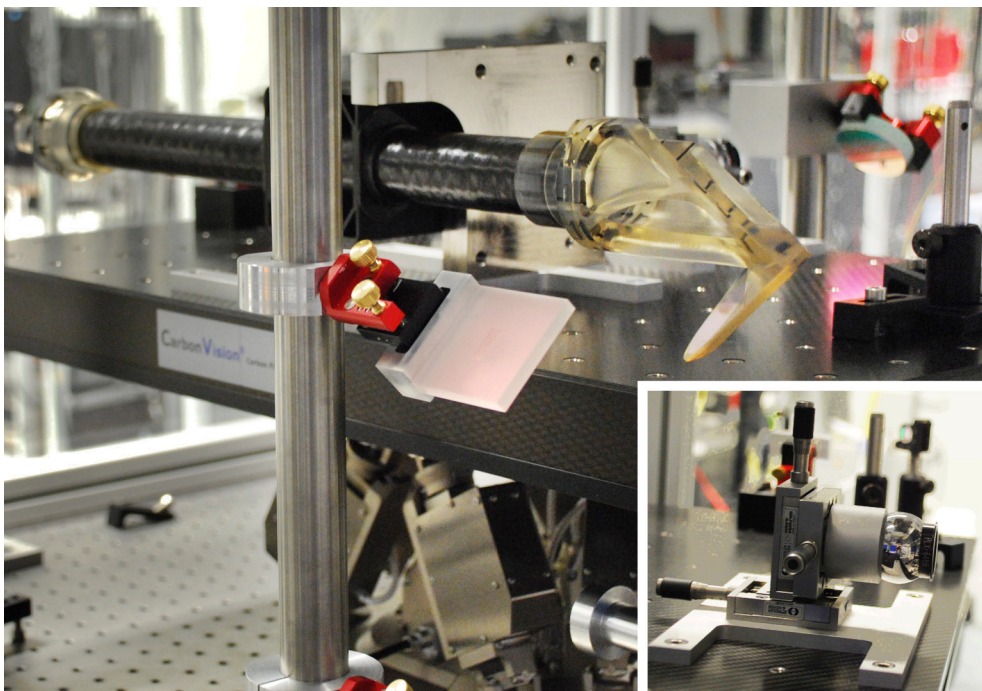


Figure 3.13: Photograph of TMA DM in PMC test bed. The inset shows the BMR on a 3-dimensional translation stage with which the BMR is placed at the TMA PMC.

delivered to the setup via optical fibers. The laser beam coming from the slave laser serves as reference beam for the interferometric range measurements. The laser beam from the master laser is split and coupled into both TMA and BMR.

For the Glass TMA, as shown in Figs. 3.9 and 3.10, both TMA beam and BMR beam enter along $-x$. For the TMA DM and the TMA QM, cf. Fig. 3.12, the BMR beam probes the BMR from the opposite direction along $+x$ due to space constraints.

The beams retroreflected by TMA and BMR are interfered with the reference beam on AC-coupled photodiodes PD-TMA and PD-BMR, respectively. Furthermore, by using differential power sensing (DPS, cf. Chap. 1.4.4), beamwalk of the retroreflected beams can be observed on the position-sensitive DC-coupled quadrant photodiodes QPD-TMA, QPD-BMR, with the reference beam being blocked.

For the Glass TMA, the measurement beam probing the TMA is coarsely aligned to the hexapod x -axis by translating the hexapod along this axis and simultaneously observing beamwalk on QPD-TMA. By minimizing the beamwalk, an alignment with an uncertainty of some mrad is achieved, which is limited by systematic errors in the hexapod motion.

For the TMA DM and the TMA QM, the TMA beam is aligned to the nominal TMA incident beam axis, which is parallel to the TMA x -axis and centered on TMA mirror M1 (cf. Chap. 2.1.2). As mentioned before, alignment tolerances between hexapod coordinate axes and TMA coordinate axes of some mrad are expected. The nominal TMA incident beam axis is referenced with two position-sensitive QPDs installed on the carbon fiber breadboard, as will be explained in Sec. 3.2.2.

The relative alignment of TMA and BMR beam is also accomplished by moving the hexapod along the x -axis. However, this time, beamwalk *differences* between QPD-TMA and QPD-BMR are minimized (cf. Fig. 3.9). By this, erroneous hexapod motion cancels out since it leads to common beamwalk on both QPDs, so that a much better coalignment between the TMA beam and the BMR beam of $\pm 200 \mu\text{rad}$ is achieved. Since for the beamwalk differences, the relative alignment of the axes of QPD-TMA and QPD-BMR matters, they have been aligned within $\pm 2^\circ$.

In a next step, the TMA PMC is coarsely located in hexapod coordinates. For the x -coordinate, PMC^x , this is achieved by performing hexapod pitch and yaw rotations around pivot points PP with varying x -value PP^x and observing beamwalk on QPD-TMA, cf. Fig. 3.9. This method yields a 1 mm uncertainty in PMC^x . This is sufficient, since the rotation-to-pathlength coupling for PMC-to-vertex offsets along the x -axis is expected to be three orders of magnitude smaller than for offsets along the y - and z -axes (cf. Chap. 1.3.2).

The remaining TMA PMC coordinates, PMC^y and PMC^z , are determined in a similar way: While the hexapod performs calibrated yaw and pitch rotations, this

time with varying PP^y and PP^z , the corresponding range displacement is observed with heterodyne interferometry on PD-TMA. This allows for a coarse PMC determination of $\pm 200 \mu\text{m}$ within the hexapod coordinate frame.

After TMA PMC determination in hexapod coordinates, the BMR is coarsely located to this TMA PMC position with a comparable procedure in all three axes BMR^x , BMR^y , BMR^z . Now the test bed is prepared to refine the *relative* alignment of BMR and TMA PMC and consecutively to measure the minimal achievable rotation-to-pathlength coupling.

In the following, the hexapod always rotates around the TMA PMC, which has previously been determined in hexapod coordinates. While this is in principle not necessary, it reduces beamwalk during rotations, which is one candidate for residual noise in the setup.

In the next step, we consider range displacement *differences* between PD-TMA and PD-BMR, cf. Fig. 3.9. In these differences, any erroneous hexapod translation along the measurement beam axis cancels out, since it is common for both measurements on PD-TMA and PD-BMR.

Recalling the linear rotation-to-pathlength coupling for a TMA with an offset from the center of rotation, cf. Eq. (1.1), we can write for the displacement measurements δL^{TMA} and δL^{BMR} to TMA and BMR, respectively:

$$\begin{aligned}\delta L^{\text{TMA}} &= -(\text{PMC}^z - \text{PP}^z) \delta\theta_{\text{pitch}} + (\text{PMC}^y - \text{PP}^y) \delta\theta_{\text{yaw}} + \delta x^{\text{HX}}, \\ \delta L^{\text{BMR}} &= -(\text{BMR}^z - \text{PP}^z) \delta\theta_{\text{pitch}} + (\text{BMR}^y - \text{PP}^y) \delta\theta_{\text{yaw}} + \delta x^{\text{HX}},\end{aligned}\tag{3.6}$$

where δx^{HX} has been added to account for erroneous hexapod translations along the measurement beam axis. The coupling of offsets along the x -axis has been neglected here. This formula is valid under the assumption that TMA beam and BMR beam are parallel.

By taking the difference of both measurements in Eq. (3.6), we obtain the relative range displacement between TMA and BMR:

$$\delta L_{\text{rel}} = \delta L^{\text{TMA}} - \delta L^{\text{BMR}} = -(\text{PMC}^z - \text{BMR}^z) \delta\theta_{\text{pitch}} + (\text{PMC}^y - \text{BMR}^y) \delta\theta_{\text{yaw}}.\tag{3.7}$$

This result is astonishingly simple and has very interesting implications. Note that the erroneous hexapod motion δx^{HX} has canceled out. Furthermore, the hexapod rotation pivot point PP does not appear at all in this formula. This means that once the TMA PMC and the BMR have been colocated, this measurement gives the same result as rotating around the TMA PMC, independent of the actual hexapod pivot point. This is a very nice feature of this measurement configuration, since we

have no means of measuring deviations of hexapod rotations from its nominal pivot point.

To verify Eq. (3.7), the BMR was translated in y - and z -direction in steps of $100\ \mu\text{m}$ while measuring the differential rotation-to-pathlength coupling δL_{rel} for yaw and pitch, respectively. The slope was close to $1\ \text{m/rad}$, as expected from Eq. (3.7): $-0.993\ \text{m/rad}$ in y - and $1.003\ \text{m/rad}$ in z -direction, which is compatible with an alignment tolerance of the BMR translation stage with respect to the measurement beam axis of a few mrad.

By iteratively translating the BMR and measuring the relative displacement δL_{rel} under hexapod rotations $\delta\theta_{\text{pitch}}$ and $\delta\theta_{\text{yaw}}$, the rotation-to-pathlength coupling can be minimized. On the one hand, this yields an upper limit estimation for the minimal achievable rotation-to-pathlength coupling. On the other hand, this simultaneously fine-aligns the BMR to the TMA PMC location.

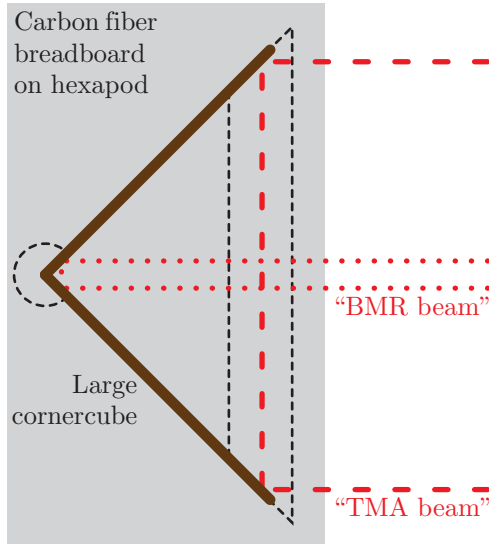
The differential measurement concept of Eq. (3.7) was tested by replacing TMA and BMR in Fig. 3.9 with a large hollow cornercube retroreflector (PLX Inc., 130 mm diameter clear aperture), as is illustrated in Fig. 3.14. Since now both “TMA beam” and “BMR beam” probe the same cornercube, the difference between both measurements should nominally be zero. However, while hexapod systematic errors are effectively suppressed in this configuration, they might still couple via misalignment of TMA beam and BMR beam, which is of the order of $\pm 200\ \mu\text{rad}$. For the PMC test bed, a typical noise floor for the relative displacement measurements δL_{rel} of $\pm 5\ \mu\text{m/rad}$ was found, which limits BMR and TMA PMC colocation to $\pm 5\ \mu\text{m}$.

A caveat of the differential measurement concept as described by Eq. (3.7) is that we always see the combined effect of TMA and BMR which cannot be disentangled in this configuration. However, effects of an imperfect BMR such as a non-vanishing difference between BMR vertex and BMR PMC scale with the BMR size (cf. Chap. 1.3.3.2, [65, 66]), which is a factor of more than 30 smaller than the TMA.

3.2.2 CMM test bed

The CMM test bed, as second part of the TMA rotation-to-pathlength coupling test bed, consists of a CMM facility (Global Advantage, GLOA 000670, probe head: Tesa-Star m, 3P005901, Hexagon Metrology GmbH). The CMM positional accuracy in calibrated contact mode has been shown to be better than $\pm 2\ \mu\text{m}$ over the whole measurement volume during a manufacturer’s calibration. With the CMM, location and orientation of the TMA mirror planes and the location of the BMR sphere can be measured in a mechanical reference frame. The CMM test bed serves three purposes:

Figure 3.14: Setup to determine the noise floor in the differential range measurement δL_{rel} for TMA PMC location. TMA and BMR in Fig. 3.9 have been replaced by a single large cornercube retroreflector which is simultaneously probed with both “TMA beam” and “BMR beam”.



1. Pre-alignment: Before installation of the carbon fiber breadboard hosting TMA and BMR into the PMC test bed (Sec. 3.2.1), the BMR can be pre-positioned to the TMA vertex using the CMM. Furthermore, a nominal beam axis for the measurements in the PMC test bed can be defined. For the Glass TMA test campaign, which was the first to be performed, the pre-alignment step was not yet included in the test procedure.
2. TMA vertex vs. PMC: After positioning the BMR at the TMA PMC in the PMC test bed, TMA vertex and BMR position are measured with the CMM.
3. TMA dihedral angles and beam coalignment: Measurement of TMA dihedral angles and TMA beam coalignment to compare experimental results with results obtained from the analytical TMA model (cf. Chap. 1.3).

Most of the above-mentioned tasks can be performed by positional measurements of the TMA mirrors and the BMR sphere with the CMM. However, to define a laser beam axis or to measure TMA beam coalignment with the CMM, a special method is required which has been developed for this purpose. The name of this special method is CMM-assisted beam alignment and measurement (CABAM, [102]). For stringency, let us first continue explaining the CMM test bed. Subsequently, CABAM is introduced in Sec. 3.2.2.4.

In Figs. 3.15 and 3.16, we can see the installation of the Glass TMA and the TMA DM on the CMM table. The TMA units are mounted on the carbon fiber breadboard. Any CMM measurement begins with the definition of a suitable coordinate system.

3.2 TMA ROTATION-TO-PATHLENGTH COUPLING TEST BED

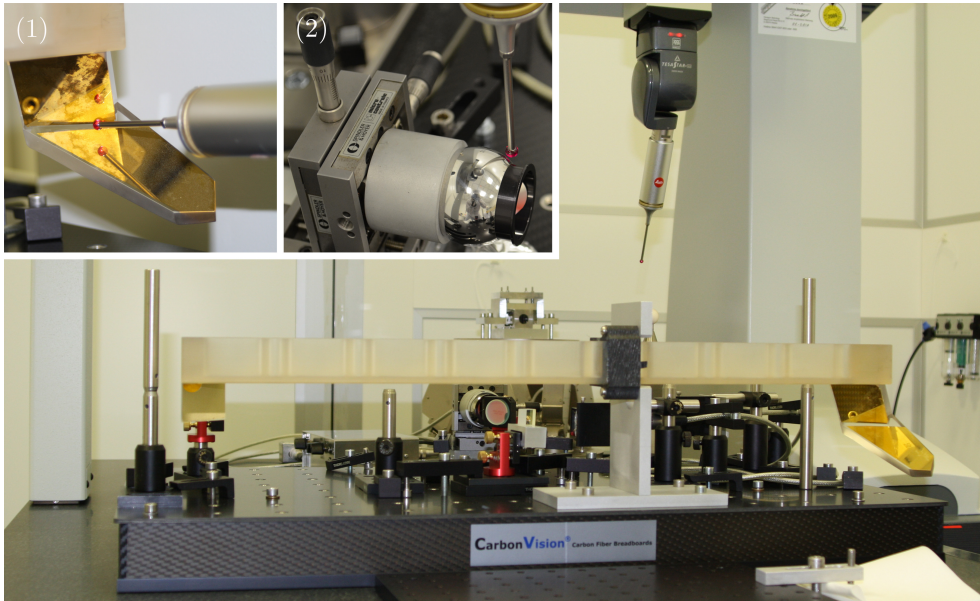


Figure 3.15: *CMM measurement of Glass TMA vertex and position of BMR. The insets show (1) probing of TMA mirror M3 and (2) probing of BMR sphere with the CMM head.*

As explained in Chap. 2.1.2, for the Glass TMA, the faces of the glass ceramic bar define the coordinate system, while TMA DM and TMA QM have dedicated reference cubes. At the beginning of the CMM measurement, a script is generated by manually probing each point position that is to be measured. For the actual measurement run, this script is then executed in automated CNC (computerized numerical control) mode.

In our case, each measurement run probes the three planes that define the coordinate system of the respective TMA unit, cf. Chap. 2.1.2, the planes of the three TMA mirrors, and the BMR sphere. As can be seen in inset (1) of Fig. 3.15 and in the inset of Fig. 3.16, probing the TMA mirrors is a tricky task that requires a lot of attention. The path of the CMM probe head has to be checked carefully before the automated CNC mode is activated, since any design or execution error in the CMM movement could damage the mirror coating or the sensitive glass pieces. Furthermore, the CMM probe shaft orientation has to be adapted to the probe object. While for the TMA mirrors a horizontal orientation is suitable as in Fig. 3.15, inset (1), a vertical orientation is necessary to probe the BMR sphere, see inset (2).

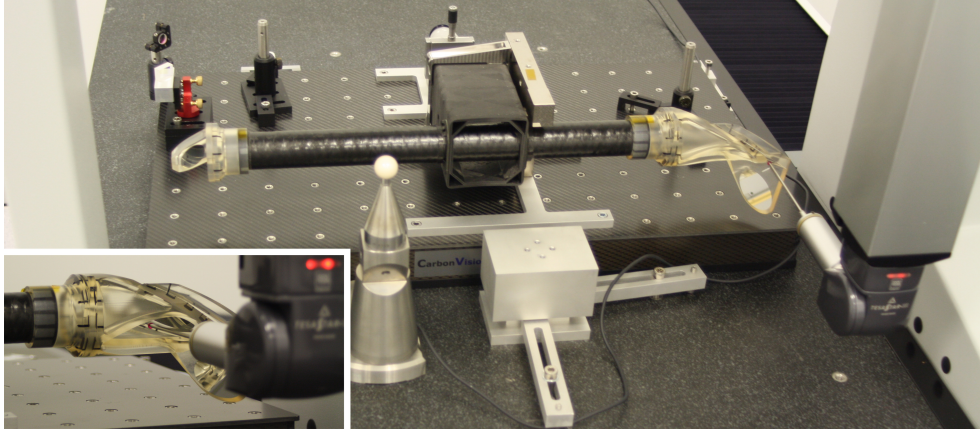


Figure 3.16: CMM measurement of TMA DM vertex and position of BMR. The inset shows probing of TMA mirror M2 with the CMM head, which was a delicate task due to the encapsulation of the M2/M3 mirror subassembly.

3.2.2.1 Pre-alignment in CMM

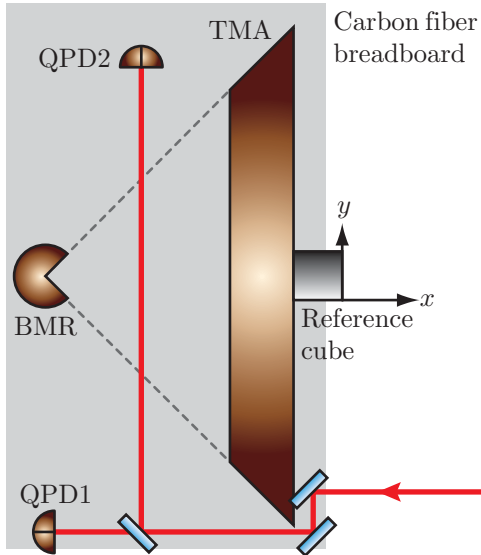
For the “pre-alignment” step, TMA mirrors and BMR are probed iteratively, while the center of the BMR sphere is translated to coincide with the TMA vertex, which is determined as the intersection point of the TMA mirror planes. Colocation of BMR and TMA vertex of $\pm 35 \mu\text{m}$ in all three axes is easily achieved. Furthermore, an auxiliary laser beam is aligned to the nominal TMA incident beam direction and position as referenced to the reference cube (cf. Chap. 2.1.2).

For aligning and measuring the beam axis, CABAM is used iteratively. The auxiliary laser beam bypasses the TMA on two mirrors, see Fig. 3.17. Subsequently, two position-sensitive QPDs, which are installed on the carbon fiber breadboard, are centered in the beam. By this, the nominal TMA incident beam axis is referenced with the two QPDs and can be reconstructed with the measurement beam in the PMC test bed, cf. Sec. 3.2.1, by again centering the beam on the QPDs. With a lever between QPD1 and QPD2 (see Fig. 3.17) of 0.5 m and a DPS centering accuracy of typically below $\pm 10 \mu\text{m}$, the auxiliary beam can be both referenced and reconstructed with a positional accuracy of $\pm 10 \mu\text{m}$ and an angular accuracy of $\pm 40 \mu\text{rad}$.

3.2.2.2 TMA vertex vs. PMC

After aligning the BMR to the TMA PMC in the PMC test bed (Sec. 3.2.1), the “TMA vertex vs. PMC” measurement is performed with the CMM. Just as for the pre-alignment step, TMA mirror planes and BMR sphere are probed. However, now the BMR is located at the TMA PMC, so that from this measurement, a difference

Figure 3.17: An auxiliary laser beam is aligned to the nominal TMA incident beam axis as referenced to the reference cube using CABAM. The auxiliary beam bypasses the TMA on two mirrors. Two position-sensitive QPDs, which are installed on the carbon fiber breadboard, are centered in the beam to reference both beam position and direction.



between TMA vertex and TMA PMC can be inferred.

3.2.2.3 TMA dihedral angles and beam coalignment measurement with CMM

After comparing TMA vertex and PMC position in the previous step, the measurement of “TMA dihedral angles and beam coalignment” is performed. While this is not the main objective of this test bed, it is a unique opportunity to test the predictions of the analytical TMA model, cf. Chap. 1.3. Note that the TMA coalignment results obtained in this setup are not representative for the TMA performance, since this test bed does not support a gravity-compensating mount for the TMAs (cf. Sec. 3.1).

On the one hand, TMA dihedral angles are obtained from the TMA mirror planes, which have already been measured in the previous “TMA vertex vs. PMC” step. On the other hand, TMA beam coalignment is measured. This is done by launching a beam into the TMA and measuring both incident beam axis and the beam axis of the retroreflected beam with CABAM. The difference between the axes of the incident and the retroreflected beam reveals the TMA beam coalignment.

3.2.2.4 CMM-assisted beam measurement and alignment

After using CABAM so extensively in the previous steps, let us now explain how CABAM actually works. CABAM is a novel tool to both measure laser beam direction and position and to align a laser beam to a desired direction and position within the

CMM mechanical coordinate system.¹ A detailed presentation of CABAM has also been published [102].

The alignment and measurement of a laser beam axis within a mechanical frame are known challenges especially in science fields involving space-born interferometers [5,8,9,14,15,103–105]. Interferometers for space applications are often assembled with a CMM, which is used to control position and orientation of the optical components. However, the alignment of the laser beams that are routed through the assembly is a much more demanding task since the beams cannot be physically contacted. To this end, a tool has been developed known as calibrated quadrant photodiode pair (CQP, [73]).

The CQP comprises two position-sensitive quadrant photodiodes (QPDs) installed in a mechanically stable housing. It is calibrated in a way that an incoming beam which is centered on both QPDs has a known offset and direction with respect to the housing.

In the CMM test bed (Sec. 3.2.2), first attempts to measure and align a laser beam axis with the CMM were performed using an AEI in-house built CQP [106]. However, some difficulties arose:

- The CQP calibration process is prone to inaccuracies due to instability of the CQP housing. During the calibration, the surface of the housing is probed with the CMM, while the housing is mounted under different orientations. When analyzing the CMM measurements, a non-negligible effect of housing distortions was observed when changing CQP orientations. Furthermore, for the purposes of the CMM test bed (Sec. 3.2.2) it is necessary to move the CQP to different locations and install it on different heights to account for the lateral and vertical TMA beam offsets. Any such manipulation of the CQP housing might invalidate the calibration.
- The achievable CQP angular accuracy depends on the lever arm between the two QPDs, which is about 15 cm for this specific CQP leading to an angular accuracy of several 10 μ rad. For the purposes of the CMM test bed, a larger lever arm would have been preferred.
- The CQP needs to be aligned to the laser beam with a four-axes translation and rotation stage, since the calibration is only valid if both QPDs are centrally hit by the beam. Such stages, if desired to be reasonably stable, tend to be quite bulky, which made it difficult to place the CQP at the desired locations in the CMM test bed.

¹The original idea of CABAM was brought up by Vitali Müller (AEI).

One possible approach could have been to refine the design of the AEI in-house built CQP to overcome the main drawback, which was clearly the instability of the housing. One could have, e.g., considered a CQP housing built quasi-monolithically from ultra-stable materials such as Zerodur[®] [73]. Instead, with CABAM a new tool to align and measure a laser beam axis has been invented, which surprises by its simplicity and accuracy. All that is needed for CABAM is a single position-sensitive QPD on a 2-axes translation stage. No stable housing is required and no calibration process has to be performed.

The basic idea behind CABAM is to measure 3D-points \vec{p}_i , $i = 1, \dots, n$, along the laser beam axis and consecutively fit a 3D-ray $\vec{b}(s)$ to these points:

$$\vec{b}(s) = \vec{p}_0 + s \cdot \vec{w}. \quad (3.8)$$

As support vector for the ray we choose

$$\vec{p}_0 = \frac{1}{n} \sum_{i=1}^n \vec{p}_i. \quad (3.9)$$

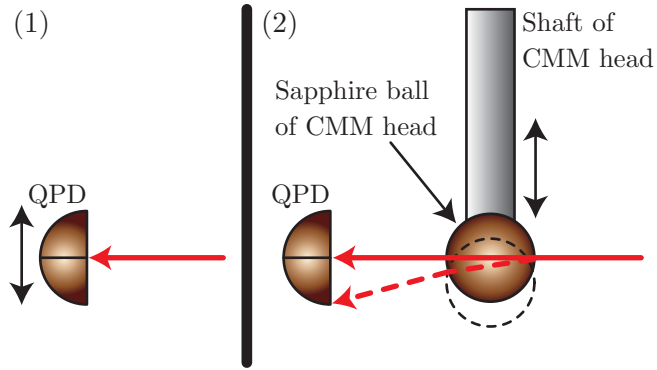
The ray direction vector \vec{w} is obtained with a least squares fit using, e.g., singular value decomposition [107]. The crucial trick of the CABAM method is how to measure 3-dimensional point positions on the beam axis.

The CMM usually measures point positions on a test object by physically probing the object with its probe sphere. The sphere is installed at the end of the CMM probe head shaft. Once a calibrated force is applied to this shaft, the CMM software records the respective position that is being probed on the test object. However, the current position of the probe sphere center is also available from the CMM software, even when the CMM probe sphere is not physically contacting an object. If we accomplish to center the CMM probe sphere in the laser beam, we can use this non-contact CMM position information to obtain a point on the laser beam axis.

Figure 3.18 illustrates the alignment procedure of the CMM probe sphere in the laser beam: (1) First, we center a position-sensitive QPD which is mounted on a two-axes translation stage in the beam. (2) Second, we take advantage of the fact that the CMM probe sphere is usually a sapphire ball: It is transmissive for the used laser light (wavelength 1064 nm) and has the same effect as a ball lens. We position the sapphire ball in the laser beam by minimizing the DPS signals (cf. Chap. 1.4.4) of the QPD. In this way, the beam remains centered on the QPD. This can only be achieved when the laser beam is passing through the center of the sapphire ball.

Now that the CMM probe head has been positioned correctly, the position of the probe sphere and thus a point \vec{p}_i on the beam axis can be read out from the CMM

Figure 3.18: (1) First, we center the incoming beam (arrow from right) on the QPD which is translated in two dimensions transversal to the beam. (2) Second, we position the CMM sapphire ball in the beam such that the beam passing through the ball remains centered on the QPD. The dashed lines show beam deflection for misplaced CMM ball. See also [102].



software. We can reconstruct the ray according to Eq. (3.8) after measuring two or more points.

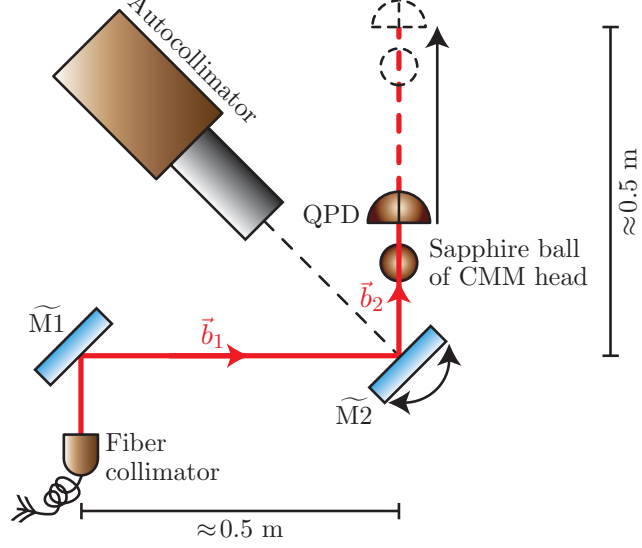
Now we need to verify the achievable positional and angular accuracies of CABAM by testing CABAM against calibrated measurement devices. The CABAM *positional* accuracy, which is limited by the non-calibrated CMM non-contact positional accuracy, is tested by centering a separate ball lens into the laser beam which can then be probed with the CMM in calibrated contact mode. The CABAM *angular* accuracy is tested against an autocollimator.

CABAM has been tested with the setup shown in Fig. 3.19. The laser beam is generated by a Mephisto 500 laser (Innolight GmbH, now Coherent Inc.) with a wavelength of 1064 nm and delivered to the fiber collimator (SUK60FC-4-A11-03, Schäfter&Kirchhoff GmbH), which produces a collimated laser beam with 1 mm waist diameter.

The beam is routed via the mirrors $\widetilde{M}1$, $\widetilde{M}2$. The orientation of mirror $\widetilde{M}2$ is observed with an autocollimator (ELCOMAT direct SN-162, Möller Wedel), which has a calibrated angular accuracy of $\pm 0.34 \mu\text{rad}$. Alignment of autocollimator axes to the horizontal plane of the CMM coordinate system to better than $\pm 1^\circ$ has been confirmed: Mirror $\widetilde{M}2$ was tilted both horizontally and vertically and autocollimator measurements were compared with mirror $\widetilde{M}2$ orientations derived from CMM measurements of the $\widetilde{M}2$ plane.

A position-sensitive QPD (silicon, 1 cm diameter, in-house electronics) is mounted on a two-axes translation stage. We can insert the QPD into the beam at various positions before and after $\widetilde{M}2$ to measure points along beams \vec{b}_1 and \vec{b}_2 . The CMM

Figure 3.19: In this setup, CABAM beam orientation measurements are compared with calibrated autocollimator angular measurements. First, position and orientation of the laser beam before (\vec{b}_1) and behind mirror $\tilde{M}2$ (\vec{b}_2) are measured with CABAM. Then mirror $\tilde{M}2$ is tilted. The tilt angle is recorded with an autocollimator. Consecutively, the new orientation of beam \vec{b}_2 is measured with CABAM. See also [102].



probe sphere can be placed very precisely in the laser beam: A $1\ \mu\text{m}$ displacement from the center of the beam results in a well-resolvable DPS displacement signal from the QPD with a signal-to-noise ratio of 2.5. The noise floor of the DPS displacement signal is dominated by beam jitter caused by the fiber collimator.

For each beam measurement, three point measurements distributed over about 0.5 m along the beam axis are performed to which a ray according to Eq. (3.8) is fitted. It takes about 10 minutes to perform a three-point beam measurement. For all measurements, fit residuals of less than $1\ \mu\text{m}$ are obtained. Furthermore, the fitted beams \vec{b}_1 and \vec{b}_2 almost intersect, approaching each other within less than $2\ \mu\text{m}$.

A beam measurement with 6 points along the beam is performed as well to improve statistics. The measured points on the laser beam have a root-mean-square distance from the fitted ray of less than $1\ \mu\text{m}$. Even the maximum distance recorded is below $1\ \mu\text{m}$. Over a distance of 0.5 m, this corresponds to an angular precision of $2\ \mu\text{rad}$.

Now the positional accuracy of CABAM is confirmed by aligning a 9.525 mm diameter sapphire ball lens (Edmund Optics, 63-227) on a two-axes translation stage at several locations in the beam \vec{b}_2 with the same alignment method used for CABAM (cf. Fig. 3.18). For each location, the ball lens position is measured with the CMM in calibrated contact mode. The deviations of measured ball lens positions from the fitted \vec{b}_2 ray are smaller than $3\ \mu\text{m}$. This is very close to the CMM measurement

accuracy of 2 μm .

In a next step, angular CABAM measurements are compared with autocollimator measurements. The orientation of the laser beam \vec{b}_2 is measured with CABAM. After tilting mirror $\widetilde{M2}$, the tilt angle is recorded with the autocollimator and the new orientation of beam \vec{b}_2 is measured with CABAM. This procedure is repeated for five different mirror $\widetilde{M2}$ orientations covering an angular range of 300 μrad both horizontally and vertically.

Note that laser beam direction and autocollimator axes are not linked in an absolute sense, so that only angular differences between the investigated mirror $\widetilde{M2}$ orientations are considered. Furthermore, geometrical factors for beam deflection off the mirror are taken into account: The beam's angle of incidence is close to 45° , thus a factor of 2 is applied for horizontal and a factor of $\sqrt{2}$ for vertical tilts.

The differences between autocollimator measurements and measured beam direction changes are symmetrically distributed around zero for both horizontal and vertical tilt angles of mirror $\widetilde{M2}$. No significant bias can be observed. The root-mean-square of the differences is less than or equal to 5 μrad for both horizontal and vertical angles, with the biggest difference being 7 μrad .

Finally, let us verify with the setup in Fig. 3.19 how CABAM can also be used to align a beam to a desired position and direction. To this end, we first set two points \vec{q}_1, \vec{q}_2 in the CMM software defining a ray

$$\vec{B}(s) = \vec{q}_1 + s \cdot (\vec{q}_2 - \vec{q}_1) \quad (3.10)$$

to which beam \vec{b}_2 shall be aligned. Next, we use the CMM probe sphere as beam target at \vec{q}_1, \vec{q}_2 to coarsely align beam \vec{b}_2 to the points \vec{q}_1, \vec{q}_2 . Near- and far-field beam positions are iteratively adjusted with mirrors $\widetilde{M1}, \widetilde{M2}$, respectively.

When the coarse alignment is accomplished, we use CABAM to measure a point \vec{p}_2 on beam \vec{b}_2 in the vicinity of \vec{q}_2 . We then move the CMM probe sphere out of the beam so that the beam directly illuminates the QPD. With DPS, Eq. (1.11), and the previously determined calibration factors $C_{\text{hor,ver}}$, we can now use the difference $(\vec{q}_2 - \vec{p}_2)$ to correct the beam position on the QPD with mirror $\widetilde{M2}$.

Consecutively, the procedure is repeated for the near-field: We measure a point \vec{p}_1 on beam \vec{b}_2 close to \vec{q}_1 and correct the beam position with mirror $\widetilde{M1}$. The alignment procedure converges quite quickly. Usually sufficient alignment is achieved after three iterations with a total duration of 10–15 minutes. Finally, the successful beam alignment is verified with CABAM: An alignment of beam \vec{b}_2 to the desired

beam position and direction \vec{B} with $(7\pm 3)\mu\text{m}$ positional and $(2\pm 10)\mu\text{rad}$ angular accuracy has been achieved.

With CABAM, a novel and easy-to-implement method has been developed to measure both laser beam direction and position or to align a laser beam to desired direction and position. CABAM uses a CMM in non-contact mode in combination with a position-sensitive QPD to center the CMM probe sphere in the laser beam. CABAM is capable of a positional accuracy of $3\mu\text{m}$ and an angular accuracy of below $10\mu\text{rad}$, as verified against calibrated devices.

3.2.3 Uncertainty of TMA vertex and PMC colocation measurement

As we have learned, the method of verifying colocation of TMA vertex and PMC involves various procedures in two test beds. On the one hand, there is an uncertainty of TMA vertex determination with the CMM. On the other hand, the BMR, the vertex of which marks the TMA PMC position, might be misplaced. Also, we have to consider that a possible offset between TMA vertex and PMC is expected to be rather small, cf. Chap. 1.3. We now derive an estimate of the overall measurement uncertainty and discuss the different error sources that enter during the various measurement steps.

The location difference of TMA vertex and BMR, $\Delta V_{\text{CMM}}^{y,z}$, as measured by the CMM in the axes of interest y, z is given by

$$\Delta V_{\text{CMM}}^{y,z} = \Delta_{\text{TMA}}^{y,z} + \Delta_{\text{BMR}}^{y,z} \pm \sigma^{y,z}. \quad (3.11)$$

Here, $\Delta_{\text{TMA}}^{y,z}$ and $\Delta_{\text{BMR}}^{y,z}$ are the differences between vertex and PMC for the TMA and the BMR, respectively. The measurement uncertainty is given by $\sigma^{y,z}$.

The equations are identical for both axes, thus we omit y and z in the following for simplicity. As we have estimated in Chap. 1.3.3.2 for a TMA built within requirements, the theoretically expected deviation between TMA vertex and PMC is $\Delta_{\text{TMA}} < 10\mu\text{m}$. The formulas given in Chap. 1.3.3.2 have been derived for the specific dimensions of the TMA with a lateral size of 600mm . Since they scale with the size of the retroreflector, we expect an even smaller vertex-to-PMC difference for the BMR, $\Delta_{\text{BMR}} < 1\mu\text{m}$, because of the much smaller BMR dimensions of below 40mm . This leaves the measurement uncertainty σ as dominant term in Eq. (3.11). We assume the following contributions for σ :

$$\sigma = \Delta_{\text{PMC}} + \Delta_{\text{PMC}}^x \cdot \phi^{\text{CS}} + \Delta V_{\text{BMR}} + \Delta V_{\text{BMR}}^{\text{CMM}} + \Delta V_{\text{TMA}}^{\text{CMM}}. \quad (3.12)$$

The different terms in Eq. (3.12) have been summed up linearly as a worst-case estimate. Their meaning is listed below:

- $\Delta\text{PMC} \approx 5 \mu\text{m}$: Difference between BMR vertex and TMA PMC after BMR placement with the help of the interferometric difference measurement. This term is deduced from the measurement noise floor, which we have discussed in Sec. 3.2.1.
- $\Delta\text{PMC}^x \cdot \phi^{\text{CS}} \approx 15 \mu\text{m}$: For the Glass TMA, interferometric measurement axis and CMM x -axis are not linked, since no pre-alignment step in the CMM is performed (cf. Sec 3.2.2.1). The misalignment angle ϕ^{CS} between both measurement axes couples the uncertainty of BMR and TMA PMC offset along the x -axis $\Delta\text{PMC}^x \approx 1 \text{ mm}$ (cf. Sec. 3.2.1) into ΔPMC^y , ΔPMC^z . For now, we assume ϕ^{CS} to be of the order of 15 mrad. In Chap. 4.2, ϕ^{CS} will be measured. For TMA DM and TMA QM, due to the pre-alignment step in the CMM, we can assume $\Delta\text{PMC}^x \leq 35 \mu\text{m}$ and $\phi^{\text{CS}} \leq 100 \mu\text{rad}$, leading to a totally negligible contribution of $\Delta\text{PMC}^x \cdot \phi^{\text{CS}} \leq 3 \text{ nm}$.
- $\Delta V_{\text{BMR}} \approx 2.5 \mu\text{m}$: This is the uncertainty with which the BMR vertex lies within the ball housing as specified by the manufacturer.
- $\Delta V_{\text{BMR}}^{\text{CMM}} \approx 2 \mu\text{m}$: Uncertainty of position of BMR ball housing center as measured with CMM by probing the BMR sphere.
- $\Delta V_{\text{TMA}}^{\text{CMM}} \approx 26 \mu\text{m}$: Uncertainty of TMA vertex extrapolation from CMM measurement of position and orientation of each TMA mirror. We estimate a CMM angular accuracy of roughly $50 \mu\text{rad}$ from the CMM positional accuracy of $2 \mu\text{m}$ divided by the maximum distance of roughly 4 cm between the points being probed on the TMA mirrors. The CMM angular accuracy is then multiplied with the lever arm of 30 cm between the TMA mirrors and the TMA vertex position, giving a contribution of $15 \mu\text{m}$ per mirror. The contributions from the three mirrors are then summed up quadratically leading to a TMA vertex uncertainty of $26 \mu\text{m}$.

With the above-listed terms, we get $\sigma \approx 51 \mu\text{m}$ for the Glass TMA and $\sigma \approx 36 \mu\text{m}$ for the TMA DM and the TMA QM. Thus we expect to be noise-dominated in the comparison of TMA vertex and TMA PMC location, since a possible expected offset is smaller than $10 \mu\text{m}$. However, if the difference between TMA vertex and TMA PMC is as small as expected, the method presented in this thesis is precise enough to confirm that TMA vertex and PMC are colocated within $\pm 100 \mu\text{m}$ within 2σ uncertainty.

3.3 LRI Optical Bench test bed

This section presents a test bed to investigate the properties and functionalities of the LRI Optical Bench. For developing and commissioning the test bed and in a subsequent test run, the AEI in-house built OBBM unit (cf. Chap.2.2) was used. Currently, the test bed is being used for tests with industry-manufactured (STI) LRI Optical Bench engineering models [87]. The LRI Optical Bench test bed as developed in this thesis has also been presented in a related publication [108].

The test bed focuses on the following LRI Optical Bench properties under local spacecraft attitude jitter: DWS signals, heterodyne efficiency, closed-loop beam steering and beam coalignment, and rotation-to-pathlength coupling. Local spacecraft attitude jitter is simulated by a hexapod, a six-degree-of-freedom rotation and translation platform.

The setup of the LRI Optical Bench test bed with the OBBM installed is depicted in Fig. 3.20. Furthermore, a CAD model and a photograph of the setup are displayed in Figs. 3.21 and 3.22. To perform the envisioned tests, the test bed needs to provide a suitable RX beam to simulate the beam coming from the distant spacecraft, a phasemeter to calculate the DWS signals and to control the beam steering loop, and auxiliary readout systems to investigate LO beam and RX beam coalignment and rotation-to-pathlength coupling. These different test bed units and their implementation are now described.

3.3.1 RX beam generation

The LRI uses heterodyne interferometry with laser beams of 1064 nm wavelength to measure intersatellite distance changes (cf. Chap.1.2). Since intersatellite velocities are several m/s, a frequency offset between the lasers on both spacecraft of some MHz is required to keep the ranging information unambiguous.

Additionally, due to the large spacecraft separation of 200 km, the RX beam that is received by the local spacecraft is expanded to a diameter of 60 m. This results in a flattop beam with flat wavefront and flat intensity profile over the 8 mm diameter aperture of the LRI Optical Bench (cf. Chap. 1.4.1, [67]).

The LRI Optical Bench test bed provides the required laser beams from two lasers (Mephisto 500, Innolight GmbH, now Coherent Inc.) with 1064 nm wavelength, which are phase-locked with a frequency offset of 6.25 MHz by an auxiliary analog phase-locked loop and delivered to the setup (Fig. 3.20) via optical fibers. While the fiber coming from the master laser is fed into the LO beam generator of the OBBM, the fiber from the slave laser is injected into the RX beam generator.

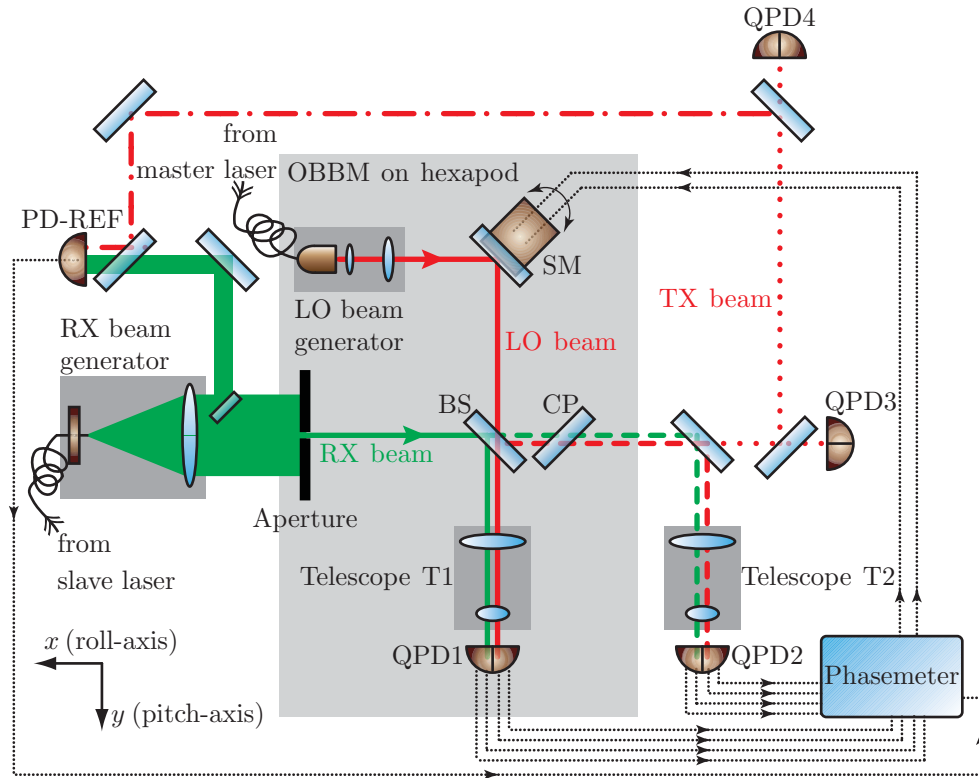


Figure 3.20: Setup of LRI Optical Bench test bed. The OBBM is installed on a hexapod which can be commanded to simulate local spacecraft attitude jitter. OBBM properties such as heterodyne efficiency between interfering LO beam and RX beam, DWS signals, closed-loop LO beam steering, and rotation-to-pathlength coupling can be investigated with auxiliary readout tools. The OBBM QPD is labeled as QPD1. Mirrors $M1$, $M2$ are not shown for simplicity (cf. Fig. 2.4). QPD2 provides DWS-measured LO beam/TX beam and RX beam coalignment. QPD3, QPD4 are sensitive to beam position and monitor TX beam orientation changes. From the difference between QPD1 and PD-REF, roundtrip pathlength changes incurred under hexapod rotations can be obtained. See also [108].

3.3 LRI OPTICAL BENCH TEST BED

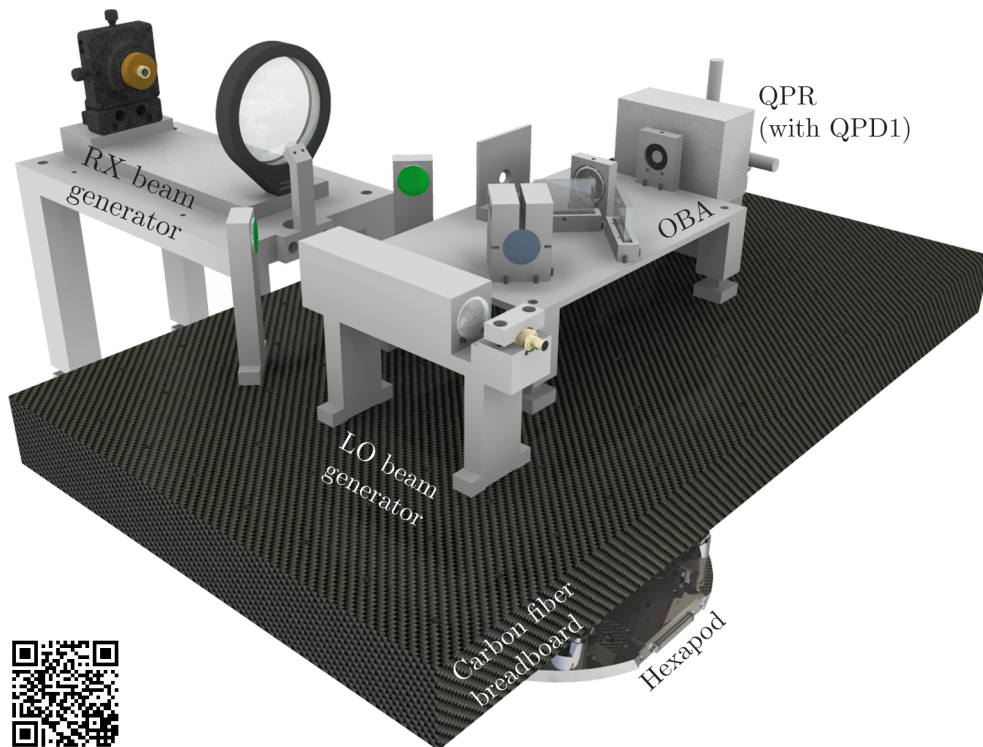


Figure 3.21: CAD model of a part of the LRI Optical Bench test bed. The OBBM is installed on a hexapod. The RX beam generator simulates the beam coming from the distant S/C. Lens mount CAD file provided by Thorlabs Inc., translation stage CAD file by Newport Corp., hexapod CAD file by PI GmbH & Co. KG. To watch an animation of this setup, scan the QR code in the lower left corner of the picture or go to www.gracefo.spacegravity.org/video8.

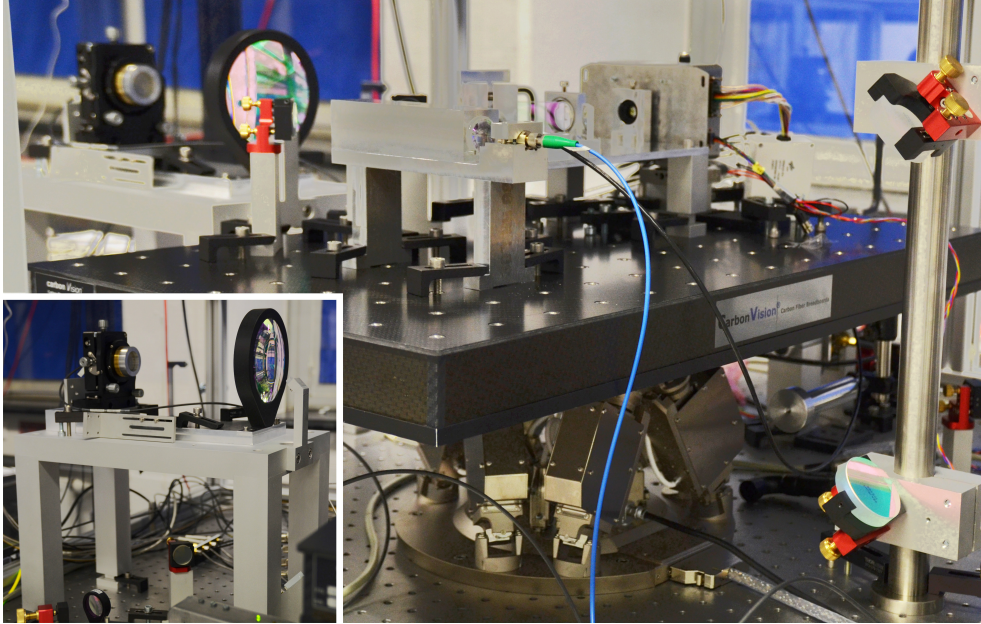


Figure 3.22: Photograph of LRI Optical Bench test bed. The OBBM is installed on a hexapod. The inset shows the RX beam generator.

The RX beam generator consists of a bare fiber end aligned to the focal point of an aspherical lens with 200 mm focal length (Thorlabs Inc., AL100200-C).² The RX beam generator, as installed in the test bed, can be seen in the CAD model of Fig. 3.21 and in the photograph of Fig. 3.22 (inset).

During the alignment of the fiber end, the beam leaving the RX beam generator is observed with a Shack-Hartmann sensor (SHS, Imagine Optics S.A., HASO3-128-GE2). Wavefront and intensity profile of the generated beam are displayed in Fig. 3.23. By fitting Zernicke polynomials up to 2nd order, “piston”, “tilt”, and “defocus”, we obtain a radius of curvature of 2 km. This shows that the fiber end has been aligned well to the focal point of the lens. The remaining visible circular structure, which can be attributed to lens errors, leads to a peak-to-valley wavefront error of 440 nm over the full SHS measurement area.

Comparing the wavefront with the intensity profile in Fig. 3.23, one can observe that phasefront center and intensity center show a horizontal and a vertical offset of some mm. However, the center of the wavefront is adjusted to the center of the OBBM aperture, since a flat wavefront is esteemed more important than a flat intensity profile.

²Design, construction, and alignment was performed by Gunnar Stede (AEI).

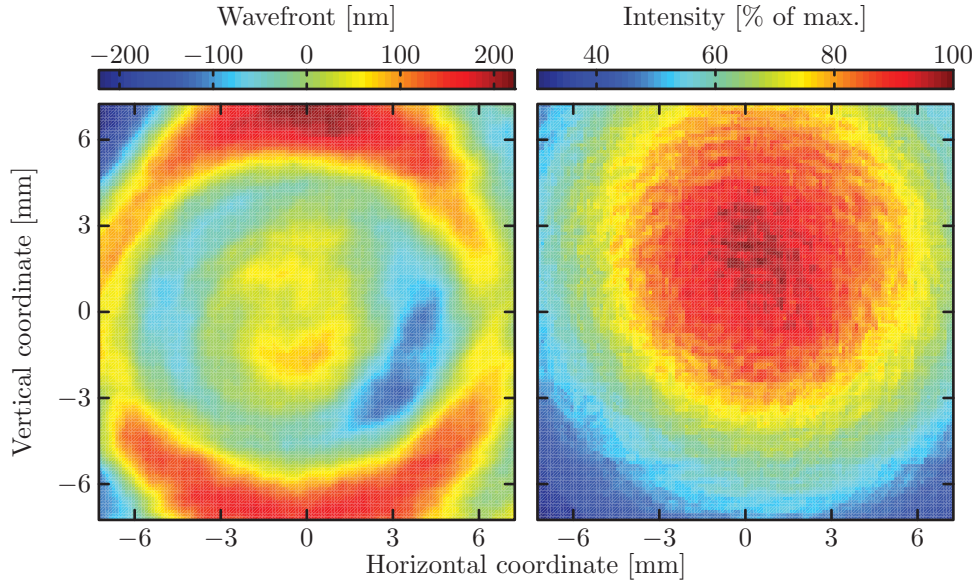


Figure 3.23: Wavefront (left) and intensity profile (right) of RX beam measured with SHS. Measurement taken by Gunnar Stede (AEI).

As we can see from the intensity profiles in Fig. 3.23, the RX beam is large enough (diameter roughly 2 cm) to overshadow the 8 mm diameter aperture of the OBBM. The part of the RX beam that was later aligned to illuminate the 8 mm diameter OBBM aperture is shown in Fig. 3.24. The peak-to-valley wavefront error over the 8 mm diameter aperture is 160 nm with an intensity drop of roughly 30%.

3.3.2 Phasemeter, DWS signal computation, and beam steering control loop

The signals of the four QPD1 segments, cf. Fig. 3.20, are recorded and processed with an AEI in-house built digital phasemeter.³ Furthermore, the phasemeter calculates DWS signals and controls the steering mirror loop. With some simplifications, this phasemeter is similar to the readout system which was originally developed for the space-based gravitational wave detector LISA [12, 13].

The phasemeter has been implemented in a field-programmable gate array (FPGA). Figure 3.25 shows a schematic overview of the phasemeter (PM) architecture.

The analog photo receiver signals from the four QPD1 segments $i = A1, B1, C1,$

³The phasemeter has been assembled, programmed, and commissioned mainly by Oliver Gerberding (formerly AEI, now working at NIST/JQI).

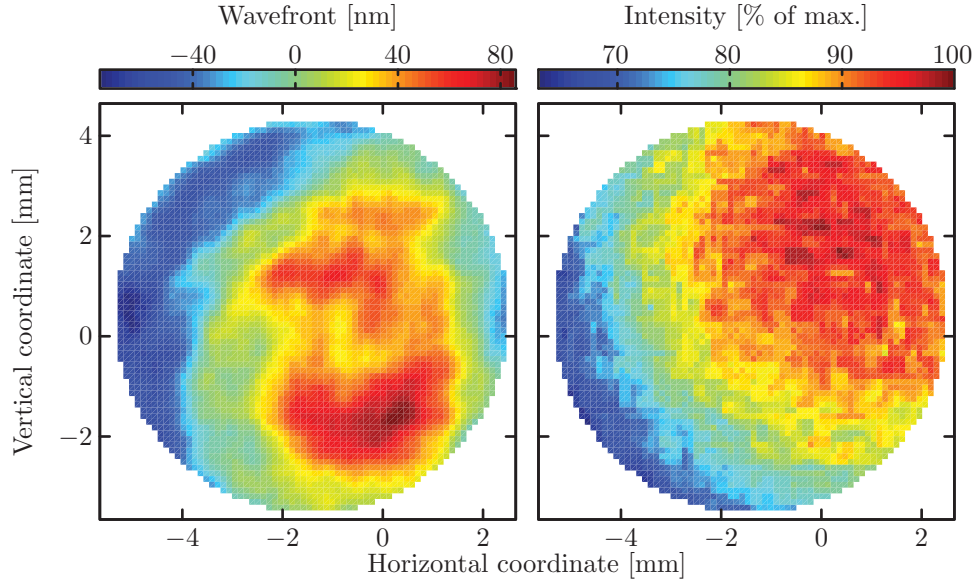


Figure 3.24: Wavefront (left) and intensity profile (right) of RX beam in 8 mm diameter OBBM aperture measured with SHS. Measurement taken by Gunnar Stede (AEI).

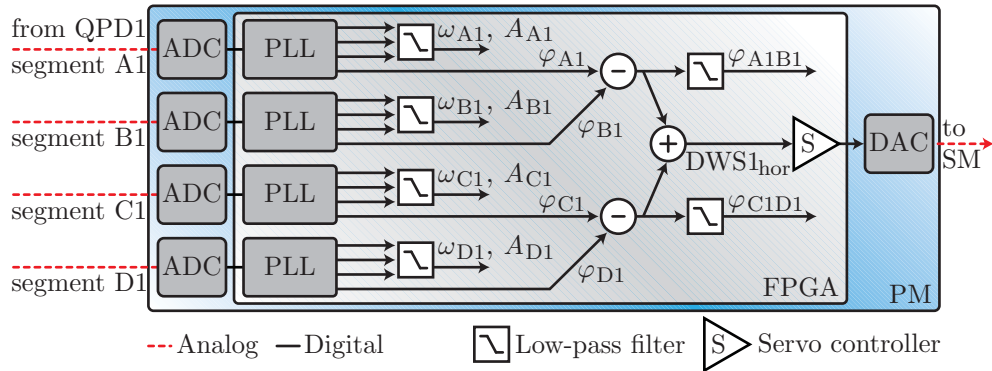


Figure 3.25: Schematic of phasemeter architecture to illustrate the generation of $DWS1_{hor}$. The generation of $DWS1_{ver}$, which is not shown here, is handled analogously. See also [108].

D1 are digitized with analog-to-digital converters (ADCs) with a sampling rate of 40 MHz. Consecutively, digital phase-locked loops (PLLs) determine frequency ω_i , amplitude A_i , and phase φ_i for each QPD1 segment, cf. Eq. (1.9) [11].

In a next step, the phasemeter calculates phase differences between the QPD1 segments according to

$$\begin{aligned}
 \varphi_{A1B1} &= \varphi_{A1} - \varphi_{B1}, \\
 \varphi_{C1D1} &= \varphi_{C1} - \varphi_{D1}, \\
 \varphi_{A1C1} &= \varphi_{A1} - \varphi_{C1}, \\
 \varphi_{B1D1} &= \varphi_{B1} - \varphi_{D1}.
 \end{aligned}
 \tag{3.13}$$

Then, the phase differences are added up appropriately to obtain the DWS signals corresponding to horizontal ($DWS1_{\text{hor}}$) and vertical ($DWS1_{\text{ver}}$) relative beam tilts between LO beam and RX beam, cf. Eq. (1.14). Note that in Fig. 3.25, only the generation of $DWS1_{\text{hor}}$ is shown. The generation of $DWS1_{\text{ver}}$ is handled analogously.

The beam steering loop is realized by feeding the DWS signals $DWS1_{\text{hor}}$ and $DWS1_{\text{ver}}$ through a single integrator, which acts as servo controller of the loop (cf. Fig. 3.25). The loop gain can be adjusted by changing the integrator gain by factors of 2 via simple bit shifting. The resulting actuator signal is transformed with digital-to-analog converters (DACs) and fed to the steering mirror electronics. Since steering mirror actuation axes are well-aligned to the DWS1/QPD1 axes within a few degrees, cross coupling between the axes is expected to be small and no additional rotation matrix calculation is necessary.

The behavior of the beam steering loop is simulated with a simple control model, as explained in Chap. 1.4.5, Fig. 1.8. The model includes the simulated DWS transfer matrix (see below, Eq. (3.14)), the digital signal processing, the variable integrator gain of the loop's servo controller, the steering mirror gain, and the optical geometry (factor 2 for horizontal tilts, $\sqrt{2}$ for vertical tilts). The steering mirror response function has been recorded with a network analyzer (Stanford Research Systems Inc.), see Fig. 3.26, and is included in the model.

Simulated beam steering open-loop transfer functions for three different integrator gain factors ("I-gains") of 2^5 , 2^4 , and 2^3 are plotted in Fig. 3.27 for both horizontal and vertical actuation axis of the beam steering loop. From the transfer functions, unity gain frequency $f_{\text{UG}}^{\text{sim}}$ and phase margin $\varphi_{\text{UG}}^{\text{sim}}$ for the three different I-gains were extracted and summarized in Tab. 3.2.

As we can see, the phase margin for an I-gain of 2^5 is insufficient to support a stable control loop operation, being 0° for the horizontal and 10° for the vertical axis. A suitable I-gain setting is 2^4 with a phase margin of 21° for the horizontal and 33°

Figure 3.26: Amplitude (top) and phase (bottom) of the OBBM steering mirror piezo response function recorded with a network analyzer. Shown are response functions for both the horizontal and the vertical actuation axis.

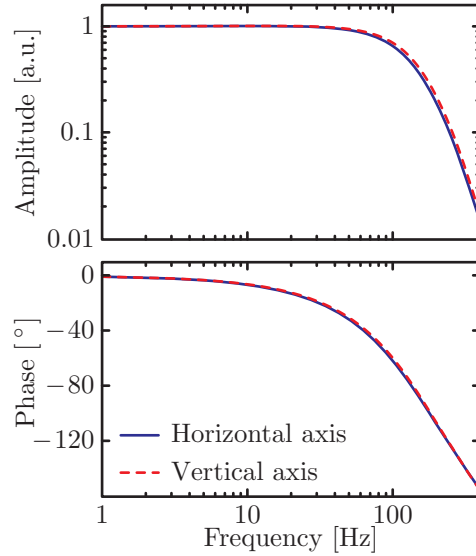


Table 3.2: Unity gain frequency $f_{\text{UG}}^{\text{sim}}$ [Hz] and phase margin $\varphi_{\text{UG}}^{\text{sim}}$ [°] for three different I-gains and both horizontal and vertical axis of the simulated beam steering loop.

	I-gain	$f_{\text{UG}}^{\text{sim}}$	$\varphi_{\text{UG}}^{\text{sim}}$
Horizontal	2^5	150	0
	2^4	103	21
	2^3	64	44
Vertical	2^5	125	10
	2^4	82	33
	2^3	48	54

for the vertical axis at unity gain frequencies of 103 Hz and 82 Hz, respectively. While for the actual satellite mission, a much lower unity gain frequency would also be sufficient, since satellite attitude jitter is expected to be present only well below 1 Hz, higher unity gain frequencies are advantageous in the noisy environment of standard laboratory conditions.

When closing the OBBM beam steering loop in Chap. 4.3, an I-gain of 2^4 is chosen as starting point, as this promises to support stable loop operation. Then the open-loop transfer function can be recorded with a network analyzer and, if necessary, the I-gain can be adjusted.

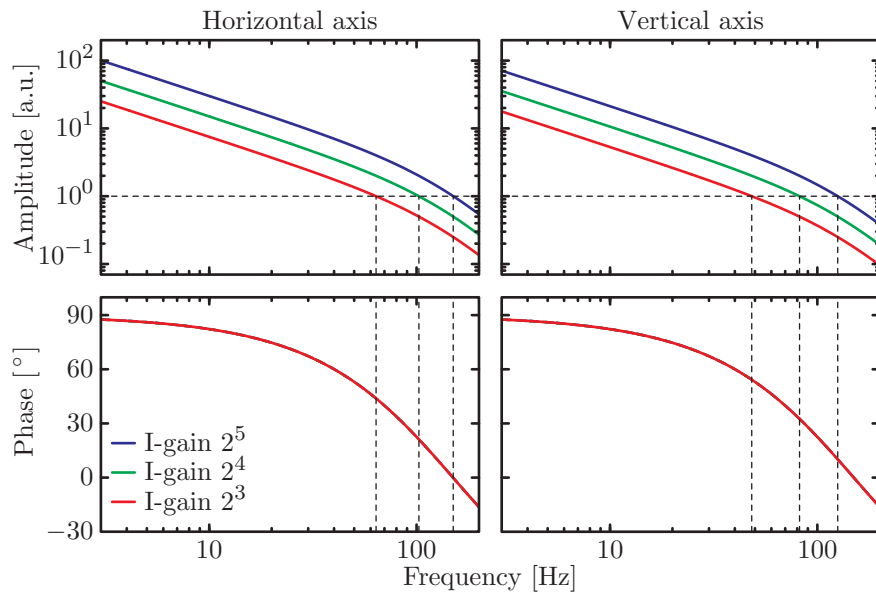


Figure 3.27: Amplitude (top row) and phase (bottom row) of the simulated beam steering open-loop transfer function. Both horizontal (left column) and vertical (right column) actuation axis are shown. Simulations were performed for three different I-gains of 2^5 , 2^4 , and 2^3 .

3.3.3 Simulation of DWS signals and heterodyne efficiency

The DWS signals from QPD1 (cf. Fig. 3.20) can be calibrated to corresponding horizontal and vertical LO beam and RX beam relative wavefront tilts at the beam splitter by performing calibrated hexapod yaw and pitch rotations, respectively. The relation between the DWS signals and the wavefront tilt is given by the DWS transfer matrix $M1$, as defined in Eq. (1.14).

In a Matlab[®]-based environment, the interference of LO beam and RX beam under hexapod rotations was simulated using the specific parameters of the OBBM and of the LRI Optical Bench test bed (cf. Chap. 2.2 and Sec. 3.3.1): Gaussian LO beam with 4.6 mm waist diameter, flattop RX beam with 8 mm diameter, OBBM telescope T with 1/8 demagnification, QPD1 active area of 1 mm diameter, and QPD1 slit width of 44 μm . Perfect alignment of QPD1 segments and hexapod coordinates is assumed, leading to zero off-diagonal elements of the DWS1 transfer matrix $M1$ (cf. Eq. (1.14)) and to $M1_{11}^{\text{sim}} = -M1_{22}^{\text{sim}}$. Furthermore, flat LO beam and RX beam wavefronts and a flat RX beam intensity profile are assumed.

First, the Gaussian LO beam wavefront is generated on a 512×512 grid covering the QPD1 active area. Then flattop wavefronts with horizontal and vertical tilts ranging from $-550 \dots 550 \mu\text{rad}$ with $10 \mu\text{rad}$ step size are computed to simulate RX beam tilts caused by hexapod yaw and pitch rotations. Consecutively, each RX beam wavefront is interfered with the LO beam wavefront. The phases φ_i and the interferometric contrast κ_i , $i = A1, B1, C1, D1$ (cf. Chap. 1.4.3), are obtained by integrating over each QPD1 segment.

With the phases φ_i , $i = A1, B1, C1, D1$, the DWS signals $DWS1_{\text{hor}}$, $DWS1_{\text{ver}}$ are calculated according to Eq. (1.14). The results are shown in Fig. 3.28. The simulated DWS1 transfer matrix $M1^{\text{sim}}$ is determined with Eq. (1.14) inside the linear region for small pitch and yaw angles:

$$M1^{\text{sim}} = \begin{pmatrix} 15,600 & 0 \\ 0 & -15,600 \end{pmatrix} \cdot 1 \text{ rad/rad}. \quad (3.14)$$

Furthermore, the heterodyne efficiency for each of the four QPD1 segments is computed from the simulations using Eq. (1.10). The heterodyne efficiency is displayed in Fig. 3.29. For perfectly aligned LO beam and RX beam and with the specific parameters of this setup, the heterodyne efficiency for each QPD1 segment reaches a maximum value of

$$\gamma_{\text{max}}^{\text{sim}} = 60\%. \quad (3.15)$$

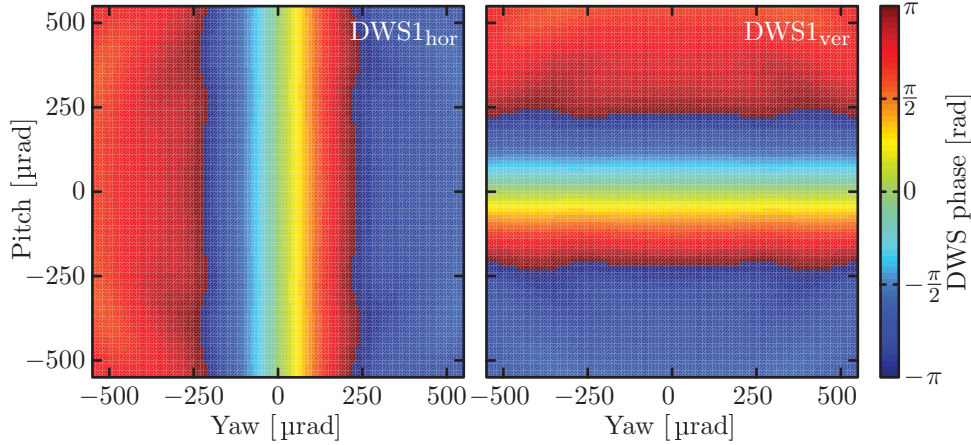


Figure 3.28: Numerically simulated DWS signals on QPD1 under hexapod pitch and yaw rotations. DWS signals corresponding to horizontal beam tilts are shown on the left, DWS signals corresponding to vertical beam tilts on the right. See also [108].

3.3.4 Coalignment of LO beam and RX beam

The LRI Optical Bench test bed in Fig. 3.20 offers auxiliary measurements to verify successful beam steering operation. Since the DWS signals of the in-loop OBBM QPD (QPD1) are inherently small due to the suppression of the loop, an independent out-of-loop measurement is required to verify the coalignment of LO beam/TX beam and RX beam during closed-loop beam steering. This is achieved by the out-of-loop DWS measurement of QPD2, for which DWS signals $DWS2_{hor}$, $DWS2_{ver}$ and DWS transfer matrix $M2$ are defined analogously to Eq. (1.14). Signal processing for QPD2 is also performed using the phasemeter. Calibration of DWS2 and determination of $M2$ is performed simultaneously with DWS1 calibration in Chap. 4.3.4.

While during the actual satellite mission the RX beam is very weak (a few hundred pW), the light powers in the LRI Optical Bench test bed can be adjusted so as to further investigate both the LO beam that is being reflected at the OBBM beam splitter (TX beam) and the transmitted RX beam leakage.

Analogously to the OBBM scheme (cf. Chap. 2.2.1), the auxiliary DWS measurement of QPD2 features a telescope T2, which simultaneously images OBBM aperture and steering mirror plane on QPD2 (see Fig. 3.20). Additionally, T2 demagnifies the beams by a factor of $\approx 1/8$ to fit on the 1 mm diameter QPD2 (Hamamatsu Photonics K.K., G6849-01, InGaAs, in-house electronics). This is achieved by a telescope T2 lens selection with focal lengths for a wavelength of 1064 nm of 762.48 mm and 101.65 mm (Thorlabs Inc., LA1978-C and LA1509-C). The first lens of telescope T2

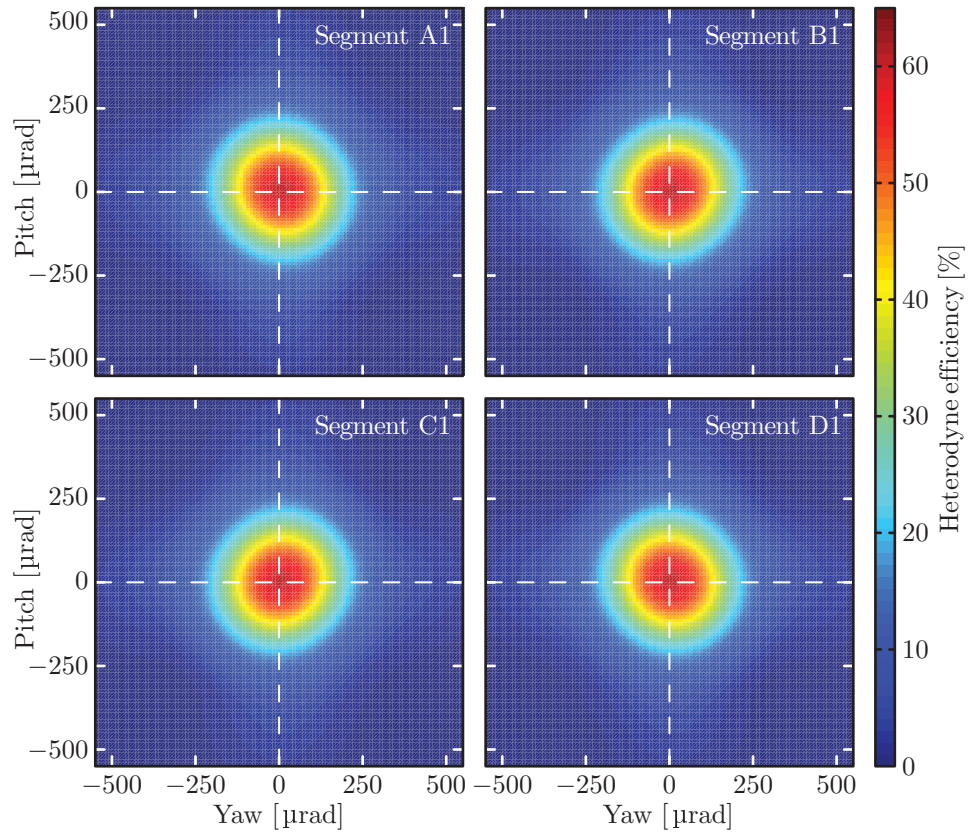


Figure 3.29: Numerically simulated heterodyne efficiency for each segment of QPD1 under hexapod pitch and yaw rotations. See also [108].

is positioned at a distance of 762.48 ± 5 mm from the OBBM aperture. The second lens is aligned in the same way as lens L2 of the OBBM telescope, cf. Chap. 2.2.4.

After telescope T2 alignment, the TX beam is centered on QPD2 by translating QPD2 transversally to the beam and minimizing the DPS signals, cf. Chap. 1.4.4. The alignment of the QPD2 position along the beam direction to place QPD2 at the image plane of T2 is performed simultaneously with the alignment of QPD1 in Chap. 4.3.1.

The LRI Optical Bench test bed (Fig. 3.20) features another auxiliary tool to investigate OBBM beam steering, consisting of two position-sensitive QPDs, QPD3 and QPD4 (1 cm diameter, silicon, in-house electronics; see also [73]). This tool offers a DWS-independent verification of closed-loop beam steering using DPS by monitoring horizontal and vertical changes of TX beam orientation, TX_{hor} and TX_{ver} respectively. Using Eq. (1.11), we define

$$\begin{aligned}\text{TX}_{\text{hor}} &= C_{\text{hor}} \cdot (\Delta_{\text{hor},3} - \Delta_{\text{hor},4}), \\ \text{TX}_{\text{ver}} &= C_{\text{ver}} \cdot (\Delta_{\text{ver},3} - \Delta_{\text{ver},4}),\end{aligned}\tag{3.16}$$

where Δ_3 , Δ_4 are the DPS signals from QPD3, QPD4, respectively. The calibration factors C_{hor} , C_{ver} are determined in the setup in Fig. 3.20 by calibrated hexapod yaw and pitch rotations. The large lever between QPD3 and QPD4 of almost 2 m promises, in conjunction with DPS beam position measurements of $\pm 10 \mu\text{m}$, an angular measurement uncertainty of better than $\pm 10 \mu\text{rad}$.

3.3.5 Measuring rotation-to-pathlength coupling

As we have seen in Chap. 1.4.2, the beam splitter on the LRI Optical Bench causes a big linear rotation-to-pathlength coupling of 2.2 mm/rad for yaw rotations, which is suppressed by the compensation plate. For the OBBM beam splitter with 5 mm thickness and a refractive index of $n_{\text{BK7}} = 1.5066$ for a wavelength of 1064 nm, we can calculate an expected linear rotation-to-pathlength coupling of 1.7 mm/mrad for yaw rotations.

The LRI Optical Bench test bed offers an auxiliary phase readout to measure the linear rotation-to-pathlength coupling caused by the beam splitter and to verify the cancellation of this linear term by use of the compensation plate. This is accomplished by branching off a part of the RX beam before it enters the OBBM (cf. Fig. 3.20). This part is then interfered with the TX beam (dot-dashed line), which is bypassing the OBBM, on the photodiode PD-REF. By taking the phase differences between QPD1 (coherent sum of all four segments) and PD-REF, the LRI roundtrip measurement is emulated and effects of OBBM rotations on the roundtrip measurement can

be investigated.

Furthermore, due to the mounting strategy of the OBBM optics (cf. Chap. 2.2.1), the compensation plate can easily be removed and reinstalled. This allows for measuring OBBM rotation-to-pathlength coupling with and without compensation plate.

3.3.6 QPD phase offsets

Electronic phase offsets between QPD segments couple directly into the DWS measurement according to Eq. (1.14). Thus they have to be calibrated beforehand and their stability under ambient conditions has to be verified.

In the LRI Optical Bench test bed (Fig. 3.20), this is accomplished by amplitude-modulating the light coupled into the LO beam generator with a fiber-coupled amplitude modulator (Jenoptik AG, AM 1064) with the RX beam being blocked. This simulates an interference beatnote between two perfectly aligned near-Gaussian beams, which optically produces the same phase on each QPD segment. Thus from this measurement, electronic phase-offsets between the QPD segments can be calibrated and subtracted in the phasemeter signal processing chain. Phase offset calibration for both QPD1 and QPD2 is performed simultaneously in Chap. 4.3.1.

Chapter 4

Test results

This chapter presents the test results obtained with the three test beds introduced in the previous chapter. In the TMA beam coalignment test bed, the CFRP TMA has been investigated. The TMA rotation-to-pathlength coupling test bed was used to characterize the Glass TMA, the TMA DM, and the TMA QM. Finally, the AEI in-house built OBBM unit was tested in the LRI Optical Bench test bed.

The test runs have served two purposes. On the one hand, the test items were investigated. This was important to verify the LRI design in early project stages and for the Critical Design Review, which was successfully passed at NASA/JPL in June 2014. On the other hand, the test beds have been commissioned and characterized during the tests, which is important for future test runs with LRI hardware such as LRI Optical Bench engineering models or possibly flight units.

4.1 TMA beam coalignment test bed

Static beam coalignment for the CFRP TMA (cf. Chap. 2.1) was measured with the TMA beam coalignment test bed (cf. Chap. 3.1). While the measurements themselves were performed in collaboration with CSIRO personnel, the processing and evaluation of the obtained data as presented here has been solely performed within this thesis. The results have been summarized in a project internal test report [109] and in related publications [50, 53].

4.1.1 TMA beam coalignment test results

Beam coalignment measurements were performed for different TMA mounting types (“center-mounting” and “2-point support”, cf. Fig. 3.5), orientations $\phi_{\text{tube}} \approx 180^\circ, 0^\circ$, and compensation loads installed at the TMA bracket to study the effect of gravity on the TMA beam coalignment. Furthermore, beam coalignment was measured for the “zero-gravity” mounting type, which has been introduced in Chap. 3.1.

The interferograms that have been recorded in the test bed (cf. Fig. 3.1) are shown in Fig. 4.1. All interferograms have been processed as described in Chap. 3.1 using the evaluation tool that had been developed to obtain the TMA beam coalignment information. Each interferogram has been processed 10 times to verify the repeatability of the procedure, which was below $\pm 1 \mu\text{rad}$ for all parameters.

The main systematic error source in the measurement scheme is the non-flatness of the reference bar, which was below $4 \mu\text{rad}$ for all runs. Furthermore, this systematic error is effectively subtracted during the evaluation process, as we have seen in Chap. 3.1, with residuals below $\pm 1 \mu\text{rad}$. The test results are summarized in Tab. 4.1.

4.1.2 Discussion

As we can see in Tab. 4.1, the nominal “zero-gravity” mounting (measurement no. (2)) achieves a root-mean-square coalignment error of $\delta_{\text{RMS}} = 9 \mu\text{rad}$.

When center-mounting the TMA by its bracket, (7) and (8), we observe a root-mean-square coalignment error of $\delta_{\text{RMS}} = 16 \mu\text{rad}$ for $\phi_{\text{tube}} = 186^\circ$ and $\delta_{\text{RMS}} = 41 \mu\text{rad}$ for $\phi_{\text{tube}} = 6^\circ$. We expect a larger coalignment error for center-mounting due to gravity causing TMA deformations. As expected intuitively, there is mainly an effect on the vertical coalignment error $\delta_{\text{ver}}^{\text{TMA}}$ when changing the tube orientation, whereas the horizontal coalignment error $\delta_{\text{hor}}^{\text{TMA}}$ remains unchanged. This can be explained by gravity bending the tube in the vertical direction.

When we compare the results for center-mounting, (7) and (8), to the ones for

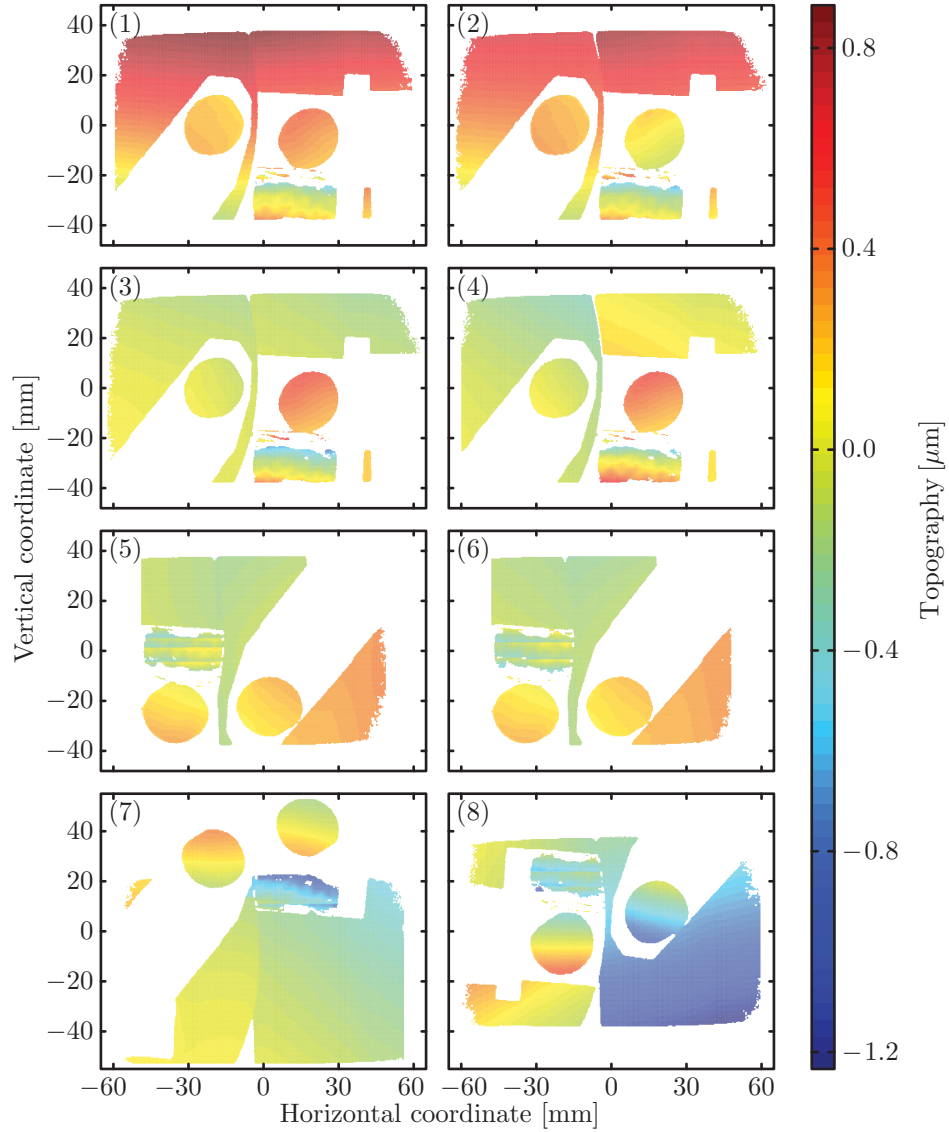


Figure 4.1: Interferograms recorded for CFRP TMA. The configurations and the recovered TMA beam coalignment angles for the measurements (1)–(8) are summarized in Tab. 4.1.

Table 4.1: TMA beam coalignment errors for different TMA mounting types (“2-point support”, “center-mounting”), orientations ϕ_{tube} , and center loads installed at the TMA bracket. The nominal “zero-gravity” mounting is indicated (measurement no. (2)). The interferograms for measurements (1)–(8) are shown in Fig. 4.1.

No.	Mounting	Load [g]	ϕ_{tube} [°]	$\delta_{\text{hor}}^{\text{TMA}}$ [μrad]	$\delta_{\text{ver}}^{\text{TMA}}$ [μrad]	δ_{RMS} [μrad]
(1)	2-point	0	184	−2	8	8
(2)	(zero-gravity)	30	184	−3	9	9
(3)		93	184	−3	11	11
(4)		184	184	−2	14	14
(5)		30	5	−3	13	13
(6)		93	5	−3	10	11
(7)	Center	0	186	−5	−16	17
(8)		0	6	−3	41	41

“zero-gravity” mounting (2), we find a difference of $-25 \mu\text{rad}$ for $\delta_{\text{ver}}^{\text{TMA}}$ for $\phi_{\text{tube}} = 186^\circ$, whereas for $\phi_{\text{tube}} = 6^\circ$, the difference is $32 \mu\text{rad}$. The sign flip can be explained by the tube bending in the opposite direction when turning it around by 180° . The size of the effect is only marginally different for the two considered orientations, which might be caused by TMA tube stiffness asymmetries.

In a consecutive test run with an Intellium H2000 interferometer and a different measurement method, a root-mean-square beam coalignment of $12 \mu\text{rad}$ was measured for the same TMA for “zero-gravity” mounting [82], which agrees very well with the results presented here. The slight discrepancy can either be attributed to the measurement uncertainty or to glue shrinkage effects at the CFRP-to-glass interface between the measurements.

4.1.3 Conclusion

The beam coalignment of the CFRP TMA has been measured with the TMA beam coalignment test bed. With a gravity-compensating mount, a root-mean-square beam coalignment error of $\delta_{\text{RMS}} = 9 \mu\text{rad}$ was confirmed, which fulfills the requirement of $10 \mu\text{rad}$ given in Chap. 1.3.3.1. The repeatability of the measurement is within $\pm 1 \mu\text{rad}$. The main source for systematic errors is the non-flatness of the reference bar, which is smaller than $4 \mu\text{rad}$. However, this effect is subtracted during the evaluation process, as explained in Chap. 3.1.2. The analysis results in Chap. 3.1.3 confirm that any influence on the final beam coalignment result is within $\pm 1 \mu\text{rad}$.

4.2 TMA rotation-to-pathlength coupling test results

Rotation-to-pathlength coupling has been investigated for the Glass TMA, the TMA DM, and the TMA QM (cf. Chap. 2.1) in the TMA rotation-to-pathlength coupling test bed (cf. Chap. 3.2).

The test campaign with the Glass TMA was very useful to commission the test bed and to refine the detailed test procedure. Since the Glass TMA was available for a period of three months, there was enough time to gain experience with the test bed and study difficulties in detail. Furthermore, the whole measurement procedure has been performed twice to verify the repeatability.

For the Glass TMA, the optical measurement axis (cf. Chap. 3.2.1) and the CMM x -axis (cf. Chap. 3.2.2) were not linked. However, the alignment between both axes was measured afterwards to estimate the resulting uncertainty in PMC location (cf. Chap. 3.2.3). The test procedure has been improved for the TMA DM and the TMA QM by introducing the pre-alignment step in the CMM (cf. Chap. 3.2.2). In this step, the nominal TMA incident beam axis is referenced by centering two QPDs in an auxiliary beam. By this, the nominal TMA incident beam axis can be reconstructed for the interferometric measurements (cf. Chap. 3.2.1).

The TMA DM and the TMA QM were only available for a very short time of two weeks each, thus a detailed test procedure had to be written in advance to make sure that each test step could be performed without delay [110]. The test procedure was exercised with the TMA DM. This test run also served for identifying final caveats in the test procedure. Consecutively, a detailed test plan was elaborated in close cooperation with STI to meet the strict regulations dictated for the TMA QM considering handling, inspection, and cleanliness [111].

The test campaigns presented here have been documented in project internal test reports [112–114]. Furthermore, the results of the first test campaign performed with the Glass TMA have been published [54].

4.2.1 Pre-alignment in CMM

This step was performed for the TMA DM and TMA QM test campaigns following the procedure described in Chap. 3.2.2.1. For both test campaigns, the BMR was placed at the TMA vertex to a precision of better than $\pm 35\ \mu\text{m}$ in each axis via iterative CMM measurements of BMR position and TMA vertex position as determined from the intersection point of the three TMA mirror planes.

Furthermore, a laser beam was aligned to the nominal TMA incident beam axis

using CABAM. With the high CABAM accuracies (cf. Chap. 3.2.2.4), a positional alignment within $\pm 10 \mu\text{m}$ and an angular alignment of $\pm 50 \mu\text{rad}$ was achieved. After alignment, the beam was referenced with two position-sensitive QPDs installed on the carbon fiber breadboard (see Fig. 3.17). The QPDs were installed with a relative distance of 0.5 m. By centering the QPDs in the laser beam by better than $\pm 10 \mu\text{m}$, a beam referencing uncertainty of below $\pm 40 \mu\text{rad}$ was achieved.

4.2.2 Locating the TMA PMC

The TMA units mounted on the carbon fiber breadboard were installed on the hexapod platform (cf. Chap. 3.2.1, Fig. 3.9). For the Glass TMA, the TMA beam was aligned to the hexapod x -axis by moving the hexapod along the x -axis and observing beamwalk of the retroreflected beam on QPD-TMA (cf. Fig. 3.9). By adjusting the angle of incidence of the TMA beam with a steering mirror, the beamwalk was minimized. Systematic errors in hexapod motion limit this alignment procedure to about $\pm 1 \text{ mrad}$.

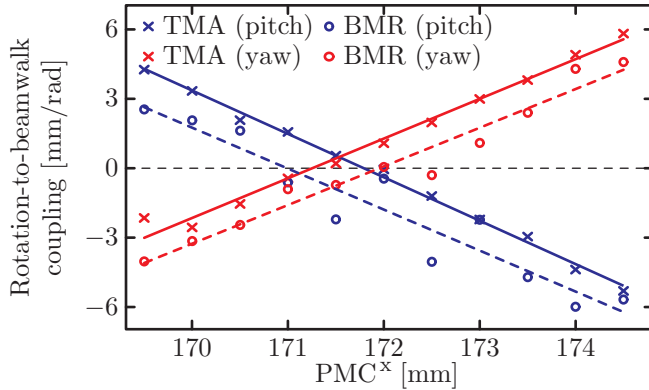
For the TMA DM and the TMA QM, the TMA beam was centered on the two position-sensitive QPDs which reference the nominal TMA incident beam axis, cf. Sec. 4.2.1. The beam was centered on the QPDs down to $\pm 10 \mu\text{m}$. Considering the distance between the QPDs of 0.5 m, a reconstruction uncertainty of the TMA incident beam axis of $\pm 40 \mu\text{rad}$ can be inferred.

In the next step, the BMR beam was aligned to the TMA beam. Again, the hexapod was moving along the x -axis, but this time *differential* beamwalk between the measurements of QPD-TMA and QPD-BMR was minimized, cf. Fig. 3.9. With this procedure, a relative coalignment between TMA beam and BMR beam of $\pm 200 \mu\text{rad}$ is achieved.

After beam alignment, the TMA PMC and the BMR positions were determined in hexapod coordinates. For the TMA DM and the TMA QM, the TMA PMC and the BMR were already colocated quite well due to the pre-alignment in the CMM, cf. Sec. 4.2.1. However, for the Glass TMA, the pre-alignment in the CMM had not been performed, so that the determination of the BMR's position in hexapod coordinates was used to correct the BMR position with respect to the TMA PMC.

To determine TMA PMC^x and BMR^x in hexapod coordinates, calibrated hexapod rotations in pitch and yaw by 1 mrad were performed while stepping the hexapod rotation pivot PP along the x -axis in 0.5 mm increments and measuring beamwalk of outgoing TMA beam and BMR beam on QPD-TMA and QPD-BMR, respectively (cf. Fig. 3.9). Figure 4.2 shows an exemplary measurement, which was taken for the TMA DM. Rotation-to-beamwalk coupling is shown for pitch (blue markers) and yaw (red

Figure 4.2: *Locating TMA PMC^x and BMR^x in hexapod coordinates. The hexapod performs 1 mrad rotations in pitch (blue markers) and yaw (red markers) for varying rotation pivot PP^x , while beamwalk of outgoing TMA beam (crosses) and BMR beam (circles) is observed. The zero-crossings of the linear fits yield PMC^x (solid lines) and BMR^x (dashed lines).*



markers) for both TMA beam (crosses) and BMR beam (circles). The zero-crossings of the linear regressions to the data points (solid lines: TMA, dashed lines: BMR) yield PMC^x and BMR^x . Pitch and yaw rotations should give the same result. However, the zero-crossings for pitch and yaw differ by roughly 1 mm, which is assumed to be the measurement uncertainty. As we can see, TMA PMC^x and BMR^x are collocated within less than ± 1 mm.

To determine $PMC^{y,z}$ and $BMR^{y,z}$ in hexapod coordinates, again calibrated hexapod rotations in yaw and pitch by 1 mrad were performed, but this time PP^y and PP^z were varied in increments of 0.2 mm. During the rotations, pathlength changes to TMA and BMR were measured interferometrically on TMA-PD and BMR-PD, cf. Fig. 3.9. Again, an example of the measurements from the TMA DM test campaign is shown in Fig. 4.3 for yaw rotations and in Fig. 4.4 for pitch rotations. Measurements for the TMA (crosses) and the BMR (circles) agree very well. Linear regression curves (solid line: TMA, dashed line: BMR) show zero-crossings that coincide within less than ± 0.1 mm, which is also expected to be the measurement uncertainty of this approach.

After determination of the TMA PMC in hexapod coordinates and confirming sufficient coarse alignment of the BMR position with respect to the TMA PMC, relative length changes δL_{rel} between the BMR measurement and the TMA measurement according to Eq. (3.7) were monitored, while the hexapod was executing rotational steps $\delta\theta_{\text{roll}}$, $\delta\theta_{\text{pitch}}$, $\delta\theta_{\text{yaw}}$ and translational steps δx , δy , δz . During this final alignment procedure, the TMA PMC location in hexapod coordinates was used as nominal

Figure 4.3: Locating TMA PMC^y and BMR^y in hexapod coordinates. The hexapod performs 1 mrad yaw rotations for varying rotation pivot PP^y , while distance changes to TMA (crosses) and BMR (circles) are measured interferometrically. The zero-crossings of the linear fits yield PMC^y (solid line) and BMR^y (dashed line).

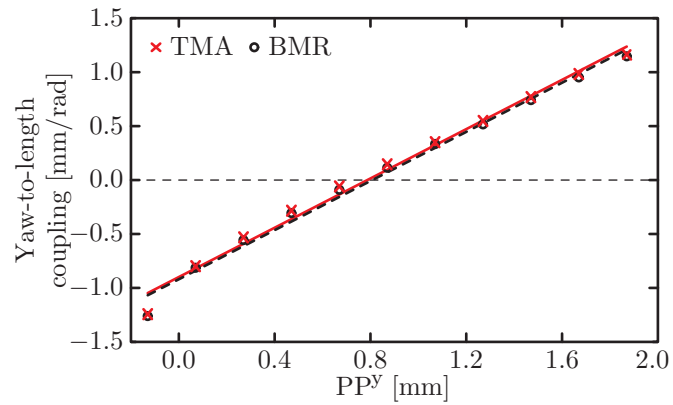
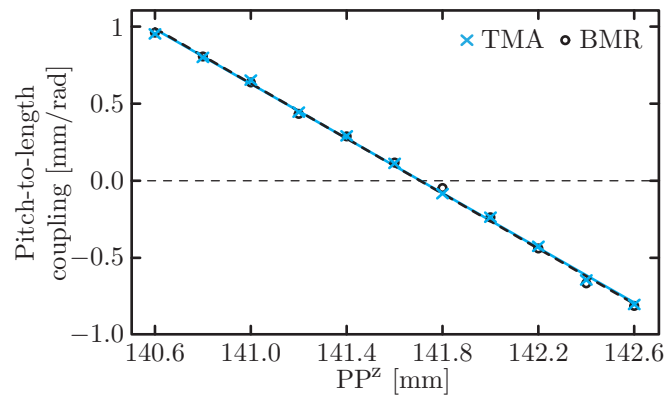


Figure 4.4: Locating TMA PMC^z and BMR^z in hexapod coordinates. The hexapod performs 1 mrad pitch rotations for varying rotation pivot PP^z , while distance changes to TMA (crosses) and BMR (circles) are measured interferometrically. The zero-crossings of the linear fits yield PMC^z (solid line) and BMR^z (dashed line).



hexapod rotation pivot, as this reduces beamwalk and associated measurement noise, cf. Chap. 3.2.1.

Relative length changes δL_{rel} under hexapod pitch and yaw rotations, $\delta\theta_{\text{pitch}}$ and $\delta\theta_{\text{yaw}}$, were used as alignment signal to iteratively fine-tune the BMR position along the z - and y -axis such that the differences ($\text{PMC}^z - \text{BMR}^z$) and ($\text{PMC}^y - \text{BMR}^y$) were minimized, cf. Eq. (3.7).

In Eq. (3.7), we assume perfect alignment of TMA beam and BMR beam so that the translational steps δx , δy , δz of the hexapod do not couple into δL_{rel} . Thus during the measurement, translational coupling into δL_{rel} could be used to check the relative alignment of TMA beam and BMR beam.

While in the simplified case of Eq. (3.7), roll rotations $\delta\theta_{\text{roll}}$ do not couple, we have learned in Chap. 1.3.3.2 that non-zero TMA mirror misalignments lead to a non-vanishing rotation-to-pathlength coupling term for roll, see Eq. (1.7).

To make averaging possible, the hexapod has performed the steps $\delta\theta_{\text{roll}}$, $\delta\theta_{\text{pitch}}$, $\delta\theta_{\text{yaw}}$, δx , δy , δz going forth and back N -times each. The step sizes were $\delta\theta_{\text{roll}} = \delta\theta_{\text{pitch}} = \delta\theta_{\text{yaw}} = 2 \text{ mrad}$, $\delta x = 2 \text{ mm}$, and $\delta y = \delta z = 0.2 \text{ mm}$.

For the Glass TMA with $N = 10$ steps for each rotation and translation, relative length changes δL_{rel} for each hexapod step are shown in Fig. 4.5. The red dashed line shows measurements of δL_{rel} before the final positioning step of the BMR. For pitch, steps 11–20, relative length changes are $\delta L_{\text{rel}} \approx 50 \text{ nm}$. Since $\delta\theta_{\text{pitch}} = 2 \text{ mrad}$, this corresponds to a TMA PMC and BMR position difference of $-25 \mu\text{m}$ along the z -axis, cf. Eq. (3.7).

The BMR was translated accordingly by $-25 \mu\text{m}$ along the z -axis. The subsequent measurement of the relative pathlength changes δL_{rel} is also shown in Fig. 4.5, solid black line. Now for both pitch and yaw (steps 11–30), δL_{rel} is dominated by noise of about $\pm 10 \text{ nm}$, which is equivalent to a difference between the BMR and the TMA PMC of $\pm 5 \mu\text{m}$ along the z - and the y -axis, respectively.

The residual measurement noise for pitch and yaw, see steps 11–30 in Fig. 4.5, is most likely caused by erroneous hexapod motion of $\pm 500 \text{ nm}$, cf. Chap. 3.2.1. This erroneous motion couples into δL_{rel} via relative TMA beam and BMR beam misalignments. From steps 41–60, we find a translational coupling for δy and δz translations of less than $25 \text{ nm}/0.2 \text{ mm}$, which corresponds to a misalignment between TMA beam and BMR beam of less than $125 \mu\text{rad}$ both vertically and horizontally.

Additionally, for roll rotations $\delta\theta_{\text{roll}}$, see steps 1–10 in Fig. 4.5, we find a non-vanishing rotation-to-pathlength coupling of about $-20 \text{ nm}/2 \text{ mrad} = -10 \mu\text{m}/\text{rad}$, which could be caused by non-zero misalignment angles between the TMA mirrors, cf. Eq. (1.7).

The relative length changes δL_{rel} in Fig. 4.6 for TMA DM (blue line) and TMA

Figure 4.5: For the Glass TMA, δL_{rel} is measured during hexapod rotations $\delta\theta_{\text{roll}}$, $\delta\theta_{\text{pitch}}$, $\delta\theta_{\text{yaw}}$ of 2 mrad and translations δx of 2 mm and δy , δz of 0.2 mm. Measurements before (red) and after (black) final alignment of BMR position with respect to TMA PMC along the z -axis are shown. One measurement taken per step, solid lines are only guides to the eye. See also [54].

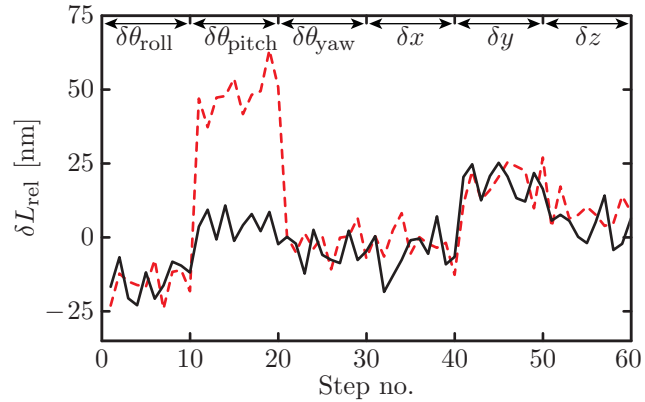


Figure 4.6: For the TMA DM (blue line) and the TMA QM (green line), δL_{rel} is measured during hexapod rotations $\delta\theta_{\text{roll}}$, $\delta\theta_{\text{pitch}}$, $\delta\theta_{\text{yaw}}$ of 2 mrad and translations δx of 2 mm and δy , δz of 0.2 mm. The BMR has already been positioned at the respective TMA PMC. One measurement taken per step, solid lines are only guides to the eye.

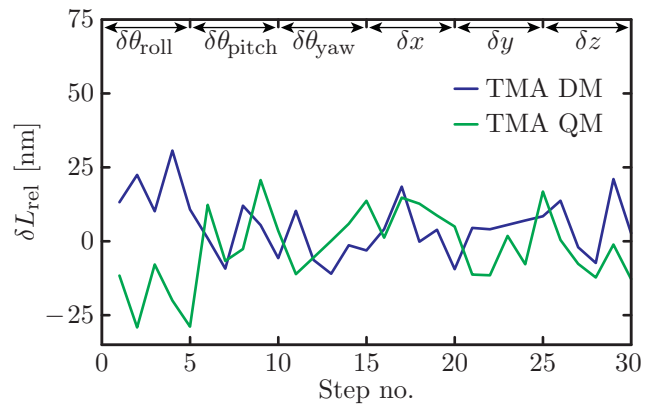


Table 4.2: *Residual rotation-to-pathlength coupling of the three investigated TMA units determined from measurements of δL_{rel} incurred under hexapod rotations $\delta\theta_{\text{roll}}$, $\delta\theta_{\text{pitch}}$, $\delta\theta_{\text{yaw}}$. Shown are averaged values and their statistical standard deviations from 20 measurements. All units in $\mu\text{m}/\text{rad}$.*

Item	Roll	Pitch	Yaw
Glass TMA	-11 ± 12	5 ± 5	-2 ± 6
TMA DM	12 ± 8	-1 ± 9	2 ± 10
TMA QM	-10 ± 17	-1 ± 6	-3 ± 8

QM (green line) were obtained equivalently to the final Glass TMA measurement, solid black line in Fig. 4.5, by iteratively measuring, adjusting the BMR position, and minimizing δL_{rel} . In Fig. 4.6, only $N = 5$ steps forth and back for each rotation and translation were performed. As before, the step sizes were $\delta\theta_{\text{roll}} = \delta\theta_{\text{pitch}} = \delta\theta_{\text{yaw}} = 2 \text{ mrad}$, $\delta x = 2 \text{ mm}$, and $\delta y = \delta z = 0.2 \text{ mm}$.

As for the Glass TMA, we can observe a non-vanishing roll coupling for steps 1–5 in Fig. 4.6. For the TMA DM, we observe $20 \text{ nm}/2 \text{ mrad} = 10 \mu\text{m}/\text{rad}$ and for the TMA QM, the roll coupling is $-20 \text{ nm}/2 \text{ mrad} = -10 \mu\text{m}/\text{rad}$.

After properly positioning the BMR at the TMA PMC, the measurement of δL_{rel} under rotations $\delta\theta_{\text{roll}}$, $\delta\theta_{\text{pitch}}$, $\delta\theta_{\text{yaw}}$ was repeated with a larger number of steps to further improve statistics. By averaging over 20 steps for each TMA and each rotation, the residual rotation-to-pathlength coupling for the TMAs was determined. The results are summarized in Tab. 4.2.

4.2.3 Measuring TMA vertex and BMR position with CMM

Now that the BMR physically marks the TMA PMC position, the carbon fiber breadboard hosting both TMA and BMR is transferred to the CMM (cf. Chap. 3.2.2.2). For the Glass TMA, the pre-alignment step in the CMM (cf. Sec. 4.2.1) has not been performed. Therefore, prior to deinstallation, two position-sensitive QPDs mounted on the carbon fiber breadboard are centered in the BMR beam in a similar way as shown in Fig. 3.17, so that they reference the interferometric measurement axis.

For the Glass TMA, once installed on the CMM table, an auxiliary beam was centered on the two position-sensitive QPDs which had been installed on the carbon fiber breadboard. The auxiliary beam axis was then measured with CABAM. The alignment error between this beam axis and the x -axis of the CMM coordinate system as defined by the TMA coordinate system, cf. Chap. 2.1.2, introduces an additional error in PMC location, since the PMC^x error couples into the measurement of PMC^y

and PMC^z (cf. Chap. 3.2.3). A coalignment error of less than 12 mrad was measured. With an anticipated PMC^x uncertainty of ± 1 mm (cf. Sec. 4.2.2), this leads to an extra $\text{PMC}^{y,z}$ uncertainty of ± 12 μm , which agrees well with the estimation in Chap. 3.2.3.

Consecutively, the TMA mirror planes and the BMR position were measured. Each TMA mirror was probed with 30 points evenly distributed around the coated reflective area. The maximum separation between measurement points was at least 4 cm for each TMA mirror. Touching the coated areas of the mirrors was avoided to prevent any damage. The BMR sphere was also probed with 30 points. The entire probing sequence was programmed in CMM script language and performed three times in automatic CNC mode.

The vertex position of each TMA unit was calculated as the intersection point of planes fitted to the points probed on the TMA mirrors. The TMA vertex positions are summarized along with the BMR center positions in Tab. 4.3. The values shown are averaged over the three CMM measurement iterations with a statistical standard deviation of 1 μm . Additionally, for BMR position measurements, we expect CMM systematic errors of ± 2 μm . As estimated in Chap. 3.2.3, CMM systematic errors are expected to lead to an uncertainty in the TMA vertex position of ± 26 μm , since the vertex position is extrapolated from CMM measurements of the TMA mirrors.

For the Glass TMA, TMA vertex and BMR center position were within ± 1 mm in the roll-axis x and ± 50 μm in the pitch and yaw axes, y and z respectively. For the TMA DM and the TMA QM, TMA vertex and BMR coincided within ± 25 μm in each axis, which can be attributed to the improved test procedure.

4.2.4 Measuring TMA dihedral angles and beam coalignment with CMM

Now the procedures from Chap. 3.2.2.3 are performed. From the CMM measurement of the TMA mirror planes, we can determine the dihedral angle deviations from $\pi/2$ of the TMA mirrors (cf. Chap. 1.3), which are listed in Tab. 4.4. The values are averaged over three CMM iterations with a statistical standard deviation of 13 μrad . However, systematic errors might be larger. Following the estimate in Chap. 3.2.3, we expect an angular accuracy of roughly ± 50 μrad , which is derived from the CMM positional accuracy of ± 2 μm divided by the maximum separation of 4 cm between the probed points on the TMA mirrors, cf. Sec. 4.2.3.

The TMA dihedral angle deviation $\gamma_3 = (\angle(\text{M2}, \text{M3}) - \pi/2)$ was zero within the measurement accuracy for all three TMA units. The reason for this is that TMA mirrors M2 and M3 are directly mounted together on the M2/M3 subassembly (cf.

Table 4.3: Vertex position determined from CMM measurements of the TMA mirror planes and position of the center of the BMR sphere in CMM coordinates for the Glass TMA, the TMA DM, and the TMA QM. For the Glass TMA, the whole test procedure was performed twice (“1st run”, “2nd run”). All units in mm.

Item		x	y	z
Glass TMA (1st run)	Vertex	-322.793	318.139	-70.775
	BMR	-321.819	318.122	-70.766
	Difference	0.975	-0.017	0.010
Glass TMA (2nd run)	Vertex	-322.795	318.149	-70.757
	BMR	-321.908	318.199	-70.722
	Difference	0.886	-0.050	0.036
TMA DM	Vertex	-325.745	-44.525	-84.438
	BMR	-325.747	-44.509	-84.430
	Difference	-0.002	0.016	0.008
TMA QM	Vertex	-325.962	-44.674	-84.648
	BMR	-325.961	-44.661	-84.670
	Difference	0.001	0.013	-0.022

Chap. 2.1) so that the angle between them is very well controlled by the perpendicularity of the mirror substrates.

The TMA beam coalignment was measured using CABAM as described in Chap. 3.2.2.3. The measurement was repeated five times for each TMA unit. Note that the beam coalignment measured here is not representative for the performance of the TMA units since this test bed does not support a gravity-compensating installation of the TMA units as in Chap. 3.1. In fact, the whole purpose of this exercise is testing the consistency of the analytical TMA model from Chap. 1.3.

The measured beam coalignment angles for the three TMA units are summarized in Tab. 4.5. The values are averaged over the five measurements leading to a standard deviation of less than $10 \mu\text{rad}$. Furthermore, as we have shown in Chap. 3.2.2.4, CABAM is accurate within $\pm 10 \mu\text{rad}$.

4.2.5 Discussion

We now want to compare the measurement results with the results obtained with the analytical TMA model from Chap. 1.3 when plugging in the TMA dihedral angle deviations as measured in Sec. 4.2.4. We do this for the residual TMA rotation-to-pathlength coupling (cf. Sec. 4.2.2), for the offset between TMA vertex and PMC (cf. Sec. 4.2.3), and for the TMA beam coalignment (cf. Sec. 4.2.4).

Table 4.4: Deviation of dihedral angles from $\pi/2$ for Glass TMA, TMA DM, and TMA QM as measured by probing the TMA mirrors with the CMM. All units are μrad .

Item	γ_1	γ_2	γ_3
Glass TMA	-76	-33	0
TMA DM	-282	-284	0
TMA QM	-67	-12	0

Table 4.5: Beam coalignment of Glass TMA, TMA DM, and TMA QM as measured with CABAM. All units are μrad .

Item	δ_{hor}	δ_{ver}	δ_{RMS}
Glass TMA	-22	-66	70
TMA DM	-757	-6	757
TMA QM	-67	-45	81

4.2.5.1 Residual rotation-to-pathlength coupling of TMA units

As we have seen in Chap. 1.3, for a TMA with non-zero mirror misalignments, rotation-to-pathlength coupling is not vanishing in general anymore by placing the TMA vertex in the center of rotation. However, it can be minimized by rotating around the TMA PMC. We have learned in Chap. 3.2.1 that this is equivalent to the measurement of δL_{rel} in Sec. 4.2.2 after positioning the BMR at the TMA PMC. Now let us compare the measured residual rotation-to-pathlength coupling for the TMA units from Tab. 4.2 with the residual rotation-to-pathlength coupling that we would theoretically expect when plugging the TMA dihedral angle deviations from Tab. 4.4 into Eq. (1.7).

The results are summarized in Tab. 4.6. The rotation-to-pathlength couplings from Tab. 4.2 are values averaged over 20 measurements with standard deviations of less than $17 \mu\text{rad}/\text{rad}$, cf. Sec. 4.2.2. The uncertainty of the rotation-to-pathlength couplings derived from the dihedral angle deviations $\gamma_1, \gamma_2, \gamma_3$ has two contributions: Applying error propagation, the statistical standard deviation of $\gamma_1, \gamma_2, \gamma_3$ of $13 \mu\text{rad}$, cf. Sec. 4.2.4, leads to an uncertainty of $13 \mu\text{m}/\text{rad}$. Furthermore, the estimated systematic error of $\gamma_1, \gamma_2, \gamma_3$ of $\pm 50 \mu\text{rad}$, cf. Sec. 4.2.4, corresponds to an uncertainty of $\pm 51 \mu\text{m}/\text{rad}$ after error propagation.

The measured rotation-to-pathlength couplings and the ones derived from $\gamma_1, \gamma_2, \gamma_3$ show an excellent agreement, with the largest deviation being $8 \mu\text{m}/\text{rad}$. This suggests that the estimate of the systematic error of $\gamma_1, \gamma_2, \gamma_3$ is too high. Furthermore,

Table 4.6: *Residual rotation-to-pathlength coupling of TMA. Shown are the coupling coefficients from Tab. 4.2 measured in Sec. 4.2.2 under hexapod roll, pitch, yaw rotations (averaged over 20 steps) and values calculated with the TMA dihedral angle deviations $\gamma_1, \gamma_2, \gamma_3$ by using the analytical TMA model, Eq. (1.7). All units in $\mu\text{m}/\text{rad}$.*

Item	Roll	Pitch	Yaw
Glass TMA	-11	5	2
From $\gamma_1, \gamma_2, \gamma_3$	-19	0	0
TMA DM	12	-1	-2
From $\gamma_1, \gamma_2, \gamma_3$	20	0	0
TMA QM	-10	-1	3
From $\gamma_1, \gamma_2, \gamma_3$	-14	0	0

the results confirm that all coupling coefficients are below $20 \mu\text{m}/\text{rad}$.

4.2.5.2 Offset between TMA vertex and PMC position

We calculate the expected offsets of TMA vertex and PMC position with Eq. (1.6) by plugging in the TMA dihedral angle deviations $\gamma_1, \gamma_2, \gamma_3$ from Tab. 4.4. The results are displayed in Tab. 4.7 along with the TMA vertex-to-PMC offsets as obtained from the BMR position (cf. Tab. 4.3).

The TMA vertex-to-PMC offsets as determined from the BMR position show a standard deviation of $1 \mu\text{m}$, as we have seen in Sec. 4.2.3. Furthermore, the systematic error of the whole measurement procedure of positioning the BMR at the TMA PMC (Sec. 4.2.2) and subsequently comparing TMA vertex and BMR position (Sec. 4.2.3) has been estimated in Chap. 3.2.3. For the Glass TMA, we have obtained an uncertainty estimate of $\pm 1 \text{ mm}$ along the x -axis and of $\pm 51 \mu\text{m}$ along y and z . For the TMA DM and the TMA QM, our estimation yields an uncertainty of $\pm 35 \mu\text{m}$ along the x -axis (cf. Sec. 4.2.1) and $\pm 36 \mu\text{m}$ along y and z (cf. Chap. 3.2.3).

The uncertainty of the TMA vertex-to-PMC offset derived from the dihedral angle deviations $\gamma_1, \gamma_2, \gamma_3$ has two contributions: By error propagation, the statistical standard deviation of $\gamma_1, \gamma_2, \gamma_3$ of $13 \mu\text{rad}$, cf. Sec. 4.2.4, leads to an uncertainty of $7 \mu\text{m}$. Furthermore, the estimated systematic error of $\gamma_1, \gamma_2, \gamma_3$ of $\pm 50 \mu\text{rad}$, cf. Sec. 4.2.4, corresponds to an uncertainty of $\pm 26 \mu\text{m}$ after error propagation.

As we can see, within the measurement uncertainties, both deductions of TMA vertex and PMC difference agree. Furthermore, the TMA PMC test bed is precise enough to confirm that TMA vertex and PMC are colocated within the requirements of $\pm 100 \mu\text{m}$.

Table 4.7: Differences δx_{PMC} , δy_{PMC} , δz_{PMC} between TMA vertex and PMC along the roll, pitch, and yaw axes, respectively, as determined from CMM measurements of the TMA mirror planes and the BMR sphere. Furthermore, δx_{PMC} , δy_{PMC} , δz_{PMC} as calculated with Eq. (1.6) from the TMA dihedral angle deviations γ_1 , γ_2 , γ_3 are given. All units are μm .

Item	δx_{PMC}	δy_{PMC}	δz_{PMC}
Glass TMA (1st run)	975	-17	10
Glass TMA (2nd run)	886	-50	36
From $\gamma_1, \gamma_2, \gamma_3$	0	-1	11
TMA DM	2	16	-2
From $\gamma_1, \gamma_2, \gamma_3$	0	0	0
TMA QM	1	13	-22
From $\gamma_1, \gamma_2, \gamma_3$	0	-1	8

The TMA vertex-to-PMC offsets as derived from γ_1 , γ_2 , γ_3 are close to zero with the biggest deviation being 11 μm . As this comes close to the estimation in Chap. 1.3.3.2, this might suggest that the estimated uncertainty of $\pm 26 \mu\text{m}$ is too large. As we have also seen in Sec. 4.2.5.1, this would mean that the uncertainty of $\pm 50 \mu\text{rad}$ for γ_1 , γ_2 , γ_3 overestimates the effect of systematic CMM errors.

4.2.5.3 TMA beam coalignment

We now calculate TMA beam coalignment using the TMA dihedral angle deviations from Tab. 4.4 and Eq. (1.4). In Tab. 4.8, the calculation results are compared with the TMA beam coalignment measured with CABAM in Sec. 4.2.4.

The measurement accuracy of CABAM has been shown to be $\pm 10 \mu\text{rad}$, cf. Sec. 3.2.2.4. For the results obtained from the dihedral angle deviations γ_1 , γ_2 , γ_3 , we find again two uncertainty contributions: The statistical standard deviation of γ_1 , γ_2 , γ_3 of 13 μrad , cf. Sec. 4.2.4, is error-propagated and leads to an uncertainty of 40 μrad . Furthermore, the estimated systematic error of γ_1 , γ_2 , γ_3 of $\pm 50 \mu\text{rad}$, cf. Sec. 4.2.4, corresponds to an uncertainty of $\pm 142 \mu\text{rad}$ after error propagation. This error estimation already shows that the derivation of TMA beam coalignment from CMM measurements of γ_1 , γ_2 , γ_3 is by far not accurate enough.

Both coalignment results obtained from CABAM measurements and derived from γ_1 , γ_2 , γ_3 agree within the measurement uncertainty. The deduction from the dihedral angle deviations seems to generally overestimate the TMA beam coalignment error. The biggest difference between the CABAM results and the deduction from the dihedral angle deviations can be found for the Glass TMA: The horizontal beam

Table 4.8: *Beam coalignment of Glass TMA, TMA DM, and TMA QM as measured with CABAM and as derived with Eq. (1.4) by plugging in the TMA dihedral angle deviations $\gamma_1, \gamma_2, \gamma_3$ which have been measured by probing the TMA mirrors with the CMM. All units are μrad .*

Item	Measurement	δ_{hor}	δ_{ver}	δ_{RMS}
Glass TMA	CABAM	-22	-66	70
	$\gamma_1, \gamma_2, \gamma_3$	-113	-73	134
TMA DM	CABAM	-757	-6	757
	$\gamma_1, \gamma_2, \gamma_3$	-800	2	800
TMA QM	CABAM	-67	-45	81
	$\gamma_1, \gamma_2, \gamma_3$	-111	-55	124

coalignment error δ_{hor} differs by 91 μrad , while the root-mean-square beam coalignment error δ_{RMS} still differs by 64 μrad . This shows that a CMM measurement of the TMA mirrors is not suitable to characterize the TMA beam coalignment sufficiently well within the required $\pm 10 \mu\text{rad}$. Instead, a dedicated coalignment measurement, e.g., as detailed in Chap. 3.1 and in Sec. 4.1, or with a suitable test bed using CABAM, has to be performed.

However, the deviations between CABAM measurements and the derivation using $\gamma_1, \gamma_2, \gamma_3$ are still significantly smaller than the estimated uncertainty of $\pm 142 \mu\text{rad}$. As already noted in Secs. 4.2.5.1 and 4.2.5.2, this might suggest that the estimated uncertainty of $\pm 50 \mu\text{rad}$ (cf. Sec. 4.2.4) for the CMM measurement of $\gamma_1, \gamma_2, \gamma_3$ is too large.

4.2.6 Conclusion

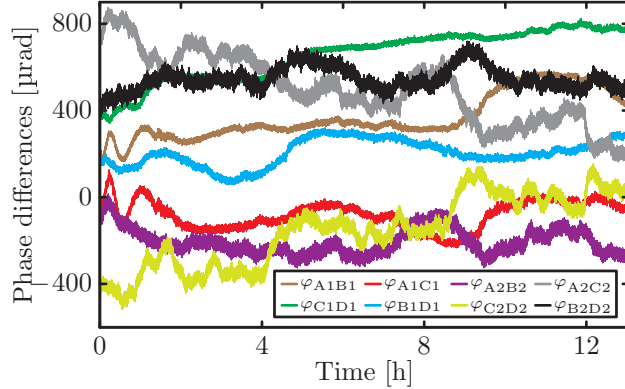
For three different TMA units, positional offsets between TMA vertex and TMA PMC have been measured with a measurement uncertainty of $\pm 51 \mu\text{m}$. The results have confirmed that TMA vertex and PMC coincide within the requirements of $\pm 100 \mu\text{m}$. Furthermore, the investigations have shown that by rotating around the TMA PMC, coupling coefficients for all rotation axes are below 20 $\mu\text{m}/\text{rad}$.

Additionally, good agreement between the measurement results and results obtained from the analytical TMA model (cf. Chap. 1.3) using the TMA dihedral angle deviations was shown for TMA rotation-to-pathlength coupling and TMA vertex-to-PMC offsets. This means that in future studies, a measurement of the TMA dihedral angles is sufficient to characterize these TMA properties.

The TMA beam coalignment can be coarsely determined from the TMA dihedral angle deviations as well. However, the TMA beam coalignment as calculated from

the dihedral angle deviations was too high for all three TMAs by as much as $91\ \mu\text{rad}$, which means that this is not a suitable method to characterize TMA beam coalignment. Instead, dedicated TMA beam coalignment tests have to be performed, as demonstrated in Sec. 4.1.

Figure 4.7: Time series of phase differences between segments of QPD1 and QPD2 (cf. Eq. (3.13)) as measured with an amplitude-modulated laser beam. Phase offsets between QPD segments have already been subtracted in the phasemeter processing chain.



4.3 OBBM test results

In this section, the test results for the OBBM (cf. Chap. 2.2) test campaign obtained with the LRI Optical Bench test bed (cf. Chap. 3.3, Fig. 3.20) are presented. The test results have also been summarized in a project internal technical note [115] and in a related publication [108].

4.3.1 Calibration of QPD phase offsets

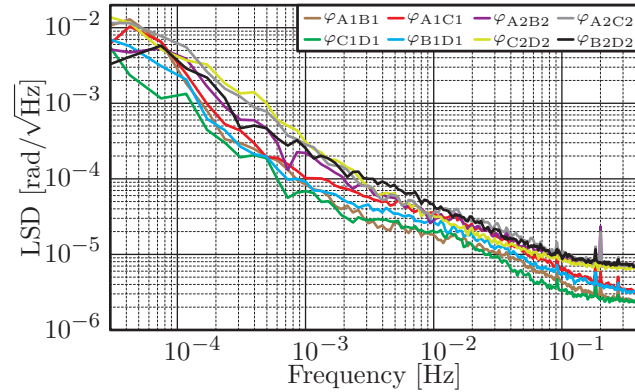
Electronic phase offsets between the segments of both OBBM QPD (QPD1) and QPD2 were calibrated in the LRI Optical Bench test bed (Fig. 3.20) by amplitude-modulating the LO beam, while the RX beam was being blocked. Phase offsets were determined to below ± 1 mrad and subtracted in the phasemeter processing chain. With the anticipated DWS transfer matrix from Eq. (3.14), this corresponds to an electronically caused offset of DWS-measured geometric wavefront tilt of below 0.1 μ rad, which is negligible.

Consecutively, under ambient conditions, a phase offset stability of less than 100 μ rad/ $\sqrt{\text{Hz}}$ was verified in the GRACE Follow-On measurement frequency band of 0.002...0.1 Hz by recording phase differences between the QPD segments. Time series and linear spectral density (LSD, [56]) of the measurement are shown in Figs. 4.7 and 4.8, respectively.

4.3.2 Beamwalk on QPDs

The OBBM telescope is supposed to suppress beamwalk caused by local spacecraft rotation and, in closed-loop beam steering, corresponding steering mirror tilts (cf. Chap. 2.2.1). This suppression of beamwalk is achieved by positioning the OBBM

Figure 4.8: *Linear spectral density (LSD, [56]) of phase differences between segments of QPD1 and QPD2 (cf. Eq. (3.13)) as measured with an amplitude-modulated laser beam.*



QPD (QPD1 in Fig. 3.20) in the image plane of the OBBM telescope to which both steering mirror surface and aperture plane are imaged. According to the telescope properties, Eq. (2.1), steering mirror tilts and tilts in the aperture plane are transformed into pure tilts in this image plane.

This section describes how QPD1 was positioned in the image plane of telescope T1 and, consecutively, how the remaining rotation-to-beamwalk coupling was measured. Rotation-to-beamwalk coupling was recorded for both steering mirror rotations and hexapod rotations to verify the suppression of beamwalk for the steering mirror plane and the aperture plane.

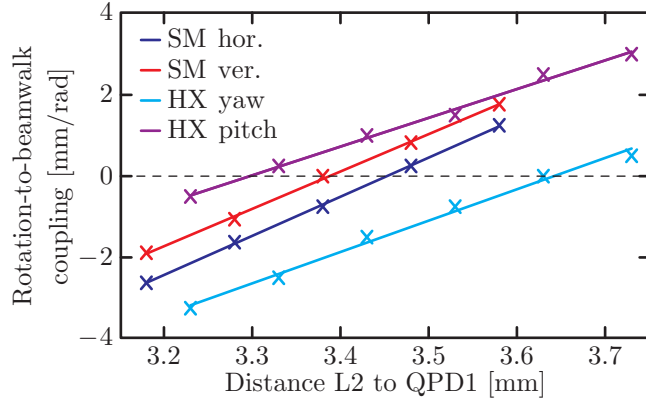
In the course of the measurements, QPD1 was translated along the beam direction. For each position along the beam, QPD1 was centered in the beam by zeroing the DPS signals. Then both horizontal and vertical steering mirror tilts and hexapod rotations (yaw and pitch) of ± 2 mrad were performed upon which QPD1 was re-centered in the beam. Horizontal and vertical beamwalk could be inferred from the scale of the micrometer screws on the QPD1 translation stages.

The measurement results are shown in Fig. 4.9 (crosses). Rotation-to-beamwalk coupling in units of mm/rad is plotted against the distance of QPD1 from lens L2 of the OBBM telescope (cf. Fig. 2.4). The nominal distance of the image plane from L2 obtained from the telescope simulations in Chap. 2.2.1 is $d_3 = 3.7$ mm. Linear fits (solid lines) to the measured data are also displayed in Fig. 4.9.

We determine the zero-crossing of each fitted line and take the mean value, which is (3.5 ± 0.2) mm. Considering the parameter tolerances of the lenses, the mounts, and the QPD1 housing, which all couple into the distance measurement between L2 and QPD1, this value is remarkably close to the simulated d_3 -value.

Next, QPD1 was positioned to the determined location of minimal rotation-to-beamwalk coupling and consecutively rotation-to-beamwalk coupling was measured

Figure 4.9: *Rotation-to-beamwalk coupling on QPD1 for both horizontal and vertical steering mirror tilts (“SM hor.,” “SM ver.”) and hexapod yaw, pitch rotations (“HX hor.,” “HX ver.”). Crosses: measurement points; solid lines: linear fits.*



for both steering mirror tilts and hexapod rotations, which was below 2 mm/rad, as we already could have expected from Fig. 4.9. Considering realistic local spacecraft rotations during the actual satellite mission of some mrad, this corresponds to beamwalks of below 10 μm , which fulfils the LRI requirements.

Consecutively, QPD2 in the setup in Fig. 3.20 is positioned analogously at the image plane of telescope T2. Again, beamwalk was minimized to below 2 mm/rad.

4.3.3 Transfer function of beam steering loop

For both horizontal and vertical actuation axis, the open-loop transfer function of the beam steering loop was measured with a network analyzer as described in Chaps. 1.4.5 and 3.3.2. I-gain factors of 2^5 , 2^4 , and 2^3 were chosen, as suggested by the simulation results in Chap. 3.3.2. A perturbation generated by the network analyzer was added to the actuation signal coming from the phasemeter and then passed on to the steering mirror electronics.

The measurements are shown in Fig. 4.10 along with the simulation results from Chap. 3.3.2. As one can see, both measurement and simulation results behave very similarly. Simulated and measured curves could be matched almost perfectly by reducing the overall gain in the model by 30%, which is well within the parameter tolerances of the model.

Unity gain frequency f_{UG} and phase margin φ_{UG} calculated from the measurements are compared in Tab. 4.9 to the simulation results from Tab. 3.2. An I-gain of 2^4 is chosen for stable loop operation with unity gain frequency of 81 Hz for the horizontal and 73 Hz for the vertical actuation axis of the beam steering loop and with phase margins of 34° and 40° , respectively.

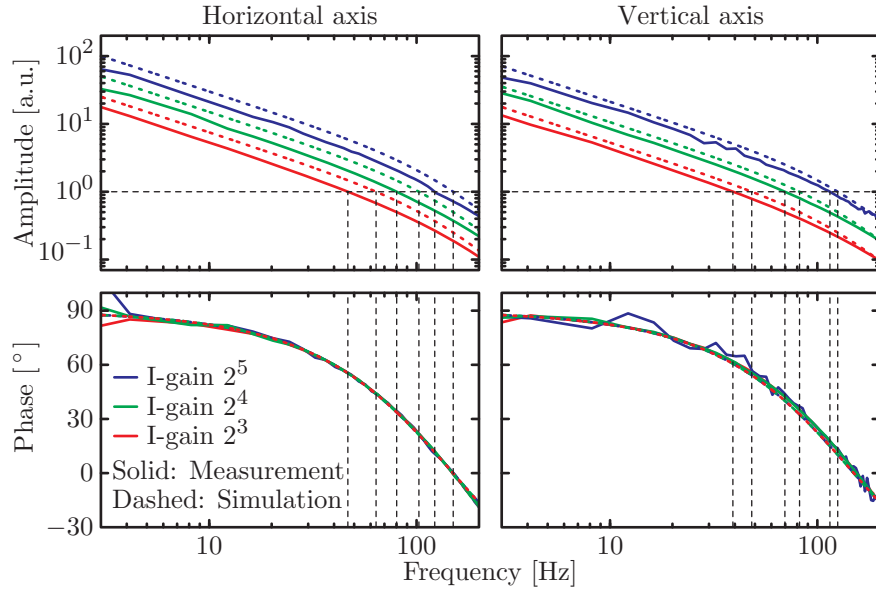


Figure 4.10: Amplitude (top row) and phase (bottom row) of beam steering open-loop transfer function for both horizontal (left column) and vertical (right column) actuation axis. Both measurements (solid lines) and simulations (dashed lines) for three different I -gains are shown.

Table 4.9: Measurement and simulation results (“sim”) of unity gain frequency f_{UG} and phase margin φ_{UG} for three different I -gains and for both the horizontal and the vertical axis of the beam steering loop.

	I -gain	f_{UG} [Hz]	f_{UG}^{sim} [Hz]	φ_{UG} [°]	$\varphi_{UG}^{\text{sim}}$ [°]
Horizontal	2^5	125	150	10	0
	2^4	81	103	34	21
	2^3	49	64	54	44
Vertical	2^5	117	125	16	10
	2^4	73	82	40	33
	2^3	40	48	61	54

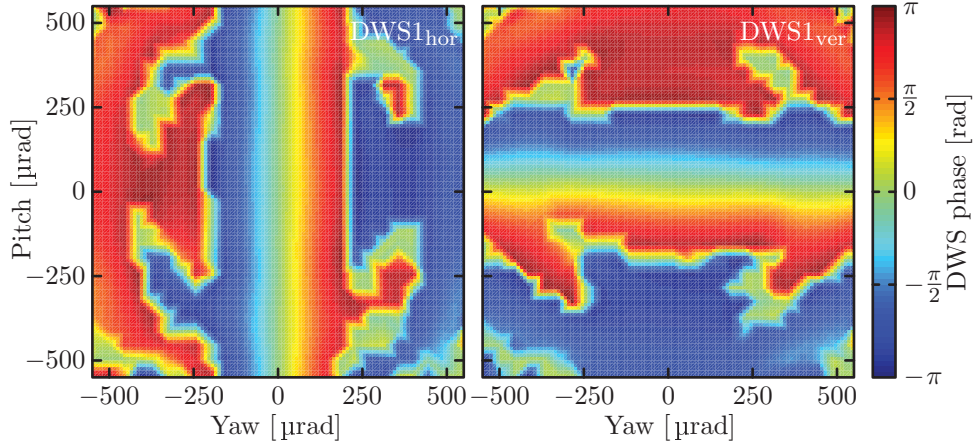


Figure 4.11: *DWS signals of OBBM QPD (QPD1 in Fig. 3.20) as measured during hexapod pitch, yaw rotations. See also [108].*

4.3.4 DWS signals, DWS transfer matrix, and heterodyne efficiency

Hexapod pitch and yaw rotations were performed with open beam steering loop with the steering mirror being fixed at its nominal zero position. Both DWS signals and heterodyne efficiency were measured during the hexapod rotations.

The DWS signals recorded with the OBBM QPD (QPD1 in Fig. 3.20) are shown in Fig. 4.11. The results obtained with QPD2 are very similar and are displayed in Fig. 4.12. When we compare the measurement results with the simulation results from Chap. 3.3.3, Fig. 3.28, we see that they are very much alike: We observe a linear response of horizontal and vertical DWS signals to hexapod yaw and pitch rotations up to about $200 \mu\text{rad}$, then the phase wraps.

Both the simulation and the measurement show a concentric ring structure outside of the linear region, but for the measurement the associated phase fluctuations are much larger and even cross zero. This is not fully understood, but could be caused by the fact that LO beam and RX beam wavefronts are not perfectly flat, cf. Chaps. 2.2.2 and 3.3.1. However, the main region of interest regarding the actual satellite mission is within $\pm 200 \mu\text{rad}$, since for much larger tilt angles, the heterodyne signal amplitude drops below the noise level, cf. Chap. 1.4.3.

The DWS transfer matrices $M1$, $M2$ for QPD1 and QPD2 were determined

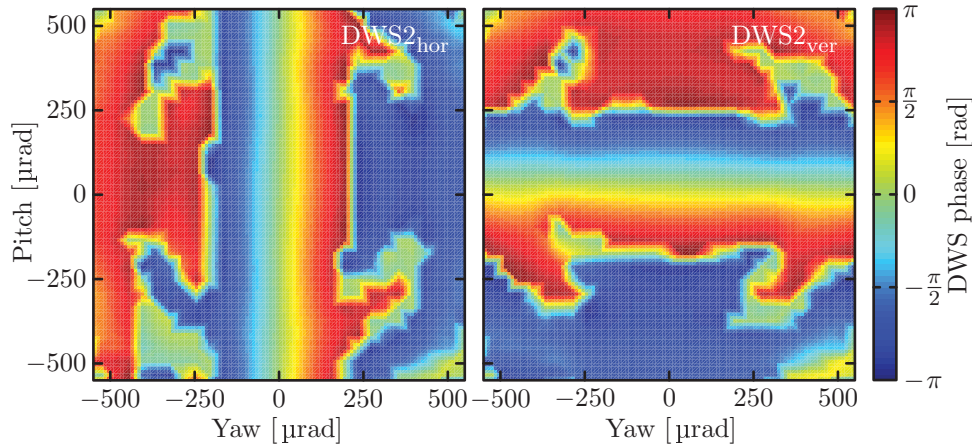


Figure 4.12: *DWS signals of QPD2 (cf. Fig. 3.20) as measured during hexapod pitch, yaw rotations.*

according to Eq. (1.14) inside the linear region for small hexapod rotations:

$$\begin{aligned}
 M1 &= \begin{pmatrix} 16,000 & -200 \\ -300 & -18,000 \end{pmatrix} \cdot 1 \text{ rad/rad}, \\
 M2 &= \begin{pmatrix} 16,400 & -100 \\ 100 & -16,000 \end{pmatrix} \cdot 1 \text{ rad/rad}.
 \end{aligned} \tag{4.1}$$

The off-diagonal matrix elements of $M1$, $M2$ are by a factor of 100 smaller than the diagonal elements, which proves that hexapod coordinates (see Fig. 3.20) and DWS/QPD axes are well aligned within less than $\pm 2^\circ$. The diagonal elements are slightly larger than the simulation predicts in Eq. (3.14). The entry $M1_{22}$ exhibits the largest deviation, being 1.15 times larger than the simulated value. Yet this is still within the expected parameter tolerances.

The heterodyne efficiency between LO beam and RX beam as measured during hexapod pitch and yaw rotations for each segment of the OBBM QPD is shown in Fig. 4.13. Taking the maximum heterodyne efficiency of each segment and then averaging yields $(58 \pm 6)\%$, which agrees very well with the simulation result of 60% (cf. Eq. (3.15)).

While in the simulation result in Fig. 3.29 the maximum heterodyne efficiency is achieved for perfectly aligned LO beam and RX beam, the maximum is offset by as much as $\pm 45 \mu\text{rad}$ in the measurements in Fig. 4.13. This effect can be explained by including curved instead of flat wavefronts in the simulations with a wavefront curvature difference between LO beam and RX beam of $0.01/\text{m}$, which is well within the

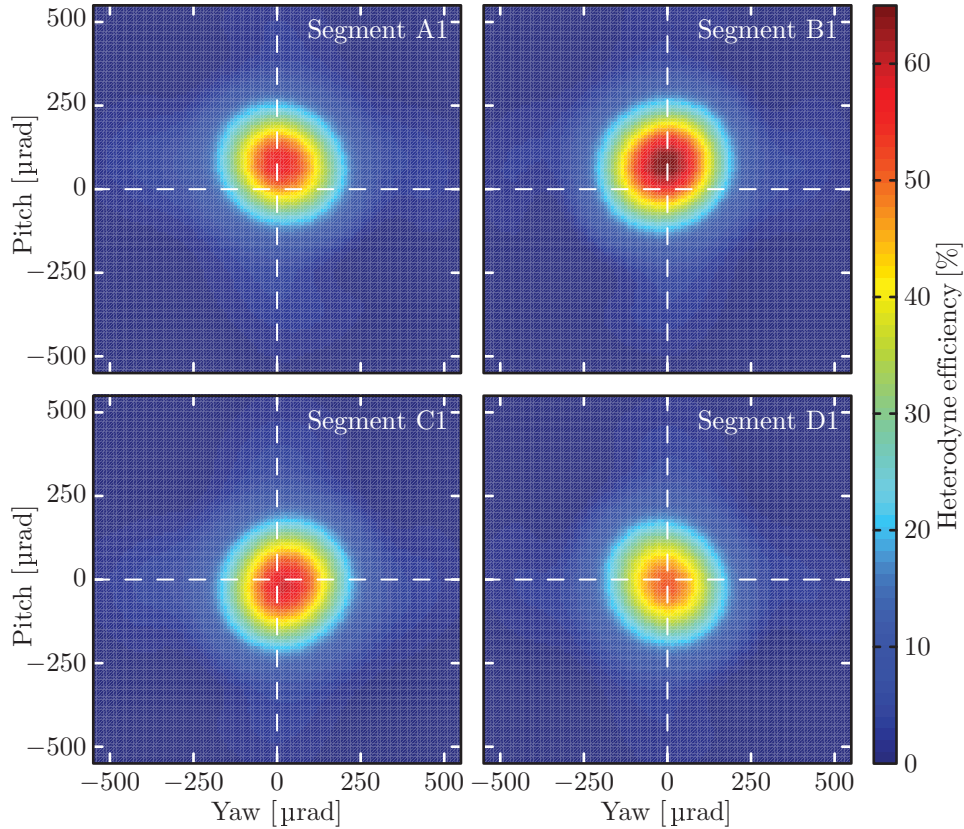


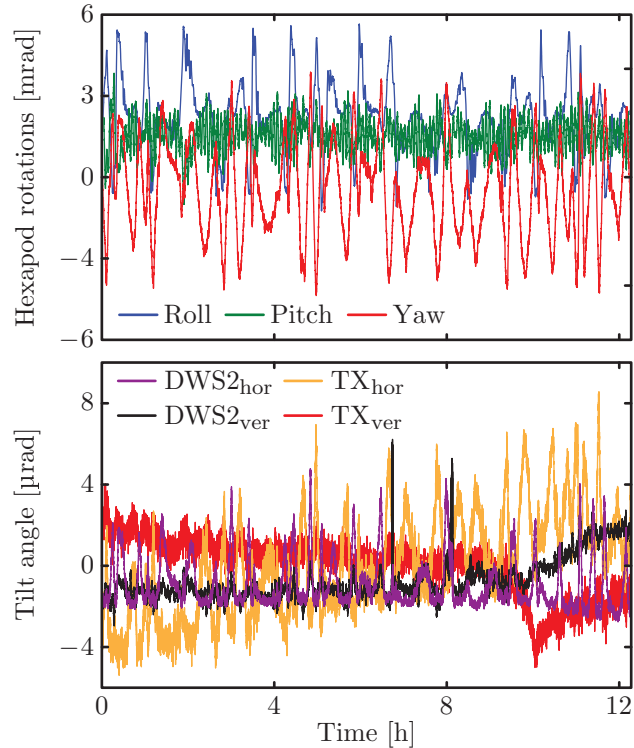
Figure 4.13: *Heterodyne efficiency as measured on the four segments of the OBBM QPD (QPD1 in Fig. 3.20) during hexapod pitch and yaw rotations. See also [108].*

alignment tolerances of LO beam generator and RX beam generator, cf. Chaps. 2.2.2 and 3.3.1.

4.3.5 Coalignment of LO beam and RX beam

The coalignment of LO beam/TX beam and RX beam was measured with the setup in Fig. 3.20 during closed-loop beam steering, while the hexapod was simulating satellite-like attitude jitter. Since the satellite pointing stability for GRACE Follow-On is expected to be improved compared to GRACE, a satellite pointing time series from GRACE was used as a “worst case” estimate to command the hexapod. Satellite line-of-sight pointing angles roll, pitch, yaw were derived from GRACE Level-1B RL02 data (raw data available at [55,57]) for a 12 h time series of January 1, 2008 [116] and

Figure 4.14: *Top: The hexapod is commanded to move according to a GRACE satellite attitude jitter dataset, while the beam steering loop is closed. Bottom: Coalignment of LO beam/TX beam and RX beam as measured with DWS signals of QPD2 (DWS2), converted into geometric wavefront tilt with DWS transfer matrix $M2$ from Eq. (4.1). Orientation changes of the TX beam, $TX_{\text{hor,ver}}$, as recorded with QPD3, QPD4 are also displayed. See also [108].*



interpolated from 0.2 Hz to 1 Hz.¹

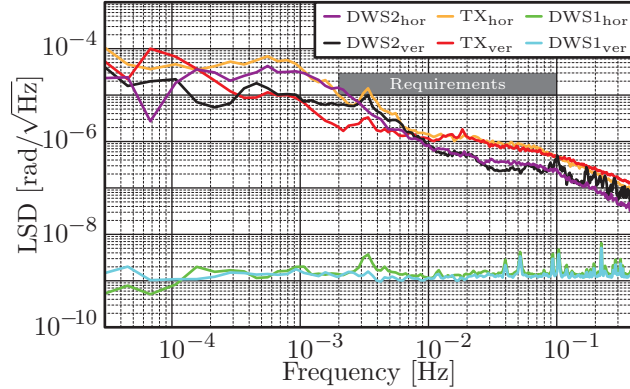
The rotations as commanded to the hexapod during the measurement are shown in Fig. 4.14 (top). The nominal rotation pivot was set to be at the center of the OBBM aperture to avoid shifting the aperture transversally with respect to the RX beam.

The time series of horizontal and vertical beam coalignment between LO beam/TX beam and RX beam as obtained from the DWS signals of QPD2, DWS2_{hor} and DWS2_{ver} respectively, are displayed in Fig. 4.14 (bottom), the linear spectral density (LSD, [56]) in Fig. 4.15. The DWS phases have been converted to relative geometric wavefront tilts between LO beam and RX beam with the DWS transfer matrix $M2$ from Eq. (4.1).

From the measurements, we find an LO beam/TX beam and RX beam coalignment of better than $\pm 10 \mu\text{rad}$ with a stability of below $10 \mu\text{rad}/\sqrt{\text{Hz}}$ in the GRACE Follow-On frequency band of 0.002 Hz...0.1 Hz. This requirement, which is shown as a grey bar in Fig. 4.15, is only marginally crossed by the horizontal beam coalignment DWS2_{hor} between 0.002...0.0024 Hz by less than $5 \mu\text{rad}/\sqrt{\text{Hz}}$.

¹Roll, pitch, yaw time series was kindly prepared by Tamara Bandikova (IfE, Universität Hannover).

Figure 4.15: Closed-loop beam coalignment stability under hexapod attitude jitter. See also [108].



However, with a fixed RX beam, a “real” beam coalignment jitter should also manifest as TX beam orientation changes, which are displayed in Fig. 4.15 as well. As we can see, for frequencies between 0.002...0.0024 Hz, the TX beam jitter is below $10 \mu\text{rad}/\sqrt{\text{Hz}}$ for both TX_{hor} and TX_{ver} . Thus we can conclude that the beam coalignment stability requirement is fulfilled down to 0.002 Hz.

Figure 4.14 (bottom) shows the time series of TX beam orientation changes TX_{hor} , TX_{ver} . TX beam orientation changes are smaller than $\pm 10 \mu\text{rad}$ while the hexapod rotates by many mrad. This is a beam jitter suppression of almost three orders of magnitude.

Additionally, Fig. 4.15 also shows the linear spectral density (LSD, [56]) of the in-loop DWS measurements of QPD1, DWS1_{hor} and DWS2_{ver} . Again, the DWS phases have been converted using the DWS transfer matrix $M1$ from Eq. (4.1), leading to relative geometric wavefront tilts between LO beam and RX beam of below $0.01 \mu\text{rad}$. However, this is not a physical coalignment error, since this only demonstrates the in-loop suppression of DWS1 signals.

4.3.6 Rotation-to-pathlength coupling

Rotation-to-pathlength coupling of the OBBM has been investigated with the test bed in Fig. 3.20. While performing hexapod rotations, pathlength changes were recorded as difference between phase changes on QPD1 (coherent sum of all four segments) and phase changes on PD-REF. As before, nominal rotation pivot was the center of the OBBM aperture.

The hexapod has performed yaw rotations of $\pm 2.5 \text{ mrad}$ with closed beam steering loop without and with compensation plate to verify the suppression of the large linear rotation-to-pathlength-coupling term caused by the beam splitter, cf. Chap. 3.3.5. The mounting strategy of the OBBM optics (cf. Chap. 2.2.1) allowed for easy removal

and reinstallation of the compensation plate.

Without compensation plate, the yaw rotation-to-pathlength coupling was found to be 1.6 mm/rad, which agrees well with the expected value of 1.7 mm/rad from Chap. 3.3.5. With the compensation plate inserted, this linear term was suppressed to below the measurement noise level of $\pm 20 \mu\text{m}/\text{rad}$. For roll and pitch rotations, with the compensation plate inserted, it was confirmed as well that linear rotation-to-pathlength coupling factors are below the noise level.

4.3.7 Conclusion

The LRI beam steering method implemented in the OBBM unit has successfully been tested under realistic local spacecraft attitude jitter of many mrad performed by a hexapod. The tests have verified that the LRI beam steering method is capable of maintaining an intersatellite laser interferometer link with beam pointing error of less than $\pm 10 \mu\text{rad}$. Furthermore, a beam pointing stability of $10 \mu\text{rad}/\sqrt{\text{Hz}}$ in the GRACE Follow-On measurement frequency band of 0.002...0.1 Hz was observed.

The OBBM rotation-to-pathlength coupling was investigated. The test results confirm that the linear term caused by the beam splitter is suppressed to below $20 \mu\text{m}/\text{rad}$ by the use of the compensation plate. Furthermore, DWS signals, heterodyne efficiency, and open-loop transfer function of the beam steering loop were characterized and shown to be in good agreement with simulation results.

Chapter 5

Conclusion and outlook

5.1 Conclusion

In this thesis, test environments have been developed to verify the design functionality of the intersatellite Laser Ranging Interferometer (LRI) for the GRACE Follow-On geodesy mission. Two LRI key components have been investigated: the Triple Mirror Assembly (TMA) and the LRI Optical Bench.

The TMA retroreflects the local oscillator (LO) laser beam to send it back to the distant spacecraft. The TMA's key properties are the coalignment of incoming and outgoing beam and a small rotation-to-pathlength coupling under local spacecraft attitude jitter, when the TMA vertex is properly placed at the spacecraft's center of rotation.

The LRI Optical Bench delivers the LO beam, measures both accumulated phase and tilt angle between LO wavefronts and received (RX) wavefronts, and actively coaligns the LO wavefronts with the RX wavefronts using the LRI beam steering method. Via retroreflection by the TMA, this ensures that the LO beam reaches the distant spacecraft even under local spacecraft attitude jitter.

Three test environments have been presented to investigate three of the LRI key properties: the TMA beam coalignment, the TMA rotation-to-pathlength coupling, and the LRI beam steering method. Furthermore, these key properties have been investigated by analysis, simulation, and in test campaigns conducted in the presented test environments.

The TMA beam coalignment was tested in the *TMA beam coalignment test bed* using a large aperture homodyne interferometer and a flat reference bar to extend the aperture of the interferometer to the required size of the TMA. The evaluation procedure was tested with simulated mock-up data and an accuracy of ± 1 μ rad was confirmed for the recovery of the TMA beam coalignment angle. Consecutively, a test

campaign was performed for a prototype TMA. In a gravity-compensating installation, a TMA beam coalignment angle of $9\ \mu\text{rad}$ was verified.

The TMA's behavior under rotation was investigated in the *TMA rotation-to-pathlength coupling test bed*. Test campaigns were performed for a TMA prototype, the TMA Design Model, and the TMA Qualification Model. The TMA point of minimal coupling (PMC) was determined by measuring range displacements under rotations of a hexapod, a six-degree-of-freedom rotation and translation platform.

When rotating around the TMA PMC, the test campaigns have confirmed a TMA rotation-to-pathlength coupling of less than $20\ \mu\text{m}/\text{rad}$ in all three rotation axes roll, pitch, and yaw. Furthermore, the PMC position was compared with the TMA vertex position by measuring the TMA mirror planes with a coordinate measuring machine (CMM). The results show that the TMA vertex and the TMA PMC coincide within the measurement uncertainty of $\pm 51\ \mu\text{m}$. This is compatible with the current baseline in which the TMA vertex position information is used during integration of the TMA into the spacecraft.

Additionally, the test results have been compared with predictions of an analytical TMA model which rely on TMA dihedral angle measurements with a CMM. The results for the TMA rotation-to-pathlength coupling and the TMA PMC-to-vertex offset agree well within the measurement uncertainty. Therefore, these TMA properties can be adequately predicted by measuring the TMA dihedral angles with a CMM.

The LRI beam steering method was studied in the *LRI Optical Bench test bed*. This test environment delivers a simulated "far-field" RX beam to the optical bench unit under test which is placed on a hexapod platform to perform "local spacecraft" attitude jitter.

In this thesis, a representative optical bench breadboard model (OBBM) has been developed and constructed. Test results obtained with this optical bench unit verify that the LRI beam steering method coaligns the LO beam to the RX beam with a beam pointing error of less than $\pm 10\ \mu\text{rad}$ under realistic local spacecraft attitude jitter of many mrad. In the GRACE Follow-On measurement frequency band of $0.002\text{...}0.1\ \text{Hz}$, a beam pointing stability of better than $10\ \mu\text{rad}/\sqrt{\text{Hz}}$ has been demonstrated.

Additionally, the tests have shown that the use of a compensation plate reduces optical bench rotation-to-pathlength coupling to below $20\ \mu\text{m}/\text{rad}$, as predicted by simulation results. Furthermore, differential wavefront sensing signals, heterodyne efficiency, and open-loop transfer function of the beam steering loop have been investigated. The measurement results and the simulation results were in good agreement.

5.1 CONCLUSION

The test environments and test campaigns that have been presented in this thesis have confirmed the design functionality of the TMA and the LRI Optical Bench. Furthermore, the elaborated concepts and procedures have laid a solid foundation for testing LRI flight units, which are currently under production. Moreover, they provide the opportunity to investigate concepts and instruments for future satellite geodesy missions using intersatellite laser interferometry.

5.2 Outlook

The scope of this thesis was the development of test environments with which the TMA and the LRI Optical Bench have been investigated. The test environments are highly specialized since they focus on key properties of the GRACE Follow-On LRI. Furthermore, they have been adopted to host the specific LRI units that have been investigated in this thesis. However, the underlying test procedures that have been elaborated can readily be applied to modified test environments. This has successfully been demonstrated in a test campaign performed with the engineering model of the LRI Optical Bench [87].

The adaptation of the test environments and procedures presented in this thesis can be exploited in three directions: testing of LRI flight hardware, establishing an LRI ground reference setup, and testing for future satellite geodesy missions that use intersatellite laser interferometry. This is briefly discussed in the following subsections.

5.2.1 Testing of LRI flight hardware

Testing of flight hardware is a delicate task which has to be performed by trained personnel. However, the Albert Einstein Institute (AEI) will support LRI flight hardware testing at its best effort. Current plans foresee an implementation of the LRI Optical Bench test bed (cf. Fig. 3.20) on mobile breadboard units. By this, the setup as a whole could be transferred to dedicated test facilities to serve as additional supportive test platform.

5.2.2 The LRI ground reference setup

For LRI tests on spacecraft level, a special tool is being developed, which is called fiber-based optical ground support equipment (Fiber-OGSE, [117]). The Fiber-OGSE uses fiber-coupled acousto-optic modulators (AOMs) to simulate Doppler shifts of the intersatellite laser link due to relative spacecraft motion (cf. Chap. 1.4.3). Additionally, power loss due to diffraction and mispointing of the distant spacecraft can be simulated. The Fiber-OGSE is fully fiber-based to facilitate mounting to the spacecraft.

A modified version of the Fiber-OGSE could be combined with the LRI Optical Bench test bed presented in this thesis (cf. Fig. 3.20) to establish an LRI ground reference setup. The envisioned configuration is shown in Fig. 5.1.

The LRI ground reference setup can be populated with LRI engineering models of phasemeter (PM), optical bench (OB), laser (including frequency stabilization), and TMA. Units that are currently not available could be replaced with AEI hard-

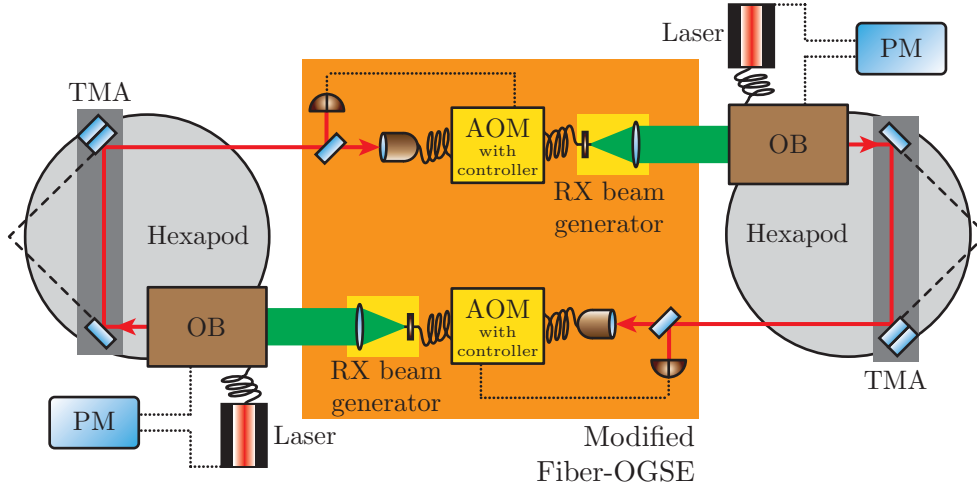


Figure 5.1: The LRI ground reference setup features the full LRI intersatellite laser link. Doppler shifts and power loss are simulated with a modified Fiber-OGSE, spacecraft rotations with two hexapod platforms. All LRI units can be integrated: the phasemeter (PM), the laser including the laser frequency stabilization, the optical bench (OB), and the TMA.

ware, such as AEI phasemeters and the AEI-built optical bench breadboard model (OBBM), and with commercial lasers and retroreflectors. However, the goal is to install components as close as possible to the actual flight units, so that a representative behavior can be expected.

The LRI ground reference setup is capable of simulating the full LRI link: Doppler shifts and power loss are simulated with the modified Fiber-OGSE, while spacecraft rotations are simulated with two hexapod platforms. This enables the LRI ground reference setup to simulate LRI operation on ground during the GRACE Follow-On satellite mission. This allows for on-ground instrument analysis if something unforeseen occurs. Furthermore, mission scenarios such as the initial calibration scan or reacquisition procedures [51, 52, 67, 72] can be tested before being applied to the satellites.

5.2.3 Future satellite geodesy missions with laser interferometers

Although the test environments presented in this thesis have been developed for the specific needs of the LRI, some of the addressed issues are common to a certain group of interferometry space missions. Especially future geodesy missions based on

intersatellite laser ranging will have to face similar challenges regarding spacecraft attitude jitter, resulting rotation-to-pathlength coupling, and the necessity of active beam steering.

So far, investigations have shown that the LRI architecture is uniquely simple for a system that is required to provide closed-loop beam steering. Thus the LRI architecture is considered a promising candidate for future geodesy missions using intersatellite laser interferometry. Since this architecture requires a TMA, it is very likely that LRI-like components of future geodesy missions can be investigated in modified versions of the test environments that have been presented in this thesis.

Appendix

A Six-degree-of-freedom interferometer platform

A six-degree-of-freedom interferometer platform has been designed with which the motion of a test object can be monitored in 3 translational and 3 rotational degrees of freedom. Since the interferometer is implemented on two perpendicular baseplates which form an “L”-shape, it was named “L-shaped interferometer”, in short LINT.

Originally, LINT was intended to monitor erroneous hexapod motion in the TMA rotation-to-pathlength coupling test bed (cf. Chap. 3.2). However, the universality of the concept allows to apply LINT to any application that requires precision measurement of a moving object in six degrees of freedom.

LINT has been developed and simulated with the AEI in-house interferometry software IfoCAD [118–120].¹ The LINT architecture is quite complex due to the required readout of six degrees of freedom. The optical layout as produced with IfoCAD is shown in Fig. A.1 (top).

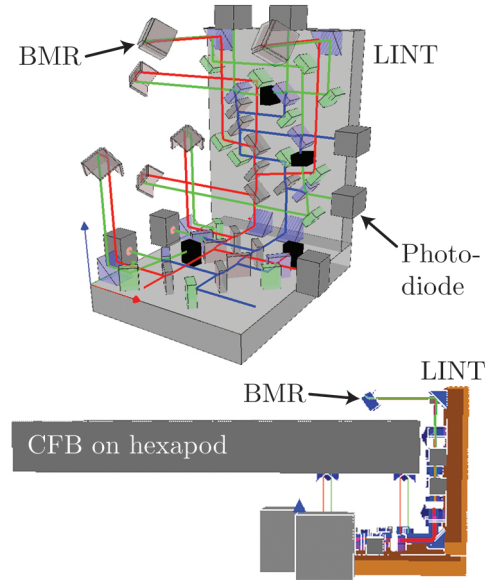
The basic LINT concept is measuring distance changes between the L-platform and six reference points on the test object with heterodyne interferometry. The reference points are constituted by vertices of six ball-mounted retroreflectors (BMR). The BMRs are mounted on a rigid structure which can be measured with a CMM to obtain the relative BMR positions prior to installation on the test object.

LINT supplies six outgoing laser beams (red) with well-defined beam axes, cf. Fig. A.1 (top). The return beams (green) that have been retroreflected by the BMRs are interfered with reference beams (blue) on photodiodes fixed to the LINT platform. Additionally, LINT features readout of beamwalk using differential power sensing (DPS, cf. Sec. 1.4.4) and a reference interferometer to subtract fiber-induced noise.

The implementation of LINT to measure the motion of a carbon fiber breadboard (CFB) installed on a hexapod platform has also been simulated with IfoCAD, see Fig. A.1 (bottom). The six BMRs are installed on the carbon fiber breadboard. First simulation results promise a measurement precision of below 10 nm.

¹IfoCAD simulations of LINT performed by Vitali Müller (AEI).

Figure A.1: The optical layout of LINT as produced with IfoCAD. Top: LINT sends out six laser beams (red) to six ball-mounted retroreflectors (BMR), which serve as reference points. The return beams (green) are interfered with the reference beams (blue) on the photodiodes for the heterodyne interferometric range displacement measurements. Bottom: CFB on hexapod hosts six BMRs so that its motions can be tracked with LINT in six degrees of freedom. Image credit: Vitali Müller (AEI).



The mechanical design of LINT was elaborated with the CAD program Autodesk[®] Inventor[®]. The rigid structure hosting the BMR reference points has not been designed yet.

The current CAD model of LINT is shown in Fig. A.2. The assembly strategy is based on template-assisted glueing [121, 122]. Since LINT is intended to monitor relative motion over rather small time periods of some minutes, no high-stability assembly is required, so that no advanced bonding techniques [123] need to be applied.

The two parts of the “L” can be assembled separately and then combined to form the whole LINT platform. As LINT was originally designed to measure erroneous motions of the hexapod platform in the TMA rotation-to-pathlength coupling test bed (cf. Chap. 3.2), the configuration of LINT and hexapod hosting carbon fiber breadboard and TMA is shown in Fig. A.3. The rigid structure hosting the BMR reference points would have to be installed on the carbon fiber breadboard as well.

All LINT baseplate parts have been manufactured from aluminum at the AEI mechanical workshop. The templates have been fabricated from brass (see Fig. A.4), as this allows for higher drill hole accuracy to place the 1 mm diameter steel balls. The steel balls serve as mechanical stops for the optical components during glueing.

The “horizontal” LINT baseplate has successfully been assembled using template 1, see Fig. A.4. However, when placing the recombination beam splitters, the interferometric beatnote could not be sufficiently maximized without vertical adjustment of the beam splitters. The reason for this is partly the aluminum baseplate,

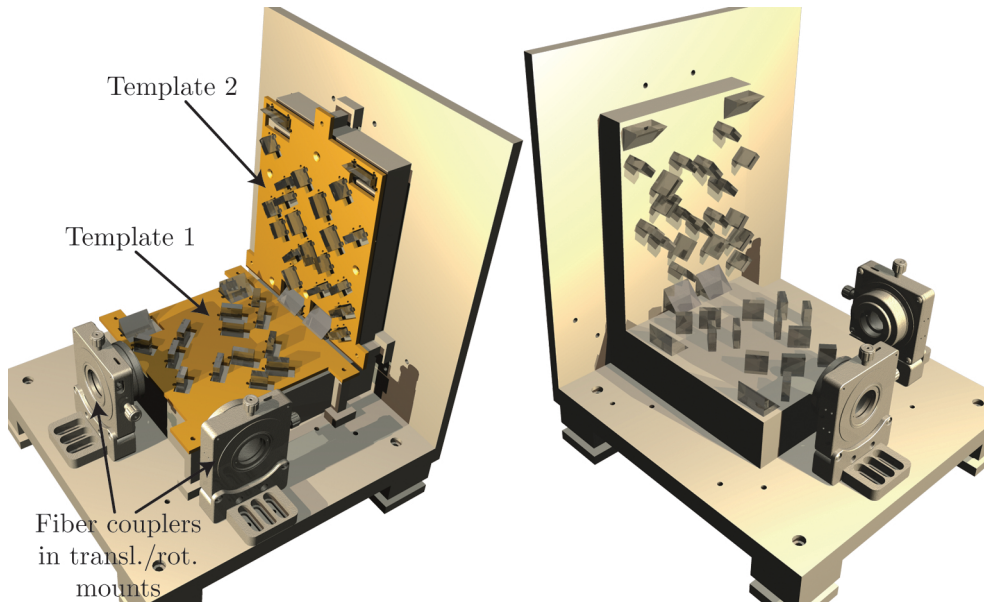
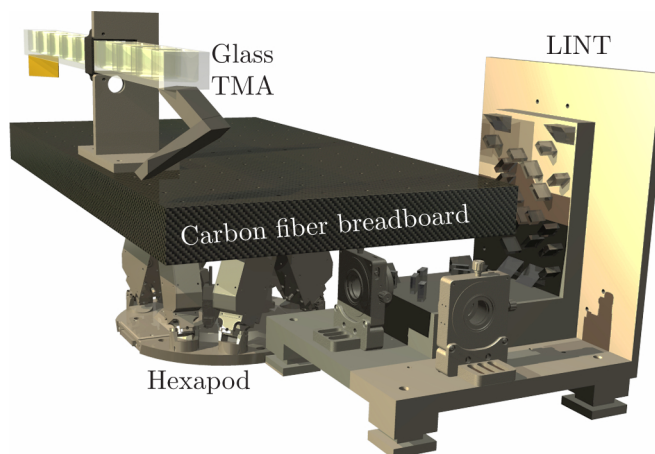


Figure A.2: CAD model of LINT interferometer. Left: Templates for placement of optical components are installed. Right: LINT after glueing optical components. CAD file of translation stages provided by Newport Corp..

Figure A.3: Configuration of LINT and hexapod hosting carbon fiber breadboard with TMA. LINT can monitor erroneous hexapod motions by measuring distance changes to six BMR reference points (not shown) that would have to be installed on the carbon fiber breadboard. CAD file of translation stages provided by Newport Corp., CAD file of hexapod by PI GmbH & Co. KG.



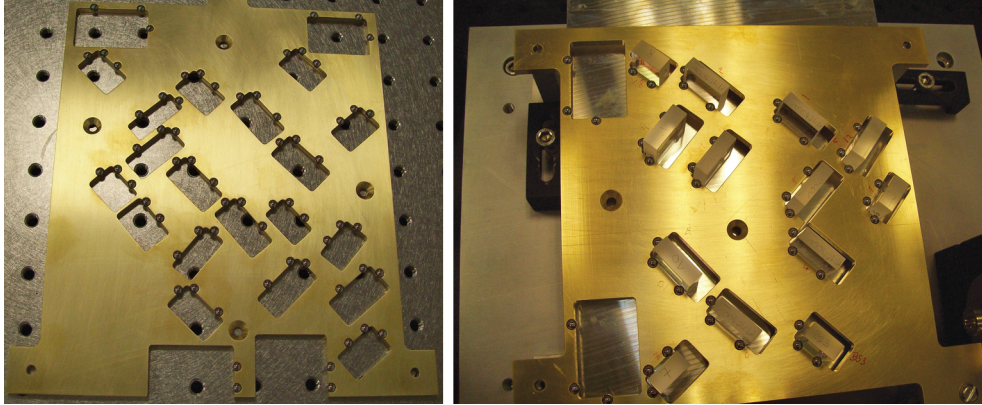


Figure A.4: *Left: LINT template 2. Right: LINT template 1. The components (except recombination beam splitters) are being glued.*

which does not offer the same planarity as Zerodur[®] baseplates which are commonly used for template-bonding of high-precision interferometers. The other reason is that the residual wedge of the components accumulates during the beam path in the assembly.

A solution for the vertical alignment of the recombination beam splitters has been developed, which allows for accurate placement of a beam splitter in four degrees of freedom: The component is held by a gallows construction which is fixed to a hexapod platform, see Fig. A.5. The interferometric beatnote can conveniently be maximized by horizontal and vertical hexapod tilts, which offers a range of many mrad and a step size of a few μrad . By using a viscous glue, the gap between component and baseplate that results from the vertical tilt can be filled.

A first test run with the “hexapod gallows” has been performed which was promising, although beatnote reduction due to alignment distortions could be observed during glue hardening. However, with the right choice of glue, the desired alignment of the vertical tilt of the recombination beam splitters can be achieved and maintained during glue hardening.

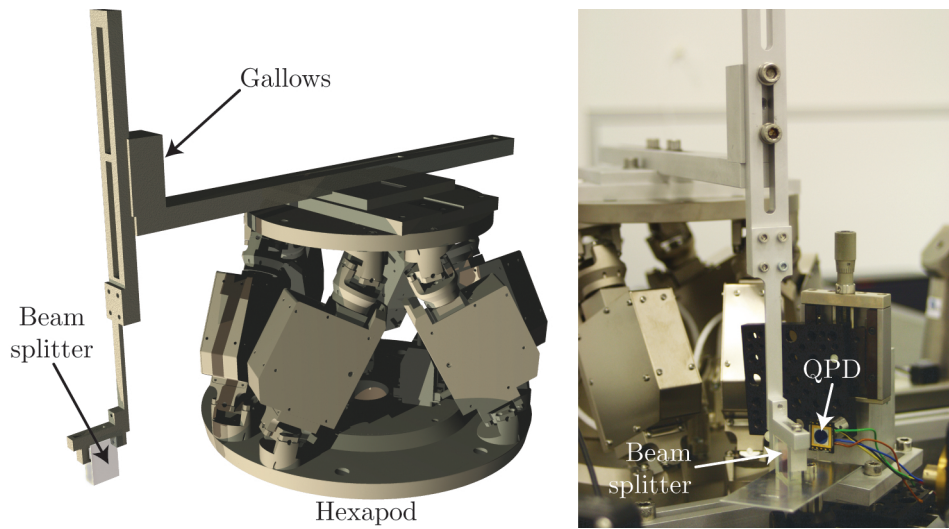


Figure A.5: *Left: Hexapod gallows to place beam splitter in 4 degrees of freedom. CAD file of hexapod provided by PI GmbH & Co. KG. Right: Placement and glueing of beam splitter, while the beatnote is being observed on a photodiode (not shown) and the beam position on a QPD.*

Bibliography

- [1] NASA, “The blue marble,” <http://www.nasa.gov/multimedia/imagegallery>.
- [2] K. Danzmann *et al.*, “The gravitational universe,” European Space Agency (ESA) L2/L3 Science Theme Selection, [arXiv:1305.5720](https://arxiv.org/abs/1305.5720) (2013).
- [3] O. Jennrich, P. Binetruy, M. Colpi, K. Danzmann, P. Jetzer, A. Lobo, G. Nelemans, B. Schutz, T. Stebbins, T. Sumner, S. Vitale, and H. Ward, “NGO – Reveiling a hidden universe: opening a new chapter of discovery,” [European Space Agency \(ESA\) Assessment Study Report](#) (2011).
- [4] K. Danzmann, T. A. Prince, P. Binetruy, P. Bender, S. Buchman, J. Centrella, M. Cerdonio, N. Cornish, M. Cruise, C. J. Cutler, L. S. Finn, J. Gundlach, C. Hogan, J. Hough, S. A. Hughes, O. Jennrich, P. Jetzer, A. Lobo, P. Madau, Y. Mellier, S. Phinney, D. O. Richstone, B. Schutz, R. Stebbins, T. Sumner, K. Thorne, J.-Y. Vinet, and S. Vitale, “LISA – Unveiling a hidden universe,” [European Space Agency \(ESA\) Assessment Study Report](#) (2011).
- [5] O. Jennrich, “LISA technology and instrumentation,” *Class. Quantum Grav.* **26**, 153001 (2009).
- [6] D. A. Shaddock, “Space-based gravitational wave detection with LISA,” *Class. Quantum Grav.* **25**, 114012 (2008).
- [7] G. Heinzel, C. Braxmaier, K. Danzmann, P. Gath, J. Hough, O. Jennrich, U. Johann, A. Rüdiger, M. Sallusti, and H. Schulte, “LISA interferometry: recent developments,” *Class. Quantum Grav.* **23**, 119–124 (2006).
- [8] K. Danzmann and A. Rüdiger, “LISA technology – concept, status, prospects,” *Class. Quantum Grav.* **20**, 1–9 (2003).
- [9] K. Danzmann and the LISA Science Team, “LISA – An ESA cornerstone mission for the detection and observation of gravitational waves,” *Adv. Space Res.* **32**, 1233–1242 (2003).
- [10] S. Barke, N. Brause, I. Bykov, J. J. E. Delgado, A. Enggaard, O. Gerberding, G. Heinzel, J. Kullmann, S. M. Pedersen, and T. Rasmussen, “LISA metrology system – final report,” [European Space Agency \(ESA\) Science Report](#) (2014).
- [11] O. Gerberding, B. Sheard, I. Bykov, J. Kullmann, J. J. E. Delgado, K. Danzmann, and G. Heinzel, “Phasemeter core for intersatellite laser heterodyne interferometry: modelling, simulations and experiments,” *Class. Quantum Grav.* **30**, 235029 (2013).

-
- [12] I. Bykov, J. J. E. Delgado, A. F. G. Marín, G. Heinzel, and K. Danzmann, “LISA phasemeter development: advanced prototyping,” *J. Phys. Conf. Ser.* **154**, 012017 (2009).
- [13] D. Shaddock, B. Ware, P. G. Halverson, R. E. Spero, and B. Klipstein, “Overview of the LISA phasemeter,” *AIP Conf. Proc.* **873**, 654–660 (2006).
- [14] D. I. Robertson, E. D. Fitzsimons, C. J. Killow, M. Perreur-Lloyd, H. Ward, J. Bryant, A. M. Cruise, G. Dixon, D. Hoyland, D. Smith, and J. Bogenstahl, “Construction and testing of the optical bench for LISA Pathfinder,” *Class. Quantum Grav.* **30**, 085006 (2013).
- [15] F. Antonucci, M. Armano, H. Audley, G. Auger, M. Benedetti, P. Binetruy, J. Bogenstahl, D. Bortoluzzi, P. Bosetti, N. Brandt, M. Caleno, P. Cañizares, A. Cavalleri, M. Cesa, M. Chmeissani, A. Conchillo, G. Congedo, I. Cristofolini, M. Cruise, K. Danzmann, F. De Marchi, M. Diaz-Aguilo, I. Diepholz, G. Dixon, R. Dolesi, N. Dunbar, J. Fauste, L. Ferraioli, V. Ferrone, W. Fichter, E. Fitzsimons, M. Freschi, A. García Marín, C. García Marirrodriga, R. Gerndt, L. Gesa, F. Gilbert, D. Giardini, C. Grimani, A. Grynagier, B. Guillaume, F. Guzmán, I. Harrison, G. Heinzel, V. Hernández, M. Hewitson, D. Hollington, J. Hough, D. Hoyland, M. Hueller, J. Huesler, O. Jennrich, P. Jetzer, B. Johlander, N. Karnesis, C. Killow, X. Llamas, I. Lloro, A. Lobo, R. Maarschalkerweerd, S. Madden, D. Mance, I. Mateos, P. W. McNamara, J. Mendes, E. Mitchell, A. Monsky, D. Nicolini, D. Nicolodi, M. Nofrarias, F. Pedersen, M. Perreur-Lloyd, E. Plagnol, P. Prat, G. D. Racca, J. Ramos-Castro, J. Reiche, J. A. R. Perez, D. Robertson, H. Rozemeijer, J. Sanjuan, A. Schleicher, M. Schulte, D. Shaul, L. Stagnaro, S. Strandmoe, F. Steier, T. J. Sumner, A. Taylor, D. Texier, C. Trenkel, H. B. Tu, S. Vitale, G. Wanner, H. Ward, S. Waschke, P. Wass, W. J. Weber, T. Ziegler, and P. Zweifel, “The LISA Pathfinder mission,” *Class. Quantum Grav.* **29**, 124014 (2012).
- [16] H. Audley, K. Danzmann, A. García Marín, G. Heinzel, A. Monsky, M. Nofrarias, F. Steier, D. Gerardi, R. Gerndt, G. Hechenblaikner, U. Johann, P. Luetzow-Wentzky, V. Wand, F. Antonucci, M. Armano, G. Auger, M. Benedetti, P. Binetruy, C. Boatella, J. Bogenstahl, D. Bortoluzzi, P. Bosetti, M. Caleno, A. Cavalleri, M. Cesa, M. Chmeissani, G. Ciani, A. Conchillo, G. Congedo, I. Cristofolini, M. Cruise, F. De Marchi, M. Diaz-Aguilo, I. Diepholz, G. Dixon, R. Dolesi, J. Fauste, L. Ferraioli, D. Fertin, W. Fichter, E. Fitzsimons, M. Freschi, C. García Marirrodriga, L. Gesa, F. Gibert, D. Giardini, C. Grimani, A. Grynagier, B. Guillaume, F. Guzmán, I. Harrison, M. Hewitson, D. Hollington, J. Hough, D. Hoyland, M. Hueller, J. Huesler, O. Jeannin, O. Jennrich, P. Jetzer, B. Johlander, C. Killow, X. Llamas, I. Lloro, A. Lobo, R. Maarschalkerweerd, S. Madden, D. Mance, I. Mateos, P. W. McNamara, J. Mendes, E. Mitchell, D. Nicolini, D. Nicolodi, F. Pedersen, M. Perreur-Lloyd, A. Perreca, E. Plagnol, P. Prat, G. D. Racca, B. Rais, J. Ramos-Castro, J. Reiche, J. A. Romera Perez, D. Robertson, H. Rozemeijer, J. Sanjuan, M. Schulte, D. Shaul, L. Stagnaro, S. Strandmoe, T. J. Sumner, A. Taylor, D. Texier, C. Trenkel, D. Tombolato, S. Vitale, G. Wanner, H. Ward, S. Waschke, P. Wass, W. J. Weber, and P. Zweifel, “The LISA

- Pathfinder interferometry – hardware and system testing,” *Class. Quantum Grav.* **28**, 094003 (2011).
- [17] G. D. Racca and P. W. McNamara, “The LISA Pathfinder mission,” *Space Sci. Rev.* **151**, 159–181 (2010).
- [18] G. Heinzel, V. Wand, A. Garca, O. Jennrich, C. Braxmaier, D. Robertson, K. Middleton, D. Hoyland, A. Rüdiger, R. Schilling, U. Johann, and K. Danzmann, “The LTP interferometer and phasemeter,” *Class. Quantum Grav.* **21**, 581–587 (2004).
- [19] M. Pitkin, S. Reid, S. Rowan, and J. Hough, “Gravitational wave detection by interferometry (ground and space),” *Living Rev. Relativ.* **14** (2011).
- [20] J. R. Gair, M. Vallisneri, S. L. Larson, and J. G. Baker, “Testing general relativity with low-frequency, space-based gravitational-wave detectors,” *Living Rev. Relativ.* **16** (2013).
- [21] B. D. Tapley, S. Bettadpur, M. Watkins, and C. Reigber, “The gravity recovery and climate experiment: mission overview and early results,” *Geophys. Res. Lett.* **31**, L09607 (2004).
- [22] B. D. Tapley, D. P. Chambers, S. Bettadpur, and J. C. Ries, “Large scale ocean circulation from the GRACE GGM01 Geoid,” *Geophys. Res. Lett.* **30**, 2163 (2003).
- [23] B. D. Tapley, S. Bettadpur, M. Cheng, D. Hudson, and G. Kruizinga, “Early results from the gravity recovery and climate experiment,” in *Astrodynamics Specialist Conference*, J. D. Lafontaine, J. DeLafontaine, J. Treder, M. T. Soyka, and J. A. Sims, eds. (Astrodynamics, 2003), 1899–1911.
- [24] B. D. Tapley, S. Bettadpur, J. C. Ries, P. F. Thompson, and M. M. Watkins, “GRACE measurements of mass variability in the Earth system,” *Science* **305**, 503–505 (2004).
- [25] T. Murray, “Climate change: Greenland’s ice on the scales,” *Nature* **443**, 277–278 (2006).
- [26] R. Schmidt, F. Flechtner, U. Meyer, K.-H. Neumayer, Ch. Dahle, R. König, and J. Kusche, “Hydrological signals observed by the GRACE satellites,” *Surv. Geophys.* **29**, 319–334 (2008).
- [27] B. Wouters, D. Chambers, and E. J. O. Schrama, “GRACE observes small-scale mass loss in Greenland,” *Geophys. Res. Lett.* **35**, L20501 (2008).
- [28] V. M. Tiwari, J. Wahr, and S. Swenson, “Dwindling groundwater resources in northern India, from satellite gravity observations,” *Geophys. Res. Lett.* **36**, L18401 (2009).
- [29] V. M. Tiwari, N. Srinivas, and B. Singh, “Hydrological changes and vertical crustal deformation in south india: inference from GRACE, GPS and absolute gravity data,” *Phys. Earth Planet. In.* **231**, 74–80 (2014).

-
- [30] M. van den Broeke, J. Bamber, J. Ettema, E. Rignot, E. Schrama, W. J. van de Berg, E. van Meijgaard, I. Velicogna, and B. Wouters, “Partitioning recent Greenland mass loss,” *Science* **326**, 984–986 (2009).
- [31] J. Wahr, S. Swenson, V. Zlotnicki, and I. Velicogna, “Time-variable gravity from GRACE: first results,” *Geophys. Res. Lett.* **31**, L11501 (2004).
- [32] B. Tapley, J. Ries, S. Bettadpur, D. Chambers, M. Cheng, F. Condi, B. Gunter, Z. Kang, P. Nagel, R. Pastor, T. Pekker, S. Poole, and F. Wang, “GGM02 – An improved Earth gravity field model from GRACE,” *J. Geodesy* **79**, 467–478 (2005).
- [33] W. R. Peltier, “Global glacial isostasy and the surface of the Ice-Age Earth: the ICS-5G (VM2) model and GRACE,” *Annu. Rev. Earth Pl. Sc.* **32**, 111–149 (2004).
- [34] C. Reigber, R. Schmidt, F. Flechtner, R. König, U. Meyer, K. H. Neumayer, P. Schwintzer, and S. Y. Zhu, “An Earth gravity field model complete to degree and order 150 from GRACE: Eigen-GRACE02S,” *Journal of Geodyn.* **39**, 1–10 (2005).
- [35] I. Velicogna, “Increasing rates of ice mass loss from the Greenland and Antarctic ice sheets revealed by GRACE,” *Geophys. Res. Lett.* **36**, L19503 (2009).
- [36] I. Velicogna and J. Wahr, “Time-variable gravity observations of ice sheet mass balance: precision and limitations of the GRACE satellite data,” *Geophys. Res. Lett.* **40**, 3055–3063 (2013).
- [37] A. Paulson, S. Zhong, and J. Wahr, “Inference of mantle viscosity from GRACE and relative sea level data,” *Geophys. J. Int.* **171** 497–508 (2007).
- [38] C. Reigber, H. Luhr, and P. Schwintzer, “CHAMP mission status,” *Adv. Space Res.* **30**, 129–134 (2002).
- [39] R. Pail, S. Bruinsma, F. Migliaccio, C. Forste, H. Goiginger, W. D. Schuh, E. Hock, M. Reguzzoni, J. M. Brockmann, O. Abrikosov, M. Veicherts, T. Fecher, R. Mayrhofer, I. Krasbutter, F. Sanso, and C. C. Tscherning, “First GOCE gravity field models derived by three different approaches,” *J. Geodesy* **85**, 819–843 (2011).
- [40] J. S. Famiglietti, M. Lo, S. L. Ho, J. Bethune, K. J. Anderson, T. H. Syed, S. C. Swenson, C. R. de Linage, and M. Rodell, “Satellites measure recent rates of groundwater depletion in California’s Central Valley,” *Geophys. Res. Lett.* **38**, L03403 (2011).
- [41] C. Dunn, W. Bertiger, Y. Bar-Sever, S. Desai, B. Haines, D. Kuang, G. Franklin, I. Harris, G. Kruizinga, T. Meehan, S. Nandi, D. Nguyen, T. Rogstad, J. B. Thomas, J. Tien, L. Romans, M. Watkins, S. C. Wu, S. Bettadpur, and J. Kim, “Instrument of GRACE: GPS augments gravity measurements,” *GPS World* **14**, 16–28 (2003).

- [42] P. Touboul, E. Willemenot, B. Foulon, and V. Josselin, “Accelerometers for CHAMP, GRACE and GOCE space missions: synergy and evolution,” *B. Geofis. Teor. Appl.* **40**, 321–327 (1999).
- [43] B. S. Sheard, G. Heinzel, K. Danzmann, D. A. Shaddock, W. M. Klipstein, and W. M. Folkner, “Intersatellite laser ranging instrument for the GRACE follow-on mission,” *J. Geodesy* **86**, 1083–1095 (2012).
- [44] S. C. Han, C. Jekeli, and C. K. Shum, “Time-variable aliasing effects of ocean tides, atmosphere, and continental water mass on monthly mean GRACE gravity field,” *J. Geophys. Res.-Sol. Ea.* **109**, B04403 (2004).
- [45] J. Flury, S. Bettadpur, and B. D. Tapley, “Precise accelerometry onboard the GRACE gravity field satellite mission,” *Adv. Space Res.* **42**, 1414–1423 (2008).
- [46] I. Panet, J. Flury, R. Biancale, T. Gruber, J. Johannessen, M. R. van den Broeke, T. van Dam, P. Gegout, C. W. Hughes, G. Ramillien, I. Sasgen, L. Seoane, and M. Thomas, “Earth system mass transport mission (e.motion): A concept for future Earth gravity field measurements from space,” *Surv. Geophys.* **34**, 141–163 (2013).
- [47] B. D. Loomis, R. S. Nerem, and S. B. Luthcke, “Simulation study of a follow-on gravity mission to GRACE,” *J. Geodesy* **86**, 319–335 (2012).
- [48] W. M. Folkner, G. deVine, W. M. Klipstein, K. McKenzie, D. Shaddock, R. Spero, R. Thompson, D. Wuchenich, N. Yu, M. Stephens, J. Leitch, M. Davis, J. deCino, C. Pace, and R. Pierce, “Laser frequency stabilization for GRACE-II,” in *Proceedings of the 2011 Earth Science Technology Forum* (2011).
- [49] R. Thompson, W. M. Folkner, G. deVine, W. M. Klipstein, K. McKenzie, R. Spero, N. Yu, M. Stephens, J. Leitch, R. Pierce, T. T. Y. Lam, and D. A. Shaddock, “A flight-like optical reference cavity for GRACE follow-on laser frequency stabilization,” in *2011 Joint Conference of the IEEE International Frequency Control Symposium/European Frequency and Time Forum Proceedings* (Institute of Electrical and Electronics Engineers, New York, 2011), pp. 729–731.
- [50] R. L. Ward, R. Fleddermann, S. Francis, C. Mow-Lowry, D. Wuchenich, M. Elliot, F. Gilles, M. Herding, K. Nicklaus, J. Brown, J. Burke, S. Dligatch, D. Farrant, K. Green, J. Seckold, M. Blundell, R. Brister, C. Smith, K. Danzmann, G. Heinzel, D. Schütze, B. S. Sheard, W. Klipstein, D. E. McClelland, and D. A. Shaddock, “The design and construction of a prototype lateral-transfer retro-reflector for inter-satellite laser ranging,” *Class. Quantum Grav.* **31**, 095015 (2014).
- [51] D. M. R. Wuchenich, C. Mahrtdt, B. S. Sheard, S. P. Francis, R. E. Spero, J. Miller, C. M. Mow-Lowry, R. L. Ward, W. M. Klipstein, G. Heinzel, K. Danzmann, D. E. McClelland, and D. A. Shaddock, “Laser link acquisition demonstration for the GRACE Follow-On mission,” *Opt. Express* **22**, 11351–11366 (2014).

-
- [52] D. M. R. Wuchenich, “Inter-satellite laser interferometry,” *PhD thesis*, Centre for Gravitational Physics, Australian National University, Acton ACT 0200, Australia (2014).
- [53] D. Schütze, D. Farrant, D. A. Shaddock, B. S. Sheard, G. Heinzel, and K. Danzmann, “Measuring coalignment of retroreflectors with large lateral incoming-outgoing beam offset,” *Rev. Sci. Instrum.* **85**, 035103 (2014).
- [54] D. Schütze, V. Müller, G. Stede, B. S. Sheard, G. Heinzel, K. Danzmann, A. J. Sutton, and D. A. Shaddock, “Retroreflector for GRACE follow-on: Vertex vs. point of minimal coupling,” *Opt. Express* **22**, 9324–9333 (2014).
- [55] National Aeronautics and Space Administration (NASA)/ Jet Propulsion Laboratory (JPL), <http://podaac.jpl.nasa.gov>.
- [56] M. Tröbs and G. Heinzel, “Improved spectrum estimation from digitized time series on a logarithmic frequency axis,” *Measurement* **39**, 120–129 (2006).
- [57] Helmholtz Centre Potsdam – GFZ German Research Centre for Geosciences, <http://isdc.gfz-potsdam.de>.
- [58] J. W. Armstrong, F. B. Estabrook, and M. Tinto, “Time-delay interferometry for space-based gravitational wave searches,” *Astrophys. J.* **527**, 814–826 (1999).
- [59] P. L. Bender, D. G. Currie, R. H. Dicke, D. H. Eckhardt, J. E. Faller, W. M. Kaula, J. D. Mulholland, H. H. Plotkin, S. K. Poultney, E. C. Silverberg, D. T. Wilkinson, J. G. Williams, and C. O. Alley, “Lunar laser ranging experiment,” *Science* **182**, 229–238 (1973).
- [60] C. F. Yoder, J. G. Williams, J. O. Dickey, B. E. Schutz, R. J. Eanes, and B. D. Tapley, “Secular variation of Earths gravitational harmonic J2 coefficient from LA-GEOS and nontidal acceleration of Earth rotation,” *Nature* **303**, 757–762 (1983).
- [61] M. Jeganathan and S. Dubovitsky, “Demonstration of nm-level active metrology for long range interferometric displacement measurements,” in *Interferometry In Optical Astronomy*, P. J. Lena and A. Quirrenbach, eds., *Proc. SPIE* **4006**, 838–846 (2000).
- [62] A. Paolozzi, I. Ciufolini, and C. Vendittozzi, “Engineering and scientific aspects of LARES satellite,” *Acta Astronaut.* **69**, 127–134 (2011).
- [63] G. Renzetti, “First results from LARES: an analysis,” *New Astron.* **23-24**, 63–66 (2013).
- [64] P. R. Yoder, “Study of light deviation errors in triple mirrors and tetrahedral prisms,” *J. Opt. Soc. Am.* **48**, 496–499 (1958).
- [65] V. Müller, “Simulations for LISA & GRACE-Follow-On: Satellite constellations at Lagrangian points for LISA-like missions, interferometer simulations for the GRACE Follow-On mission,” *Master’s thesis*, Max Planck Institute for Gravitational Physics (Albert Einstein Institute) and Institute for Gravitational Physics, Leibniz Universität Hannover, 30167 Hanover, Germany (2013).

- [66] V. Müller, “A note on TMA misalignment for the GRACE Follow-On Laser Ranging Interferometer (GFO LRI),” Technical note, LRI-AEI-TN-006, Max Planck Institute for Gravitational Physics (Albert Einstein Institute) and Institute for Gravitational Physics, Leibniz Universität Hannover, 30167 Hanover (2013).
- [67] C. Mahrtdt, “Laser link acquisition for the GRACE Follow-On Laser Ranging Interferometer,” [PhD thesis](#), Max Planck Institute for Gravitational Physics (Albert Einstein Institute) and Institute for Gravitational Physics, Leibniz Universität Hannover, 30167 Hanover, Germany (2014).
- [68] D. Fink, “Coherent detection signal-to-noise,” *Appl. Opt.* **14**, 689–690 (1975).
- [69] S. C. Cohen, “Heterodyne detection – phase front alignment, beam spot size, and detector uniformity,” *Appl. Opt.* **14**, 1953–1959 (1975).
- [70] J. Salzman and A. Katzir, “Heterodyne detection SNR: calculations with matrix formalism,” *Appl. Opt.* **23**, 1066–1074 (1984).
- [71] C. Mahrtdt, “Contrast and heterodyne efficiency,” Technical note, LRI-AEI-TN-011, Max Planck Institute for Gravitational Physics (Albert Einstein Institute) and Institute for Gravitational Physics, Leibniz Universität Hannover, 30167 Hanover, Germany (2011).
- [72] F. Ales, P. F. Gath, U. Johann, and C. Braxmaier, “Modeling and simulation of a laser ranging interferometer acquisition and guidance algorithm,” *J. Spacecraft Rockets* **51**, 226–238 (2014).
- [73] E. D. Fitzsimons, J. Bogenstahl, J. Hough, C. J. Killow, M. Perreur-Lloyd, D. I. Robertson, and H. Ward, “Precision absolute positional measurement of laser beams,” *Appl. Opt.* **52**, 2527–2530 (2013).
- [74] O. Gerberding, “Phase-readout for intersatellite interferometry,” [PhD thesis](#), Max Planck Institute for Gravitational Physics (Albert Einstein Institute) and Institute for Gravitational Physics, Leibniz Universität Hannover, 30167 Hanover, Germany (2014).
- [75] G. Hechenblaikner, “Measurement of the absolute wavefront curvature radius in a heterodyne interferometer,” *J. Opt. Soc. Am. A* **27**, 2078–2083 (2010).
- [76] T. Schuldt, M. Gohlke, D. Weise, U. Johann, A. Peters, and C. Braxmaier, “Picometer and nanoradian optical heterodyne interferometry for translation and tilt metrology of the LISA gravitational reference sensor,” *Class. Quantum Grav.* **26**, 085008 (2009).
- [77] H. I. Campbell and A. H. Greenaway, “Wavefront sensing: from historical roots to the state-of-the-art,” *EAS Publications* **22**, 165–185 (2006).
- [78] G. Heinzel, A. Rüdiger, R. Schilling, K. Strain, W. Winkler, J. Mizuno, and K. Danzmann, “Automatic beam alignment in the Garching 30-m prototype of a laser-interferometric gravitational wave detector,” *Opt. Commun.* **160**, 321–334 (1999).

-
- [79] E. Morrison, B. J. Meers, D. I. Robertson, and H. Ward, “Automatic alignment of optical interferometers,” *Appl. Opt.* **33**, 5041–5049 (1994).
- [80] D. Z. Anderson, “Alignment of resonant optical cavities,” *Appl. Opt.* **23**, 2944–2949 (1984).
- [81] A. Abramovici and J. Chapsky, *Feedback control systems: a fast guide for scientists and engineers* (Kluwer Academic Publishers, Boston, 2000).
- [82] R. Fleddermann, R. L. Ward, M. Elliot, D. M. Wuchenich, F. Gilles, M. Herding, K. Nicklaus, J. Brown, J. Burke, S. Dligatch, D. I. Farrant, K. L. Green, J. A. Seckold, M. Blundell, R. Brister, C. Smith, B. S. Sheard, G. Heinzl, K. Danzmann, B. Klipstein, D. E. McClelland, and D. A. Shaddock, “Testing the GRACE follow-on triple mirror assembly,” *Class. Quantum Grav.* **31**, 195004 (2014).
- [83] E. J. Elliffe, J. Bogenstahl, A. Deshpande, J. Hough, C. Killow, S. Reid, D. Robertson, S. Rowan, H. Ward, and G. Cagnoli, “Hydroxide-catalysis bonding for stable optical systems for space,” *Class. Quantum Grav.* **22**, 257–267 (2005).
- [84] D. H. Gwo, “Hydroxide-catalyzed bonding,” U.S. patent 6,548,176 B1 (15 April 2003).
- [85] D. H. Gwo, “Ultra-precision and reliable bonding method,” U.S. patent 6,284,085 B1 (4 September 2001).
- [86] D. H. Gwo, “Ultra-precision bonding for cryogenic fused-silica optics,” *Proc. SPIE* **3435**, 136–142 (1998).
- [87] G. Stede, “OBA/OBE/PRF-EM AEI testreport,” Technical note, LRI-AEI-TN-010, Max Planck Institute for Gravitational Physics (Albert Einstein Institute) and Institute for Gravitational Physics, Leibniz Universität Hannover, 30167 Hanover, Germany (2011).
- [88] B. W. Joseph and R. J. Donohue, “Dot patterns from imperfect cube-corner reflectors,” *J. Opt. Soc. Am.* **62**, 727 (1972).
- [89] Hilger Ltd., F. Twyman, and A. Green, “Improvements in finishing prisms or lenses or combinations of the same and in apparatus therefor,” patent GB103832 (5 February 1917).
- [90] D. Malacara, ed., *Optical shop testing* (Wiley, New York, 1978).
- [91] J. Schwider, R. Burow, K. E. Elssner, J. Grzanna, R. Spolaczyk, and K. Merkel, “Digital wave-front measuring interferometry: some systematic error sources,” *Appl. Opt.* **22**, 3421–3432 (1983).
- [92] Y. Y. Cheng and J. C. Wyant, “Multiple-wavelength phase-shifting interferometry,” *Appl. Opt.* **24**, 804–807 (1985).
- [93] D. A. Thomas and J. C. Wyant, “Determination of dihedral angle errors of a corner cube from its Twyman-Green interferogram,” *J. Opt. Soc. Am.* **67**, 467–472 (1977).

- [94] C. Y. Ai and K. L. Smith, “Accurate measurement of the dihedral angle of a corner cube,” *Appl. Opt.* **31**, 519–527 (1992).
- [95] M. S. Scholl, “Ray trace through a corner-cube retroreflector with complex reflection coefficients,” *J. Opt. Soc. Am. A* **12**, 1589–1592 (1995).
- [96] J. Burke, K. L. Green, N. Raouf, J. A. Seckold, and B. F. Oreb, “Certification of the full size double corner cube fiducials for the Space Interferometer Mission – PlanetQuest test bed,” *Proc. SPIE* **7013**, 701351 (2008).
- [97] T. W. Stuhlinger, “Subaperture optical testing: experimental verification,” *Proc. SPIE* **655**, 350 (1986).
- [98] J. B. Houston, “Using Ritchey-Common test for large plane mirrors (flats),” *Opt. Eng.* **14**, 88–90 (1975).
- [99] T. S. Turner, “Subaperture testing of a large flat mirror,” *P. Soc. Photo.-Opt. Ins.* **1752**, 90–94 (1992).
- [100] Z. Linchao, X. Bin, and X. Jingjiang, “Combination of Skip-Flat test with Ritchey-Common test for the large rectangular flat,” *Proc. SPIE* **7656**, 76564W (2010).
- [101] J. A. Bosh, ed., *Coordinate measuring machines and systems* (Marcel Dekker, New York, 1995).
- [102] D. Schütze, V. Müller, and G. Heinzl, “Precision absolute measurement and alignment of laser beam direction and position,” *Appl. Opt.* **53**, 6503–6507 (2014).
- [103] F. Sorrentino, K. Bongs, P. Bouyer, L. Cacciapuoti, M. de Angelis, H. Dittus, W. Ertmer, A. Giorgini, J. Hartwig, M. Hauth, S. Herrmann, M. Inguscio, E. Kajari, T. T. Könnemann, C. Lämmerzahl, A. Landragin, G. Modugno, F. Pereira dos Santos, A. Peters, M. Prevedelli, E. M. Rasel, W. P. Schleich, M. Schmidt, A. Senger, K. Sengstock, G. Stern, G. M. Tino, and R. Walser, “A compact atom interferometer for future space missions,” *Microgravity Sci. Tec.* **22**, 551–561 (2010).
- [104] F. Sorrentino, K. Bongs, P. Bouyer, L. Cacciapuoti, M. de Angelis, H. Dittus, W. Ertmer, J. Hartwig, M. Hauth, S. Herrmann, K. Huang, M. Inguscio, E. Kajari, T. Könnemann, C. Lämmerzahl, A. Landragin, G. Modugno, F. Pereira dos Santos, A. Peters, M. Prevedelli, E. M. Rasel, W. P. Schleich, M. Schmidt, A. Senger, K. Sengstock, G. Stern, G. M. Tino, T. Valenzuela, R. Walser, and P. Windpassinger, “The Space Atom Interferometer project: status and prospects,” *J. Phys. Conf. Ser.* **327**, 012050 (2011).
- [105] D. N. Aguilera, H. Ahlers, B. Battelier, A. Bawamia, A. Bertoldi, R. Bondarescu, K. Bongs, P. Bouyer, C. Braxmaier, L. Cacciapuoti, C. Chaloner, M. Chwalla, W. Ertmer, M. Franz, N. Gaaloul, M. Gehler, D. Gerardi, L. Gesa, N. Gürlebeck, J. Hartwig, M. Hauth, O. Hellmig, W. Herr, S. Herrmann, A. Heske, A. Hinton, P. Ireland, P. Jetzer, U. Johann, M. Krutzik, A. Kubelka,

- C. Lämmerzahl, A. Landragin, I. Lloro, D. Massonnet, I. Mateos, A. Milke, M. Nofrarias, M. Oswald, A. Peters, K. Posso-Trujillo, E. Rasel, E. Rocco, A. Roura, J. Rudolph, W. Schleich, C. Schubert, T. Schuldt, S. Seidel, K. Sengstock, C. F. Sopena, F. Sorrentino, D. Summers, G. M. Tino, C. Trenkel, N. Uzunoglu, W. von Klitzing, R. Walser, T. Wendrich, A. Wenzlawski, P. Weels, A. Wicht, E. Wille, M. Williams, P. Windpassinger, and N. Zahzam, “STE-QUEST – test of the universality of free fall using cold atom interferometry,” *Class. Quantum Grav.* **31**, 115010 (2014).
- [106] M. Sommerfeld, “Development of a calibrated quadrant photodiode pair (CQP),” Master’s thesis, Max Planck Institute for Gravitational Physics (Albert Einstein Institute) and Institute for Gravitational Physics, Leibniz Universität Hannover, 30167 Hanover, Germany (2010).
- [107] G. H. Golub and C. Reinsch, “Singular value decomposition and least squares solutions,” *Numer. Math.* **14**, 403–420 (1970).
- [108] D. Schütze, G. Stede, V. Müller, O. Gerberding, T. Bandikova, B. S. Sheard, G. Heinzl, and K. Danzmann, “Laser beam steering for GRACE Follow-On intersatellite interferometry,” *Opt. Express* **22**, 24117–24132 (2014).
- [109] D. Schütze and D. Farrant, “Triple mirror assembly prototype static beam coalignment,” Test report, LRI-AEI-TR-001, Max Planck Institute for Gravitational Physics (Albert Einstein Institute) and Institute for Gravitational Physics, Leibniz Universität Hannover, 30167 Hanover, Germany (2012).
- [110] D. Schütze, B. S. Sheard, and M. Dehne, “Triple mirror assembly DM point of minimal coupling test procedure,” Test plan, LRI-AEI-TP-001, Max Planck Institute for Gravitational Physics (Albert Einstein Institute) and Institute for Gravitational Physics, Leibniz Universität Hannover, 30167 Hanover, Germany (2013).
- [111] D. Schütze and M. Dehne, “TMA QM point of minimal coupling test procedure,” Test plan, LRI-STI-TP-005, SpaceTech GmbH Immenstaad, 88090 Immenstaad, Germany (2014).
- [112] D. Schütze, V. Müller, and G. Stede, “Point of minimal coupling and vertex of ANU Glass Tma,” Test report LRI-AEI-TR-002, Max Planck Institute for Gravitational Physics (Albert Einstein Institute) and Institute for Gravitational Physics, Leibniz Universität Hannover, 30167 Hanover, Germany (2013).
- [113] D. Schütze, “Triple mirror assembly DM point of minimal coupling test procedure (filled-in),” Test report, LRI-AEI-TR-003, Max Planck Institute for Gravitational Physics (Albert Einstein Institute) and Institute for Gravitational Physics, Leibniz Universität Hannover, 30167 Hanover, Germany (2014).
- [114] D. Schütze, “TMA QM point of minimal coupling test campaign – brief summary,” Test report, LRI-AEI-TR-004, Max Planck Institute for Gravitational Physics (Albert Einstein Institute) and Institute for Gravitational Physics, Leibniz Universität Hannover, 30167 Hanover, Germany (2014).

- [115] D. Schütze, “DWS-steering-mirror loop tests with DLR QPD EBB,” Technical note, LRI-AEI-TN-009, Max Planck Institute for Gravitational Physics (Albert Einstein Institute) and Institute for Gravitational Physics, Leibniz Universität Hannover, 30167 Hanover, Germany (2014).
- [116] T. Bandikova, J. Flury, and U.-D. Ko, “Characteristics and accuracies of the GRACE inter-satellite pointing,” *Adv. Space Res.* **50**, 123–135 (2012).
- [117] A. Görth, “Development of a fiber-based intersatellite laser link simulator for GRACE Follow-On,” Master’s thesis, Max Planck Institute for Gravitational Physics (Albert Einstein Institute) and Institute for Gravitational Physics, Leibniz Universität Hannover, 30167 Hanover, Germany (2013).
- [118] G. Wanner, G. Heinzel, E. Kochkina, C. Mahrtdt, B. S. Sheard, S. Schuster, and K. Danzmann, “Methods for simulating the readout of lengths and angles in laser interferometers with Gaussian beams,” *Opt. Commun.* **285**, 4831–4839 (2012).
- [119] E. Kochkina, G. Heinzel, G. Wanner, V. Mueller, C. Mahrtdt, B. Sheard, S. Schuster, and K. Danzmann, “Simulating and optimizing laser interferometers,” *ASP Conf. Ser.* **467**, 291–292 (2013).
- [120] IfoCAD – interferometer simulation tool, Max Planck Institute for Gravitational Physics (Albert Einstein Institute) and Institute for Gravitational Physics, Leibniz Universität Hannover, 30167 Hanover, <http://www.lisa.aei-hannover.de/ifocad>.
- [121] M. Dehne, “Construction and noise behaviour of ultra-stable optical systems for space interferometers,” [PhD thesis](#), Max Planck Institute for Gravitational Physics (Albert Einstein Institute) and Institute for Gravitational Physics, Leibniz Universität Hannover, 30167 Hanover, Germany (2012).
- [122] F. Steier, R. Fleddermann, J. Bogenstahl, C. Diekmann, G. Heinzel, and K. Danzmann, “Construction of the LISA back-side fibre link interferometer prototype,” *Class. Quantum Grav.* **26**, 175016 (2009).
- [123] C. J. Killow, E. D. Fitzsimons, J. Hough, M. Perreur-Lloyd, D. I. Robertson, S. Rowan, and H. Ward, “Construction of rugged, ultrastable optical assemblies with optical component alignment at the few microradian level,” *Appl. Opt.* **52**, 177–181 (2013).

Acknowledgments

I would like to express my thankfulness to everyone who has supported and accompanied me during the past years.

During my time at the Albert Einstein Institute, I have experienced an uninterrupted series of professional delights. I am very thankful for being a part of thrilling experiments, heated discussions, and brilliant ideas. Such creative productiveness and inspiration can only dwell on nourishing grounds. I am very thankful to my supervisor and thesis referee Karsten Danzmann for providing this unique scientific environment and for welcoming me into his group.

I was fortunate to enter the GRACE Follow-On LRI team at a very exciting period of transition from sheer concept studies and prototype experiments to testing of engineering models and the beginning of flight unit production. It was very motivating to be part of this growth process.

I am very thankful to Gerhard Heinzel for his kind and supporting supervision. His expertise and understanding of physics have been an enrichment. Furthermore, I am especially thankful to Benjamin Sheard for keeping his office door open at all times. His profound knowledge, sharp thinking, and inerrant advice have helped me a lot to develop my own ideas and to keep my research on the right track.

I am very grateful for the past years spent in the Space Interferometry group at the Albert Einstein Institute, which is full of brilliant minds and kind hearts. I especially enjoyed working with Vitali Müller, whose ideas and insights often brought the crucial inspiration to my mind. Furthermore, I am very thankful to Simon Barke for improving my design skills and to Natalia Korsakova and Gunnar Stede for being the most awesome office buddies in the world.

I would like to thank Daniel Shaddock, who kindly invited me to stay with his group at the Australian National University for three months. These months have been very productive as well as enjoyable. The time spent with the Graviteers both inside and outside the lab was unforgettable. To name a few, Roland Fleddermann and his lovely wife Kerstin, Danielle Wuchenich, and Andrew Sutton – thank you for making my stay pleasant and exciting.

During my stay in Australia, I also had the opportunity to work with David Farrant at CSIRO in Sydney. I witnessed the final assembly steps of the first Triple Mirror Assembly prototype which was a thrilling experience.

The LRI team is a unique group of diverse parties, all of which contribute invaluablely to the project as a whole. What unites us is the common vision of the LRI. My PhD project of developing test environments for the LRI would not have been possible without the support of all project partners. They have kindly provided me with detailed information on the LRI units that I wanted to test and, most importantly, with the units themselves. For this great cooperation, I would like to thank the whole LRI team, including our colleagues from JPL, STI, DLR Bremen, and DLR Berlin.

The LRI meetings have always been highlights in the project. With all the different members of the LRI team sitting around one table, the air was filled with electricity. Eager to make the LRI work, everyone was driven to his or her own best. I am especially thankful to William Klipstein, who was a constant source of motivation and inspiration during these meetings.

Most of the meetings I have attended were held at STI in Immenstaad and I would like to thank our colleagues from STI for being such kind hosts. Furthermore, we had the great opportunity to visit our colleagues at JPL in Pasadena to take part in a test campaign. It was such an inspiration to be at the birthplace of aerospace. I am very thankful to the whole team at JPL for making our time there so enjoyable.

I am very grateful to the people who kindly proof-read this thesis and helped me with their excellent comments and remarks. In alphabetical order, I would like to thank Heather Audley, Tamara Bandikova, Simon Barke, Christina Bogan, Germán Fernández, Alice Flint, Oliver Gerberding, Alexander Görth, Gerhard Heinzl, Christoph Mahrtdt, Vitali Müller, and Philip Peterson. Of course, I take full responsibility for all remaining mistakes.

I would like to thank Karsten Danzmann, Claus Braxmaier, and Jakob Flury for being referees to this thesis. Furthermore, I would like to thank Clemens Hammerer for being the chair of my thesis defense committee.

I gratefully acknowledge the funding agencies which have supported the research of this thesis: the Bundesministerium für Bildung und Forschung (BMBF, project number: 03F0654B), the Deutsche Forschungsgemeinschaft (DFG) within the Cluster of Excellence QUEST (Centre for Quantum Engineering and Space-Time Research), and the Australian Government's Australian Space Research Program (ASRP).

I am very thankful for the support and love which my parents and family have poured on me over all these years. You have given me the strength to become the person who I am today.

Finally, I would like to thank a very special person in my life, who, after all, is the sun behind the veil: my dear wife Sayoko. Thank you for giving me your heart.

Curriculum vitae



Daniel Schütze
Hainhölzer Str. 28
30159 Hanover, Germany
danielschuetze13@gmail.com
Born on November 13, 1981 in Neuss, Germany.

- | | |
|------------|------------------------------------------------------------------------------------------------------------------------------------------------------------------------------------------------------------------------------------------|
| 2014/12/16 | PhD defense examination |
| 2012/07–09 | Research visit to the Australian National University (Canberra, Australia) |
| 2011–2014 | PhD student, research assistant, and IMPRS stipend holder at the Max Planck Institute for Gravitational Physics (Albert Einstein Institute) and the Institute for Gravitational Physics, Leibniz Universität Hannover (Hanover, Germany) |
| 2010 | Research assistant and BCGS stipend holder at the Rheinische Friedrich-Wilhelms-Universität Bonn (Bonn, Germany) |
| 2009/06–09 | Research visit at the National Institute for Materials Science, JSPS stipend holder (Tsukuba, Japan) |
| 2002–2009 | Physics diploma studies at the Rheinische Friedrich-Wilhelms-Universität Bonn (Bonn, Germany) |
| 1992–2001 | Abitur, secondary school education at the Gymnasium Norf (Neuss, Germany) |
| 1988–1992 | Primary school education at the St.-Andreas-Grundschule Norf (Neuss, Germany) |

Publications

Peer-reviewed journal articles

D. Schütze, G. Stede, V. Müller, O. Gerberding, T. Bandikova, B. S. Sheard, G. Heinzl, and K. Danzmann, “Laser beam steering for GRACE Follow-On intersatellite interferometry,” *Opt. Express* **22**, 24117–24132 (2014).

D. Schütze, V. Müller, and G. Heinzl, “Precision absolute measurement and alignment of laser beam direction and position,” *Appl. Opt.* **53**, 6503–6507 (2014).

D. Schütze, V. Müller, G. Stede, B. S. Sheard, G. Heinzl, K. Danzmann, A. J. Sutton, and D. A. Shaddock, “Retroreflector for GRACE Follow-On: Vertex vs. point of minimal coupling,” *Opt. Express* **22**, 9324–9333 (2014).

D. Schütze, D. Farrant, D. A. Shaddock, B. S. Sheard, G. Heinzl, and K. Danzmann, “Measuring coalignment of retroreflectors with large lateral incoming-outgoing beam offset,” *Rev. Sci. Instrum.* **85**, 035103 (2014).

R. L. Ward, R. Fleddermann, S. Francis, C. Mow-Lowry, D. Wuchenich, M. Elliot, F. Gilles, M. Herding, K. Nicklaus, J. Brown, J. Burke, S. Dligatch, D. Farrant, K. Green, J. Seckold, M. Blundell, R. Brister, C. Smith, K. Danzmann, G. Heinzl, D. Schütze, B. S. Sheard, W. Klipstein, D. E. McClelland, and D. A. Shaddock, “The design and construction of a prototype lateral-transfer retro-reflector for inter-satellite laser ranging,” *Class. Quantum Grav.* **31**, 095015 (2014).

Y. Wang, D. Keitel, S. Babak, A. Petiteau, M. Otto, S. Barke, F. Kawazoe, A. Khalaidovski, V. Müller, D. Schütze, H. Wittel, K. Danzmann, and B. F. Schutz, “Octahedron configuration for a displacement noise-cancelling gravitational wave detector in space,” *Phys. Rev. D* **88**, 104021 (2013).

B. Knabe, D. Schütze, T. Jungk, M. Svete, W. Assenmacher, W. Mader, and K. Buse, “Synthesis and characterization of Fe-doped LiNbO₃ nanocrystals from a triple-alkoxide method,” *Phys. Status Solidi A* **208**, 857–862 (2011).

K. Kitamura, H. Hatano, S. Takekawa, D. Schütze, and M. Aono, “Large pyroelectric effect in Fe-doped lithium niobate induced by a high-power short-pulse laser,” *Appl. Phys. Lett.* **97**, 082903 (2010).

D. Schütze, B. Knabe, M. Ackermann, and K. Buse, “Orientation of colloiddally suspended LiNbO₃ nanocrystals in externally applied electric fields,” *Appl. Phys. Lett.* **97**, 242908 (2010).

Peer-reviewed conference proceedings

K. Abich, C. Bogan, C. Braxmaier, K. Danzmann, M. Dehne, M. Gohlke, A. Görth, G. Heinzel, M. Herding, C. Mahrtdt, V. Müller, K. Nicklaus, J. Sanjuan, D. Schütze, B. Sheard, G. Stede, K. Voss, “GRACE Follow-On laser ranging instrument: German contribution,” *J. Phys. Conf. Ser.* (accepted for publication).

B. Knabe, M. Peter, D. Schütze, M. Ackermann, and K. Buse, “Nonlinear optics with lithium niobate nanocrystals” in *2011 Conference on Lasers & Electro-Optics Europe (CLEO EUROPE/EQEC) and 12th European Quantum Electronics Conference* (Institute of Electrical and Electronics Engineers, New York, 2011).

Non-peer-reviewed articles

K. Nicklaus, M. Herding, A. Baatzsch, M. Dehne, C. Diekmann, K. Voss, F. Gilles, B. Guenther, B. Zender, S. Boehme, V. Mueller, D. Schütze, G. Stede, B. Sheard, and G. Heinzel, “Optical bench of the Laser Ranging Interferometer on GRACE Follow-On,” to be published in *Proceedings of International Conference on Space Optics (ICSO)*.

K. Danzmann *et al.*, “The gravitational universe,” European Space Agency (ESA) L2/L3 Science Theme Selection, [arXiv:1305.5720](https://arxiv.org/abs/1305.5720) (2013).

G. Heinzel, B. S. Sheard, N. Brause, K. Danzmann, M. Dehne, O. Gerberding, C. Mahrtdt, V. Müller, D. Schütze, G. Stede, W. Klipstein, W. Folkner, R. Spero, K. Nicklaus, P. Gath, and D. A. Shaddock, “Laser ranging interferometer for GRACE Follow-On,” in *Proceedings of International Conference on Space Optics (ICSO, 2012)*.

D. Schütze, G. Stede, V. Müller, O. Gerberding, C. Mahrtdt, B. S. Sheard, G. Heinzel, and K. Danzmann, “LISA-like laser ranging for GRACE Follow-On,” *ASP Conf. Ser.* **467**, 285–289 (2013).

GRACE Follow-On project internal documents

D. Schütze, “DWS-steering-mirror-loop tests with DLR QPD EBB,” Technical note, LRI-AEI-TN-009, Max Planck Institute for Gravitational Physics (Albert Einstein Institute) and Institute for Gravitational Physics, Leibniz Universität Hannover, 30167 Hanover, Germany (2014).

D. Schütze, “TMA QM point of minimal coupling test campaign – brief summary,” Test report, LRI-AEI-TR-004, Max Planck Institute for Gravitational Physics (Albert Einstein Institute) and Institute for Gravitational Physics, Leibniz Universität Hannover, 30167 Hanover, Germany (2014).

D. Schütze and M. Dehne, “TMA QM point of minimal coupling test procedure,” Test plan, LRI-STI-TP-005, SpaceTech GmbH Immenstaad, 88090 Immenstaad, Germany (2014).

PUBLICATIONS

D. Schütze, “Triple mirror assembly DM point of minimal coupling test procedure (filled-in),” Test report, LRI-AEI-TR-003, Max Planck Institute for Gravitational Physics (Albert Einstein Institute) and Institute for Gravitational Physics, Leibniz Universität Hannover, 30167 Hanover, Germany (2013).

D. Schütze, B. S. Sheard, and M. Dehne, “Triple mirror assembly DM point of minimal coupling test procedure,” Test plan, LRI-AEI-TP-001, Max Planck Institute for Gravitational Physics (Albert Einstein Institute) and Institute for Gravitational Physics, Leibniz Universität Hannover, 30167 Hanover, Germany (2013).

D. Schütze, G. Stede, and V. Müller, “Point of minimal coupling and vertex of ANU Glass TMA,” Test report, LRI-AEI-TR-002, Max Planck Institute for Gravitational Physics (Albert Einstein Institute) and Institute for Gravitational Physics, Leibniz Universität Hannover, 30167 Hanover, Germany (2013).

D. Schütze and D. Farrant, “Triple mirror assembly prototype static beam coalignment,” Test report, LRI-AEI-TR-001, Max Planck Institute for Gravitational Physics (Albert Einstein Institute) and Institute for Gravitational Physics, Leibniz Universität Hannover, 30167 Hanover, Germany (2012).